BRNO UNIVERSITY OF TECHNOLOGY
VYSOKÉ UČENÍ TECHNICKÉ V BRNĚ

FACULTY OF MECHANICAL ENGINEERING
FAKULTA STROJNÍHO INŽENÝRSTVÍ

INSTITUTE OF SOLID MECHANICS, MECHATRONICS AND BIOMECHANICS
ÚSTAV MECHANIKY TĚLES, MECHATRONIKY A BIOMECHANIKY

AUTOMATING THE SEARCH FOR ABNORMALITIES FROM TOMOGRAPHIC DATA
AUTOMATIZACE VYHLEDÁVÁNÍ ABNORMALIT Z TOMOGRAFICKÝCH DAT

MASTER'S THESIS
DIPLOMOVÁ PRÁCE

AUTHOR
AUTOR PRÁCE

Bc. Petr Semerák

SUPERVISOR
VEDOUCÍ PRÁCE

Ing. Jiří Bazala

BRNO 2024

BRNO FACULTY
UNIVERSITY OF MECHANICAL
OF TECHNOLOGY ENGINEERING

Assignment Master's Thesis

Institut:	Institute of Solid Mechanics, Mechatronics and Biomechanics
Student:	**Bc. Petr Semerák**
Degree programm:	Mechatronics
Branch:	no specialisation
Supervisor:	**Ing. Jiří Bazala**
Academic year:	2023/24

As provided for by the Act No. 111/98 Coll. on higher education institutions and the BUT Study and Examination Regulations, the director of the Institute hereby assigns the following topic of Master's Thesis:

Automating the search for abnormalities from tomographic data

Brief Description:

One of the few ways to analyze the quality of the product by non–destructive testing due to the structure of the material and its connection is CT analysis. The CT data of the product must then be carefully checked by an experienced expert who manually marks the abnormalities. It is offered to create a software tool that identifies the locations of possible defects since the abnormalities have a very similar manifestation in location and morphology. This method is expected to reduce the financial costs of inspection, the requirement for radiologist experience and the risk of erroneous analysis.

Master's Thesis goals:

Research on the use of available software for automatic abnormality detection
Categorization of heat exchanger abnormalities
Design and creation of an algorithm enabling the detection and marking of suspicious locations
Software testing including user environment and output verification
Discuss the possibility of involving artificial intelligence tools

Recommended bibliography:

X-Ray CT: Hardware and Software Techniques, Hiroyuki Toda,

VG studio

Deadline for submission Master's Thesis is given by the Schedule of the Academic year 2023/24

In Brno,

L. S.

_____   _____
prof. Ing. Jindřich Petruška, CSc.   doc. Ing. Jiří Hlinka, Ph.D.
Director of the Institute   FME dean

ABSTRACT

The presented thesis concerns the automation of the process of scanning and evaluating abnormalities of gascoolers that occur during their production. Non-destructive testing employs CT scanning technology, which generates image data as an output. The objective of the work is to replace the time-consuming manual data scanning process with a reliable algorithmic method and to assess the potential of this direction of development. The theoretical part of the thesis deals with cooling systems in cars, non-destructive testing with a focus on CT technology and a search for software for viewing and analysing CT data. The practical part of the thesis focuses on the problem of clogged gascooler ducts. The causes of this abnormality, the current approach to its detection and a new automatic inspection approach are described. The proposed algorithm together with an application developed using Matlab are tested on concrete data. Finally, the reliability of the results is evaluated by manual inspection of the CT images. A deep neural network is trained to assess the quality of the image data.

KEYWORDS

Gascooler, X-Ray micro computed tomography, CT, Image processing, Fourier transform

ABSTRAKT

Předložená diplomová práce se zabývá automatizací procesu skenování a vyhodnocování abnormalit gascoolerů, které vznikají při jejich výrobě. Nedestruktivní testování využívá technologii CT skenování jejímž výstupem jsou obrazová data. Cílem práce je nahradit zdlouhavý proces ručního procházení dat spolehlivou algoritmizovatelnou metodou a ověřit, zda je tento směr vývoje perspektivní. V teoretické části se práce zabývá chladícími systémy v automobilech, nedestruktivním testování s těžištěm v CT technologii a rešerší softwarů pro prohlížení a analýzu CT dat. Praktická část diplomové práce se zaměřuje na problematiku ucpaných kanálků gascoolerů. Jsou popsány příčiny vzniku této abnormality, dosavadní přístup k jejímu odhalení a nový automatický přístup kontroly. Navržený algoritmus spolu s aplikací vytvořenou pomocí Matlabu jsou testovány na konkrétních datech. Spolehlivost výsledků je v závěru porovnávána ručním hodnocením CT snímků. Pro hodnocení kvality obrazových dat je trénována hluboká neuronová síť.

KLÍČOVÁ SLOVA

Gascooler, rentgenová počítačová tomografie, CT, zpracování obrazu, Fourierova transformace

BIBLIOGRAPHIC CITATION

SEMERÁK, Petr. *Automating the search for abnormality from tomographic data* [online]. Brno, 2024 [cit. 2024-05-24]. Available from: https://www.vut.cz/studenti/zav-prace/detail/157477. Diploma thesis. Brno University of Technology, Faculty of Mechanical Engineering, Institute of Solid Mechanics, Mechatronics and Biomechanics. Supervisor Jiří Bazala.

AFFIDAVIT

I declare that presented thesis has been composed solely by myself under the supervision of Ing. Jiří Bazala. All references, literature sources and other resources I have utilized to develop this work have been appropriately cited and acknowledged.

In Brno, 24th of May 2024   Bc. Petr Semerák

ACKNOWLEDGEMENT

CONTENTS

INTRODUCTION

Air conditioning units are an integral part of modern automobiles. Their purpose is to ensure the necessary comfort for the driver, thereby reducing fatigue while driving, and indirectly mitigating the risk of traffic accidents in automotive transport. Compressor-based air conditioning circuits typically use various refrigerants to regulate cabin temperature. These refrigerants have a significant negative impact on the environment, especially on the greenhouse effect. A recent trend is to replace these refrigerants with less harmful substances, such as CO2.

Switching to more environmentally friendly refrigerants undoubtedly promises less environmental impact but also creates a broad field of technical challenges that need to be addressed. Traditional condensers used in air conditionings operating at about 3.5 bar are being replaced by gascoolers, which must operate at much higher pressures to ensure the same cooling performance. While condensation of the refrigerant occurs in the condenser, the gascooler only cools the refrigerant without its phase change. This necessitates many technical modifications to this equipment, with the most discussed in this thesis being the reduction of the internal geometry of the channels.

With the increasing demands for output quality in production, it is necessary to seek new and progressive methods for detecting potential manufacturing defects. Thanks to rapid technological advances, the use of 3D CT scanners for non-destructive testing has become very accessible and effective. This technology allows for the creation of a 3D digital twin of the scanned part in a short time, on which it is possible to view each external and internal structure in detail.

The growing demands for testing from customers and production increase the time complexity of evaluating product quality, while maintaining high reliability of the method is necessary. This leads to the need to continuously increase the efficiency of processing a large amount of data produced by CT technology. Incorporating this technology into production processes is a relatively new trend that also provides ample space for further innovation.

This thesis focuses on the algorithmizing and finding an efficient way to evaluate CT data of gascoolers, focusing on characteristic abnormalities that occur during their production. The theoretical part of the thesis is dedicated to a brief description of gascoolers and CT scanning technology. The aim of the theoretical part is then to describe and categorize characteristic abnormalities during their production. It also focuses on an overview of commercial software used for visualizing and analyzing CT data. The final chapter is dedicated to the basics of image processing, which is utilized in the practical part.

The experimental part of the thesis focuses on analyzing the current process of scanning and viewing CT reconstructions of a specific type of gascooler. The goal of the thesis is to algorithmize the process of finding typical abnormalities, further design and implement a semi-automatic defect detection system without the need for manual intervention. For this purpose, custom software with a simple user interface should be designed, which will then be tested on real data. The possibility of involving artificial intelligence will be discussed within the results of the designed and tested algorithm.

1 THEORETICAL PART

The theoretical part of this thesis focuses on the description of the differences between the condenser and the gascooler as a component in the cooling cycle of a car. It also characterises possible manufacturing defects of the gascooler and non-destructive methods by which defects are detected. Most attention is focused on the X-ray method, which is the focus of the thesis. The principle of X-ray generation and detection and the formation of the CT image are described. This is followed by a review of commercial and freely available software for visualising and working with CT data. Finally, the research section is devoted to basic 2D image handling in Matlab, histogram equalisation and image frequency analysis. The method of detecting the principal directions in the image by integrating in the amplitude spectrum of the image, which is obtained using the Fourier transform, is explained. The image processing theory is further used in the practical part of the thesis.

1.1 VEHICLE AIR CONDITIONING HISTORY

Air conditioning is now an integral part of most mass-produced cars on the market. It was first installed in 1940 by the Packard Motor Car Company in the Packard 180. [1], [2], [3] However, it was an oversized unit with low efficiency and no controls and was not in great demand. The first mass-produced car with air conditioning was the Chrysler Imperial, produced in 1953. In the years that followed, air conditioning spread to other luxury and mainstream car models in the US and Europe. Adjusting the temperature of the cabin air is now commonplace in many engineering applications. The technology improves comfort, reduces driver fatigue and overheating, and contributes to improved road safety [2],[4].

1.2 WORKING PRINCIPLE OF AIR CONDITIONING

At its simplest, the function of a cooling circuit can be thought of as the inverse behaviour of a heat engine. In a heat engine, heat is extracted from the hot part and then converted into mechanical work. A refrigeration circuit works in exactly the opposite way, adding mechanical work to the system to transfer heat energy from the cooler part to the warmer part.

The compressor air conditioner operates on the basis of the inverted Clausius-Rankin cycle. The second law of thermodynamics applies, i.e. a substance at a higher temperature always transfers heat energy to a substance at a lower temperature. The refrigerant in the air conditioning circuit is heated by the warm air in the cabin, then compressed by the compressor to increase the temperature potential, and the refrigerant can be cooled by the cooler air outside. The pressure of the refrigerant, which is undergoing metabolic transformation, therefore plays a key role in the correct functioning of the air conditioning system [3].

The air conditioning system of a car consists of two primary sections: the high-pressure branch and the low-pressure branch. In Figure 1.1, the high-pressure branch is depicted in orange and yellow, while the low-pressure branch is shown in blue. The system incorporates a compressor and an expansion valve (or expansion nozzle) to facilitate changes in pressure within the circuit. The refrigerant circulates between the condenser and the evaporator, ensuring continuous cooling. In the high-pressure section, the condenser is responsible for condensing the refrigerant

vapor at high pressure. Conversely, the evaporator is located in the low-pressure section, where it facilitates the evaporation of the refrigerant.
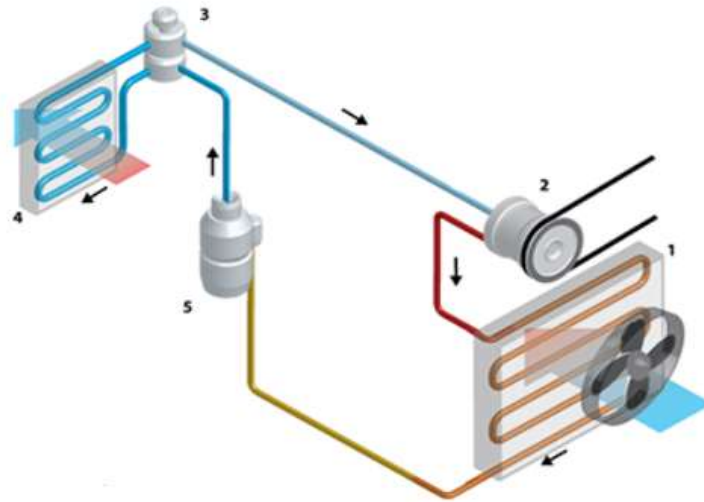
Figure 1.1 Air conditioning system [6].

Initially, the refrigerant enters the compressor as slightly superheated vapor. The compression process increases its pressure and temperature, further superheating the vapor. This elevation in pressure also raises the refrigerant's condensing temperature. The superheated vapor then flows into the condenser, where it releases heat, first cooling to a saturated vapor and then undergoing isobaric condensation into a saturated liquid, ultimately reaching a subcooled liquid state. The liquid refrigerant then passes through the expansion valve, where a rapid isoenthalpic drop in pressure occurs, causing partial evaporation. The partially evaporated refrigerant proceeds to the evaporator, where it fully evaporates by absorbing heat from the surrounding environment. Now in the form of saturated to slightly superheated vapor, the refrigerant returns to the compressor at a lower pressure, ready to begin the cycle anew [5], [6].

1.3 MANIFOLD CONDENSERS

The condenser in an air conditioning system is responsible for condensing the high-pressure gaseous refrigerant received from the compressor. Within the condenser, the refrigerant cools down and transforms into a liquid state, while still maintaining high pressure. To enhance heat transfer efficiency, condensers are fitted with a fan. Figure 1.2 illustrates a condenser from the air-cooling system.
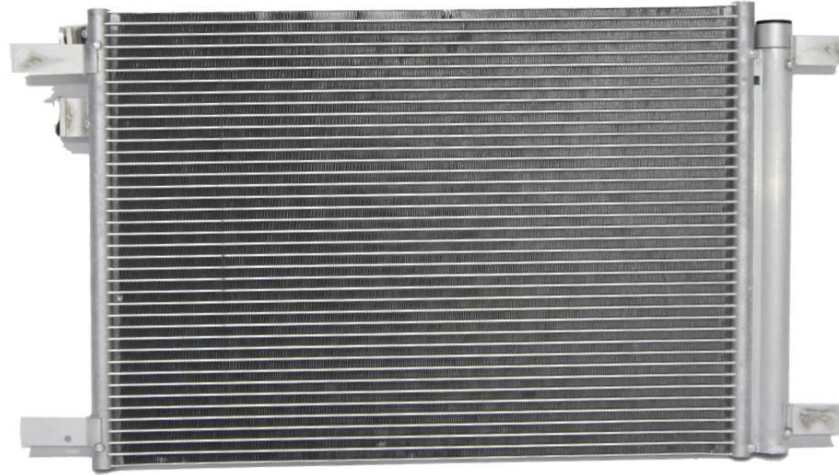
Figure 1.2 Manifold condenser [8].

There are two types of condensers: zigzag condensers, which consist of a single tube twisted several times, and the second type, which has a different design. Ribs or bellows can be inserted between the tubes to increase the effective area [1].

The second type of condenser arrangement is the parallel condenser, which can be compared to a flow radiator. In this arrangement, the medium flows through a large number of fins that are parallel to each other. According to the available literature, this arrangement is up to 25% more efficient. Therefore, it is preferred in various technical solutions and is also the subject of this thesis [7].

The input and output block is attached to the manifold. These are used to connect the condenser to the hoses of the air conditioning circuit. There are two holes on the face of the connection blocks. One is threaded for attachment and the other serves as a connection coupling for the refrigerant hose. Great emphasis is placed on precision when manufacturing the second hole and the patented MSF (Metal Seal Fitting) connection is used here. This unconventional metal to metal connection ensures zero refrigerant leakage from the system. The refrigerant flow is shown in the Figure 1.3.
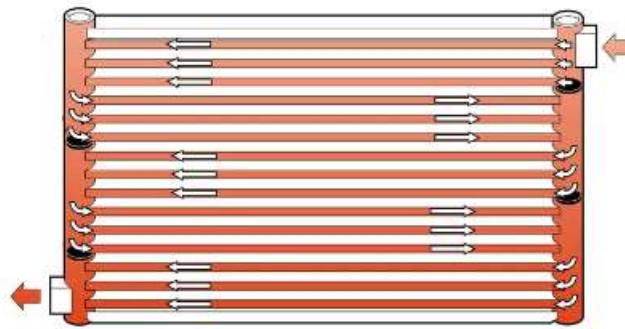
Figure 1.3 Schematic of the manifold capacitor.

The Manifold distributes the refrigerant to individual tubes, each containing several channels (ports). A bent sheet metal (bellows) is inserted between the tubes to increase the surface area for heat transfer. The manifolds are located on either side of the condenser and contain baffles that direct the flow of refrigerant so that it passes through the condenser in an axis.

The material of the condenser is in most cases aluminium because it is suitable for the manufacturing process. These are often aluminium extrusion (tubes), drawing (connection blocks) or pressing (manifolds).

1.3.1 REFRIGERANT

A refrigerant is a chemical substance or combination of substances that circulates in a hermetically sealed refrigeration system. In this closed circuit, the refrigerant undergoes a phase change from gas to liquid and vice versa. The main function of the refrigerant is to transfer heat energy.

There are many chemicals and mixtures that can be used as refrigerants, but not all of them have suitable properties for trouble-free use in technical applications. A key factor in the quality of refrigeration equipment is the correct choice of refrigerant.

There are many factors to consider when selecting a suitable refrigerant. These are thermomechanical properties (suitable boiling point), physical properties (flammability, explosiveness, ...), chemical properties (corrosiveness, erosive effects, chemical stability), physiological effects on humans (toxicity, etching), ecological requirements (ozone depleting substances, prohibited media) and, last but not least, the availability and price of the refrigerant [9], [10], [11].

1.3.2 REFRIGERANTS IN THE AUTOMOTIVE INDUSTRY

Historically, two primary refrigerants used in refrigeration systems were ammonia and CO2. Both have notable drawbacks: ammonia is toxic to humans, while CO2 requires extremely high pressures, typically between 30 kPa and 200 kPa, within the refrigeration circuit. In supercritical operation, the compressor outlet temperature can reach 160°C, leading to additional technical issues, such as problems with the lubricant [11].

The advent of Freon 12 (dichlorodifluoromethane) addressed these issues by providing a highly stable and non-toxic alternative that is also inert to compressor lubricants. Freon 12 operates at a pressure slightly above atmospheric pressure (approximately 3.5 kPa), allowing refrigerant to be added to the system without the need for a vacuum. Moreover, the slight overpressure within the refrigeration circuit naturally prevents ambient air from entering the system [11].

Freon 12 could be considered an ideal refrigerant for refrigeration circuits, but when it leaks into the atmosphere and reaches the Earth's ozone layer, it is broken down by UV radiation, releasing very aggressive chlorine radicals that break down ozone molecules. This was the main reason why Freon 12 was banned. It has been replaced by a chlorine-free refrigerant called R-134a (tetrafluoroethane). Although this replacement is not as stable as the original Freon 12, it does not contain chlorine radicals and does not cause ozone depletion, which is why it was used for a long time by all car air conditioning manufacturers [11].

Global warming is a well-known problem that is largely caused by man-made substances. For this reason, the Global Warming Potential (GWP) unit has been introduced and individual substances are assigned GWP values relative to CO2 (GWP = 1). On this scale, R-134a has a GWP of 1300 and has been banned across Europe for all car manufacturers since 2017. At the same time, the European Parliament and the Fluorinated Greenhouse Gases Council are discussing appropriate legislation to facilitate a total ban on fluorinated gases (F-gases), which would ban F-gases with a GWP greater than 150 in Europe from 2027 [11], [12].

The refrigerant R-134a has been replaced by R-1234yf, developed by DuPont and Honeywell. The refrigerant meets strict European regulations and achieves GWP = 4. This is a very significant change from an environmental point of view. R-1234yf can be used at pressures similar to those of R-134a, while using 5% less refrigerant. These features make R-1234yf a suitable replacement for existing air conditioning systems without the need to develop additional components [11].

A major disadvantage of the new R-1234yf refrigerant is that it is classified as A2L under PN EN 378, i.e. highly flammable. This means that R-1234yf is difficult to ignite [13].

However, the refrigerant passed the required tests and, despite some debate about the suitability of the substance in the car and the risk of fire in the event of an accident, the refrigerant was approved and used in the air conditioning systems of most modern cars. However, it has come under scrutiny, particularly from German car manufacturers, who are working hard to find a more suitable replacement [11].

A return to CO2 refrigerant (R-744) could be a reasonable solution. Although a very high pressure is required for CO2 to work, this is also to some extent an advantage. At this pressure, the refrigerant has a very high viscosity and it is therefore possible to reduce the overall refrigeration circuit while maintaining the same cooling capacity. The high outlet temperature at the compressor is suitable for instant windscreen defrosting. And the price of CO2 is significantly lower than the price of R-1234yf refrigerant [11].

1.4 GASCOOLER

A gascooler is a heat exchanger in an air conditioning system used to cool a compressed gaseous medium with ambient air without mixing the two substances. In the case of an air-cooled gascooler, cooling of the refrigerant gas to a temperature 3 K higher than the ambient air temperature can be achieved. In air conditioning systems using R-744 (CO2) as the refrigerant, the condenser is replaced by a gascooler. These systems operate at very high intermediate pressures and are therefore much more susceptible to refrigerant leaks, which are undesirable and, in the case of automotive air conditioning, even dangerous for the crew. This places greater demands on the mechanical connections and components of the entire circuit [14], [15].

The main difference between a gascooler and an air conditioning condenser is the duty cycle. Whereas a condenser in traditional refrigeration cycles condenses the refrigerant from a gaseous to a liquid state, a gascooler only cools the medium, which is always in a gaseous state and does not condense. This cycle often uses R-744 refrigerant, which is more environmentally friendly.

Due to the different cooling mechanism (no condensation of the medium) and different operating pressures of the refrigerant, gascoolers differ in their geometry from classical condensers working e.g. with R-134a. The high pressure in the system causes a high refrigerant viscosity, which leads to a difference in the dimensions of the channels inside the gascooler tubes. These are much smaller. While the condensers have a channel size of approximately 0.2 – 3 mm, the channels in the gascoolers are in the range of 0.01 - 0.2 mm [6].

1.4.1 GASCOOLER PRODUCTION

In practice, such thin channels are achieved by extrusion. The whole tube is always produced with a defined number of channels in one very long piece. The number of channels varies for different types of gascoolers. The individual tubes are cut from the long strip and inserted into the frame together with the manifolds and other parts of the gascooler. A "cladding" is applied to the surface of all parts and the entire component is heated to a suitable temperature. At this temperature, the surface of the aluminium components is melted, assisted by the cladding (decomposition of Al2O3 on the surface), and a strong, inseparable bond is made at the interface between the components. This process is very critical for the production of gascoolers.

This is also how the individual duct pipes are connected to the manifolds. Due to the melting of the surfaces during the connection of the components, the gascooler material rises into the ducts. Such blockages reduce the efficiency of the gascooler and increase the pressure drop of the refrigerant during operation of the refrigeration circuit. It is therefore necessary to control the production of gascoolers and the number of blocked channels. It is advantageous to use non-destructive methods to analyse internal defects in the component.

1.4.2 PRODUCT QUALITY CONTROL

Within the manufacturing process of gacoolers, a meticulous quality control procedure is implemented, involving comprehensive technical inspections and tests, including both visual evaluation of the products and the application of pressure tests to verify the leak tightness and mechanical integrity of the entire system. It is of paramount importance to test the mechanical design of the refrigerant inlet and outlet used to connect the component to the air conditioning

circuit. The precision of these parts is of critical importance, as they must provide a fully mechanical, disassembled connection that also ensures perfect leak tightness and zero refrigerant leakage even at very high pressures in the lower hundreds of kPa. Furthermore, thermographic diagnostics and ultrasonic inspection are employed to detect subtle internal defects such as microcracks and porosity. In addition to these methods, advanced analytical techniques such as CT analysis are employed to identify material inhomogeneities and structural abnormalities, thereby ensuring that each gascooler meets the established quality and safety standards.

1.4.3 CATEGORIES OF ABNORMALITIES IN THE MANUFACTURE OF GASCOOLERS

Abnormalities in the production of gascoolers can be divided into several basic categories. The first type that can be discussed is structural defects. These can arise from improper soldering that causes some joints to be weak. At these points, refrigerant leaks can occur later. This defect is very critical and extremely undesirable. It is therefore necessary to consistently test all pieces at a so-called leakage station just for possible leaks at all joints.

Furthermore, the soldering process may also result in deformation of the gascooler. This is often caused by inaccurate positioning of the components in the mounting frame. It can also be caused by uneven heating of the piece.

A particularly serious structural fault, which this work is concerned with detecting, is the blockage of the channels. Before soldering, a chemical powder, also known as flax, is applied to the product. The purpose of this powder is to facilitate thermal disruption of the alumina, which is found on the surface of the gascooler and effectively passivates it. However, the passivation layer prevents the necessary melting of the surfaces and their quality bonding. Improper amounts of this chemical, coupled with an improper temperature profile for heating the piece, causes solder to penetrate into the manifold channel orifice. The molten material then rises capillarily into the channels where it solidifies after cooling to ambient temperature, resulting in partial or complete permanent blockage of the channel. This impairs coolant flow through the gascooler, creates undesirable pressure drops and impairs heat transfer. This leads to a reduction in the cooling performance of the entire air conditioning system.

The second type of defect that can be described here is that of contamination of the internal parts of the gasooler. Common sources of contamination include mechanical dirt and dust, which can block narrow ducts or cause abrasive damage to the air conditioning system. In addition to mechanical contaminants from the manufacturing process, the gascooler may be contaminated with various lubricants used during production. Lubricants typically form an undesirable film on the inner surfaces of the channels, which impairs the heat transfer between the medium and the gascooler, thus negatively affecting the cooling performance of the equipment. Furthermore, there is a risk of chemical reaction of the injected lubricant with the refrigerant, which could lead to degradation of the refrigerant properties.

Finally, a potential issue during the final production stage is the ingress of water into the gascooler system. Once the air conditioning system is activated, water can evaporate and increase the pressure within the system. This can result in excessive stress on the mechanical connections, with the potential for refrigerant leakage into the surrounding area. It is therefore of the utmost importance to exercise caution when working with any chemicals that could enter

the gascooler during the manufacturing process and potentially react with the gascooler material or refrigerant.

The final category of manufacturing defects is that of faulty design of the gascooler geometry. These can result in poor refrigerant flow inside the channels, inadequate pressure inside the gascooler, and ultimately, inefficient heat transfer.

It is of the utmost importance that the aforementioned inlet and outlet blocks of the gascooler are correctly designed and precisely executed. These blocks ensure the connection of the gascooler to the air conditioning system and are subject to very strict mechanical tolerances. The joints ensure a mechanical, reusable and perfectly tight connection, thereby eliminating the risk of refrigerant leakage.

1.5 Non-destructive testing methods

Due to the complex structure of the gascooler, demanding production requirements, potential risks of defects, and high standards for quality, reliability, and durability of the manufactured units, it is crucial to carefully monitor the quality of serial production. Non-destructive testing methods are a suitable tool to verify the production process and provide proof of product quality for the customer.

Non-destructive methods of testing a component are those methods which use a reasonable amount of energy to detect a defect, but which do not damage the component and after which the component can continue to operate. These methods can be used to search for surface, internal or latent defects in the component and to evaluate material defects. The oldest non-destructive method is visual inspection. More advanced methods are based on various physical principles such as reflection of sound waves, methods using magnetic fields, X-rays, etc. Some methods are only suitable for detecting surface defects. In the context of the gascoolers under investigation, more emphasis will be placed on methods capable of detecting internal component defects [16].

1.5.1 Ultrasonic testing

Ultrasonic defectoscopy is a widely used method for examining the internal structure of materials and detecting cracks. It involves the propagation of sound waves with a frequency above 20 kHz through the material at a speed of sound characteristic of that material. Ultrasonic testing detects defects and imperfections in components by reflecting ultrasonic waves or attenuating the signal. The method's resolution depends on the frequency of the sound waves, with higher frequencies allowing for the detection of smaller defects. The method aims to identify internal imperfections in the material being tested, such as bubbles, pores, cracks, and surface defects. It is particularly effective in detecting defects that are perpendicular to the direction of the transmitted ultrasonic waves. This includes defects in welds or in metal products that have been forged or rolled, as well as castings. This method is appropriate for testing a variety of materials, such as steel, other metals, plastic, rubber, and concrete. It is especially useful for larger components and those that are already built-in, where only one surface is accessible. However, due to the gascooler's geometry and the presence of various edges in the component, this method is not suitable for evaluating clogged channels [16], [17].

1.5.2 Eddy current testing (ECT)

The eddy current method applies an alternating voltage to the component under test via an alternating magnetic field generated by a coil. Eddy currents are generated in the component, which produces its own magnetic field. The method detects defects by measuring changes in the conductivity of the material and the density of the eddy currents. A difference in phase and voltage at the excitation or external measuring coil indicates the change. This method is effective only for testing electrically conductive materials. The principle of fault detection is that the currents pass through the sample in circular paths with the least resistance. If a discontinuity in the material is encountered, the current is forced to bypass the defect, allowing it to be detected. Testing the sample from different directions greatly facilitates defect detection, particularly when the defect is perpendicular to the direction of flow [17].

1.5.3 INFRARED (IR) THERMOGRAPHY

The infrared thermography method monitors the temperature field distribution on the surface of a heated component over time. It analyses the values of the temperature field and its gradients to identify potential defects based on inhomogeneities in the temperature field distribution. Defects affect heat propagation differently than the surrounding homogeneous material [17].

These methods are effective for detecting defects in various materials, but may not be suitable for detecting small defects in complex components such as gascoolers. In such cases, Computed Tomography (CT) is preferred for evaluating the gascooler channels after the soldering process. CT provides reliable and accurate visualization of the internal structure of materials or components and can digitize the finished part. However, this method can be time-consuming and expensive [17].

1.5.4 MICRO CT

This is a relatively new and progressive technology of non-destructive testing that is widely used in biomedicine, material sciences, geology, and many other fields. This technology provides volumetric information about the structure of the sample and is suitable for detecting defects on the surface and inside the objects under investigation. The testing process involves placing the object between an X-ray source and a sensitive detector. Once the detector has detected the X-rays, an image of a single section of the part is created and the part is rotated by a small angle. This process is repeated until the object has reached a 180° (or occasionally 360°) rotation. A 3D model is then reconstructed from the individual 2D projections. Due to the permeability of X-rays, the internal structure can be examined in sections on the resulting 3D model [18].

This technology provides imaging information with very high resolution, which other non-destructive methods are unable to match. From the resulting models, it is possible to plot, for example, porosity, material density, and cavity dimensions. The method is fully applicable to the investigation of the internal structure of materials without the need for mechanical cuts, for example in the study of teeth, bone, tissue or also batteries and many others [18].

1.6 X-RAY

X-rays have a wavelength range of 0.01 to 10 nm and an energy spectrum of 100 eV to 100 keV. They can be classified as 'soft X-rays' (wavelengths above 0.1 nm) and 'hard X-rays' (wavelengths below 0.1 nm) based on their ability to penetrate matter.

1.6.1 X-RAY SOURCE

The most effective method for generating X-rays is through the use of an X-ray tube, as shown in Figure 1.4. This tube consists of a cathode and an anode (target) within a vacuum. The cathode, made from a heated tungsten or molybdenum filament, emits electrons which are then accelerated by an electric field between 30 kV and 450 kV. The speed and intensity of the emitted X-rays depend on this acceleration energy [23].
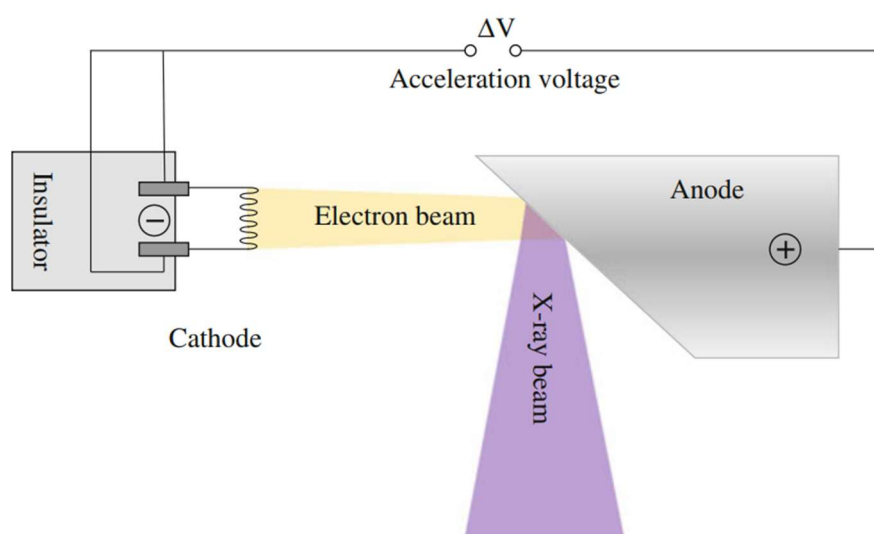

Figure 1.4 X-Ray tube diagram [22].

Electrons are aimed at a focal spot on the anode and then directed towards the object. Since 99% of the energy converts to heat upon impact with the anode, the anode must be made from heat-resistant materials like tungsten or molybdenum, with efficient cooling systems in place to manage the heat [22], [27].

Only 1% of the electron energy turns into X-rays. After striking the anode, electrons either slow down near the nuclei, producing bremsstrahlung radiation, or knock out inner-shell electrons, causing the atom to become ionized. When electrons from higher energy levels fill these vacancies, characteristic radiation is emitted. Therefore, the X-ray output consists of both bremsstrahlung and characteristic radiation [22].

The X-ray spectrum is an important characteristic that determines how effectively the radiation penetrates various materials. This spectrum is influenced by several factors, including the cathode current, which controls the number of electrons generated and thus the intensity of the X-rays. The accelerating voltage also plays a crucial role by increasing the energy of the electrons, which affects their interaction with the anode. The material of the anode is another significant factor, as it directly impacts the resulting spectrum and the characteristic radiation emitted. To refine the X-ray spectrum, thin metal filters such as copper, aluminium, or molybdenum are used. These filters remove low-energy radiation, reducing artifacts in the final image and enhancing the overall image quality [22].

1.6.2 INTERACTION OF X-RAY WITH THE OBJECT

As X-rays pass through an object, their intensity decreases exponentially due to four basic interactions with matter [25].

PHOTOELECTRIC EFFECT

The photoelectric effect occurs when an X-ray photon collides with an electron in an atom of the irradiated material. If the photon's energy exceeds the electron's binding energy, the electron is ejected from its shell. The kinetic energy of this ejected electron, which determines its speed, is the difference between the photon's energy and the electron's binding energy. During this process, the incoming photon is fully absorbed [22], [25].

Once the electron is knocked out, the atom remains ionized and in an excited state. An electron from a higher shell then fills the vacancy, resulting in the emission of characteristic radiation. This emitted radiation, known as a fluorescence photon, has a discrete energy equal to the difference in potential between the higher and lower electron shells [25].

COMPTON (INCOHERENT) SCATTERING

Compton scattering occurs when an X-ray photon collides with an electron in a target atom. For this phenomenon to happen, the incoming photon must possess energy much higher than the electron's binding energy. During the interaction, the photon ejects the electron from the atom. Unlike the photoelectric effect, the photon is not absorbed but instead continues traveling at a different angle and with a reduced frequency.

This change in frequency indicates that the photon has lost energy due to the collision. The ejected electron, known as the Compton electron, takes away some of the photon's energy. The deflection angle of the Compton electron decreases as the energy of the incident photon increases [22].

RAYLEIGH/THOMPSON (COHERENT) SCATTERING

Rayleigh (Thomson) scattering occurs when a low-energy photon interacts with an electron in an atom of the irradiated object. This phenomenon is based on the interaction of electromagnetic waves through their electric fields, resulting in the elastic scattering of electrons, whether they are bound to the atom or free.

The primary distinction between Rayleigh scattering and other processes such as Compton scattering, or the photoelectric effect is that Rayleigh scattering does not cause ionization or significant energy transfer. The photon is merely deflected, or scattered, without any loss of energy. This process is crucial in applications where the preservation of the photon's energy is essential, such as optical imaging and atmospheric physics. Additionally, Rayleigh scattering is responsible for the blue appearance of the sky, as shorter wavelengths (blue light) are scattered more effectively than longer wavelengths (red light) by atmospheric molecules [22].

PAIR PRODUCTION

In this phenomenon, an electron-positron pair is created within the Coulomb field of an electron or nucleus. The newly formed pair subsequently annihilates each other, resulting in the emission of two gamma rays. These gamma rays typically travel in opposite directions and can either be scattered or absorbed by the surrounding material.

It is important to note that in common industrial applications using X-ray energies below 1 MeV, the contribution of pair production to the total absorption is usually negligible. This process becomes significant only at higher photon energies, typically above 1,02 MeV, which is the energy threshold for pair production to occur. In such high-energy environments, pair production can play a more substantial role, especially in fields like nuclear physics and high-energy astrophysics [26].

The total absorption of radiation μ is given by the sum of the previous effects and can be written by the following relation [22]:

$$\mu = \mu_{PE} + \mu_{CS} + \mu_{RS} + \mu_{PP}, \tag{1.1}$$

where μ_{PE} is the absorption coefficient due to photoelectric effect, μ_{CS} is the absorption coefficient due to Compton scattering, μ_{RS} is the absorption coefficient due to Rayleigh scattering, μ_{PP} is the absorption coefficient due to pair production. In common practical CT applications, the electron energy ranges from 10 keV to 150 keV. At these energies, the photoelectric effect and Compton (incoherent) scattering are the main contributors to the total X-ray absorption. The contribution of each mechanism to the absorption of radiation as a function of energy is shown in Figure 1.5 [22].
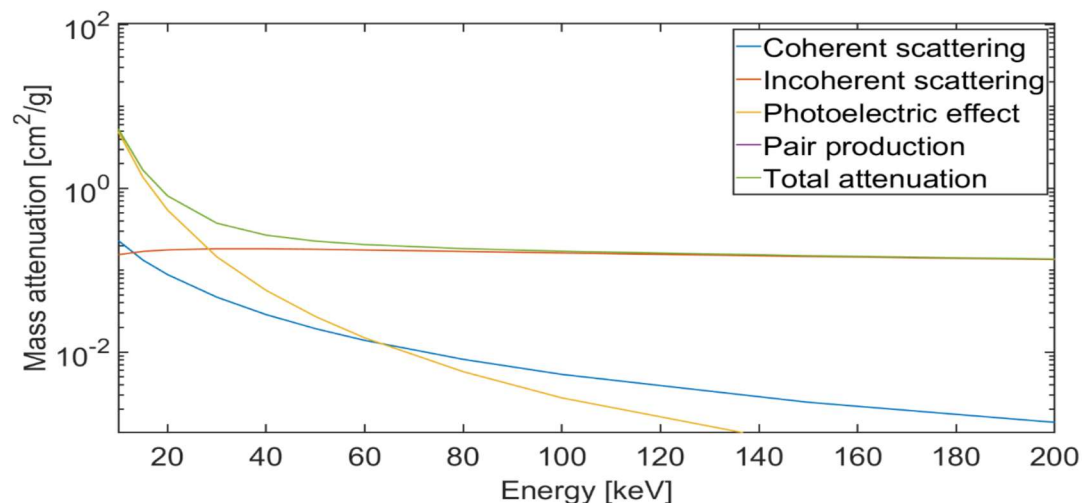

Figure 1.5 Contribution of different physical mechanism to the bulk water attenuation function. Data taken from the XCOM database [27].

1.6.3 X-RAY DETECTION

X-ray detection works by converting scattered X-rays into an electrical signal, which is then digitized and binarized. This process generates a 2D or 3D reconstruction of the scattered radiation distribution, allowing for visualization on a computer [22], [25], [26], [27].

There are two primary methods for detecting scattered X-rays: direct and indirect detection. In direct detection, the scattered radiation ionizes a gas such as xenon, directly producing an electrical signal. In contrast, indirect detection involves transforming the scattered X-rays into another form of radiation, typically light, which is then converted into an electrical signal. This method is illustrated in Figure 1.6. [22], [25], [26], [27].

CT manufacturers have long focused on increasing the number of detection elements simultaneously exposed to X-rays. This advancement facilitates faster data acquisition and enhances the thermal efficiency of X-ray tubes. Direct-conversion detectors and solid-state detectors (scintillators) are generally more scalable to multi-line or multi-layer arrays, making them highly suitable for advanced imaging systems. Conversely, indirect-conversion detectors using high-pressure gas tubes face scalability challenges when applied to planar detection systems [22].

Recent advancements in materials and electronics have significantly improved the sensitivity and resolution of both detection methods. The development of advanced semiconductor materials for direct detection and more efficient scintillators for indirect detection has led to higher image quality and reduced radiation doses. These innovations are essential in medical diagnostics and industrial applications, where precision and safety are of utmost importance [22], [23].
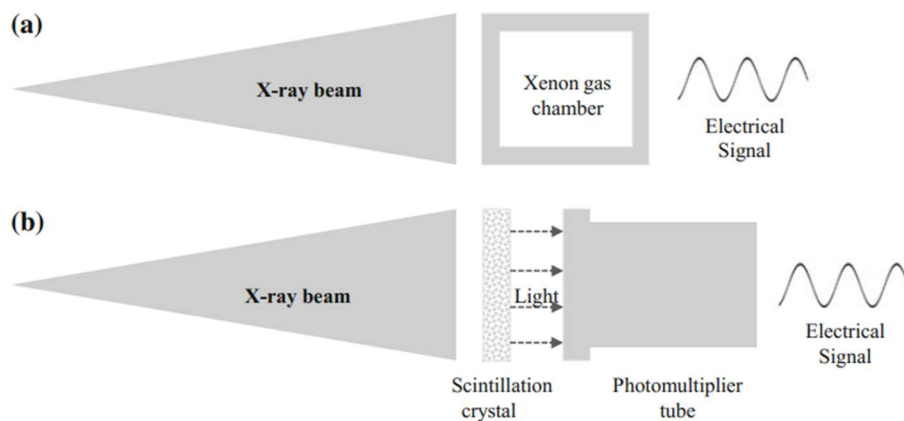

Figure 1.6 Schematic of scattered X-ray detection (a) gas tube detector (b) solid state detector [22].

1.6.4 X-RAY DETECTORS

Almost all modern computed tomography (CT) scanners use solid-state detectors. They consist of a luminescent crystal (scintillator) and a photon detector (sensor). The operating principle of solid-state detectors is the conversion of X-rays passing through the scintillator into visible light and its subsequent detection. The emitted light is directed to the sensor, which produces an output signal in the form of a digital number (DN). This represents the sum of photons or energy absorbed in a pixel during a single exposure [21], [22].

The main parameters of the scintillator are the quantum efficiency required to convert X-rays into visible light, where the range of emitted wavelengths should match the optimum range of detector efficiency. Equally important are the absorption of the scintillator and the time constant of the radiation detection process. These properties directly affect the quality of the reconstruction of the scattered X-rays [21], [22].

Typically, scintillators are made from materials such as sodium iodide with thallium addition, cesium iodide, $CdWO_4$, ZnS, Gd_2O_2S, naphthalene, anthracene and other rare earth based compounds. The scintillators are then coupled to photon detectors via a lens system or fibre optic channel. Depending on the output signal, solid-state X-ray detectors can be further classified into integrating and counting detector [21], [22].

1.6.5 INTEGRATING DETECTORS

An ideal integrating detector produces a signal that is directly proportional to the total energy of the incoming X-rays, i.e. the sum of all the X-rays quanta. The electrical signal from the photodiode is integrated over a period of time (integration period). At the end of the integration period, the resulting charge is read out and the next integration period begins. The total time, including the integration period and the charge period, is called the reading. The integrated signal is then amplified, digitised and further processed by an analogue-to-digital converter, where the output signal corresponds to the total detected energy of all incoming X-ray photons during a reading [21], [22].

CHARGE-COUPLED DEVICE (CCD)

A CCD is an integrated circuit consisting of an array of coupled capacitors that together form a photosensitive region. Each capacitor can transfer its electrical charge to an adjacent capacitor. During the detection process, the absorbed photons form electron-hole pairs when they strike the chip, and the electrons are collected in electron tails that correspond to individual pixels. After the integration time, the pixels are digitally read by an ADC in a readout register located on one side of the chip. As the electrons are read, they pass into the pixels of the adjacent column until all columns reach the readout register. Here they are amplified and digitised by the AD converter. Unfortunately, this process is quite slow and takes about a second to read an image [27].

FLAT PANEL DETECTORS (FPD)

The FPD chip is composed of a matrix of pixels, where each pixel contains a photodiode and a thin silicon transistor on a single glass substrate. The pixel matrix is then coated with a scintillator layer made of caesium iodide (CsI). The chip is covered by a thin aluminium housing, and a carbon cover to protect the chip from mechanical damage [27].

COMPLEMENTARY METAL-OXIDE SEMICONDUCTOR (CMOS)

CMOS chips are similar to CCD chips. In contrast to CCDs, each individual pixel of the content has electronics to amplify and convert the charge of a particular pixel. Each pixel contains a type of AD converter, so it is possible to amplify the signal on each pixel without the need for charge transfer. This chip achieves very high reading speeds because the pixels are read independently at the same time, and also has low power consumption. The drawback is lower sensitivity [27], [28].

1.6.6 COUNTING DETECTORS

Standard detectors cannot distinguish between different energies of X-ray photons, causing artefacts called "beam hardening". This limits the ability to inspect multi-component materials. This has led to the development of the photon counting detector (PCD) technique, currently used in some CT applications, which overcomes the limitations of conventional detectors. PCDs are based on the direct conversion of X-ray photons into an electrical charge. This technology is based on high-energy physics experiments carried out at CERN in the 1980s [27].

A PCD chip consists of a layer of sensors made up of semiconductor crystals that convert incident X-ray photons into an electrical signal. The absorption efficiency of the sensor depends on the photon energy, the material used and the thickness. The PCD allows differentiation between different photon energy levels, which is widely used in scanning multi-component samples. Compared to conventional detectors such as CCDs or FPDs, PCDs eliminate interfering components, increasing detection capability, contrast and SNR (signal to noise ratio). Research into PCD technology has focused on several laboratories and manufacturers, resulting in several readout electronics designs and overall PCD configurations [27].

1.6.7 PROPERTIES OF DETECTORS

X-ray detectors can be assessed on the basis of their mechanical and electronic properties. Important properties are geometrical characteristics and quantum efficiency.

GEOMETRICAL CHARACTERISTICS

Due to the presence of electronic sensor circuitry adjacent to each pixel, a small but significant portion of the pixel is insensitive to incoming radiation. This is known as the 'dead' area. The distortion can be caused by, among other things, uneven magnification. If part of an image falls outside the detector, that image will be misinterpreted, and the overall 3D representation of the component will be cartoonish [28].

QUANTUM EFFICIENCY

The quantum efficiency of a detector is the property that determines whether an incident X-ray photon produces a usable signal when it hits the detector. It is related to the energy of the incident photon and the sensitivity of the pixel. The energy of the photon increases with the number of collisions it has with the atoms of the object being scanned. The probability of a collision then increases as the wall thickness of the scanned object increases. This means that objects with a thin wall may not always be detected correctly. Signal generation at the detector is also affected by the thickness of the active pixel layer. The thicker the active pixel layer, the more sensitive the pixel is to incident radiation. In an ideal detector, all pixels would be equally sensitive, but this is not the case in real detectors [28].

The probability μ that photon generates a usable signal after hitting detector is given [29]:

$$\mu = 1 - \exp\left(-\mu(E)T\right), \tag{1.2}$$

where T is thickness of detector, $\mu(E)$ is linear attenuation of detector and E is the energy of the photon [29].

NOISE

The resulting quality of the scan is affected by noise, which occurs randomly in the image and has a Gaussian distribution and mean value that can be predicted by statistical methods [30].

ACQUISITION SPEED

The scanning speed is mainly influenced by the volume of the body being scanned, the data processing speed and the desired image resolution [28].

DYNAMIC RANGE

Another very important feature of the detector is its dynamic range. The detector does not have a linear response over the entire radiation spectrum, but only over a certain frequency interval. If the incident photon is too low in energy, it may not be detected at all. On the other hand, if the energy of the photon is too high, the pixel on the detector can go into saturation, where if two photons of different energies hit the detector, both of which are high, the pixel cannot distinguish between the different energy levels and the signal produced by the pixel is the same for both photons [28].

Other key features that affect the quality of the resulting 3D display are spatial resolution, uniformity, and frame rate. Of course, finally, the price also influences whether a particular detector is applied and used in practice and decides whether a given technology is a successful XCT system [28].

1.7 X-Ray Computed Tomography (XCT)

CT technology uses X-rays to examine internal structures of parts. X-rays pass through the part and are detected on the opposite side by a detection system. Introduced in 1971, CT scanners have significantly evolved. Key components include the X-ray source, sample stage, and detection system [20], [21], [27].

The standard CT process involves measuring X-ray intensity at different angles as they pass through the sample, capturing 2D projection images. Two main configurations exist: rotating the X-ray source and detector around a stationary sample (common in medical CT) or rotating the sample between a fixed source and detector using rotation stages [19], [20], [27].

Once projections are obtained, tomographic reconstruction creates a 3D image of the sample. This 3D data is essential for detailed analysis and visualization, providing a comprehensive view of the part's internal structure [21], [27].

X-rays are a type of electromagnetic radiation. The frequency of the photons is directly proportional to the energy of the X-rays and can be expressed as [22]:

$$E = hf = \frac{hc}{\lambda},$$

(1.3)

where h is Planck's constant ($6.626 \cdot 10^{-24} \, Js$), c is the speed of light ($299{,}8 \cdot 10^6 \, ms^{-1}$) and λ is the wavelength of radiation [22].

1.7.1 Advantages of XCT

CT scanners are gaining ground in industry in the field of metrology and product quality investigation. The main advantages of this technology include:

- non-destructive testing (NDT) capability for inspection and metrology.
- accurate measurement of complex internal components.
- almost no fixture requirements - parts are scanned in a free-standing state, minimising the risk of damage or clamping affecting the test result.
- Ability to reverse engineer closed geometries and components.

1.7.2 Classification of industrial CT systems

According to the shape of the X-ray beam, industrial CT devices on the market can be divided into two groups. These are linear beam scanners and cone beam scanners [23].

LINE BEAM SCANNERS

This is the first generation of X-ray scanner. The scanning process involves linear movement of the X-ray source and detector and rotational movement of the scanned component around a fixed axis of rotation. This causes several 2D images to be taken, from which a 3D representation of the object is subsequently reconstructed. The system is shown in Figure 1.7 [23].
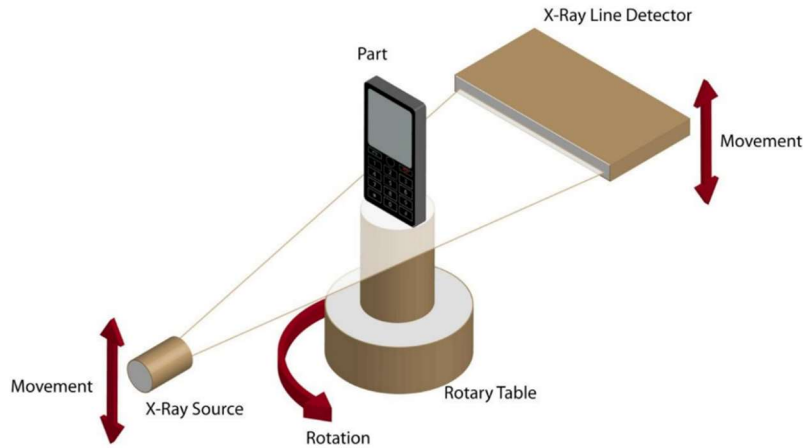
Figure 1.7 Line beam scanner [23].

CONE BEAM SCANNER

This CT scanner system uses a conical X-ray beam that passes through the object and is usually captured on a flat panel detector as shown in Figure 1.8. The object rotates around a fixed axis during the scan. Typically, a large number of 2D images of the component are produced during the scanning process, from which a 3D image of the object is then reconstructed. The reconstruction algorithm is often the Feldkamp algorithm (FDK) [23], [24].

Figure 1.8 Cone beam scanner [23].

1.8 Data reconstruction

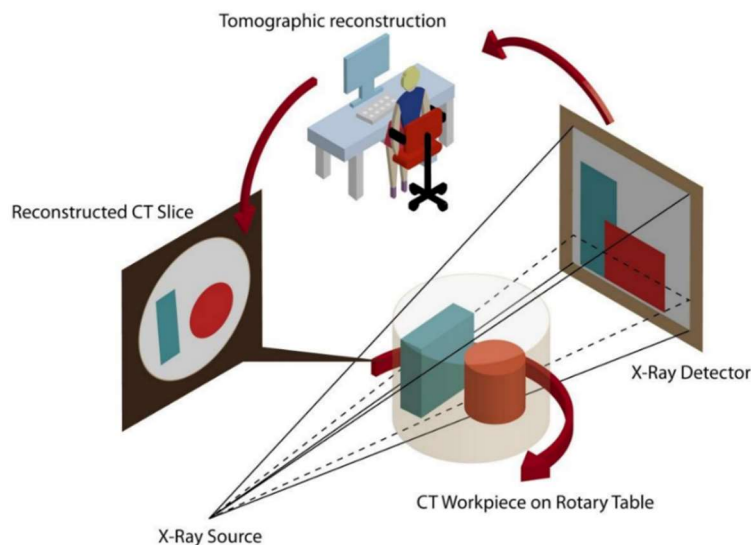Transforming images from the detector into voxels is a process that requires significant computational power and robust computing capabilities. The critical hardware for this task consists of the central processing unit (CPU), random access memory (RAM) and graphics card.

In the field of XCT technology, the role of computing is crucial. Without the reconstruction process, XCT images are essentially equivalent to X-ray images produced by standard radiological methods [28].

The resulting radiographic image is essentially a projection of the object being examined. The brightness of each pixel in this image is determined by the ability of the material to block X-rays (attenuation coefficient) and how far the X-rays travel inside the object. The Radon transform can be used to calculate this projection. Mathematical operation which sums the values along a ray passing through the object $f(x)$ over a certain length L, to produce the projection is given by [31]:

$$pf(L) = \int_L f(x)|dx|, \tag{1.4}$$

XCT reconstruction aims to determine $f(x)$ from the known projection $pf(L)$. This is achieved through a method referred to as backprojection, which is effectively resolved by applying the inverse Radon transform [28].

When researching how to reconstruct images from cone-beam scans, scientists evaluate different methods or algorithms based on their precision and noise tolerance. Two types of algorithms are commonly used: exact and non-exact. Exact algorithms are ideal for noise-free and detailed scan data, requiring sufficient sensors in the right locations. Non-exact algorithms, on the other hand, are more flexible. X-ray algorithms can still function even if some scan data is missing or not detailed enough in certain areas, making them useful when scans are imperfect [31], [32].

Additionally, the path or trajectory of the X-ray source during the scan is an important consideration as it affects the algorithm's ability to reconstruct the image from the scan data [31].

When selecting a method to reconstruct images from cone-beam scans, it is crucial to consider the method's ability to handle imperfect data and the movement of the X-ray during the scan. These factors will determine the most suitable method for obtaining clear images from the scans [31].

1.8.1 Commercial visualisation software

Several software tools are available for CT data reconstruction. In some cases, the software is bundled directly with the CT scanner and often includes advanced data processing, filtering and display functions in addition to basic volumetric data display functions.

VGSTUDIO MAX

VGSTUDIO MAX is a software tool developed by Volume Graphics (VG), a company founded in 1997 in Heidelberg, Germany. VG specializes in processing industrial CT data and has become a leading player in the global industrial CT software market, as confirmed by the 2018 award. Since 2020, VG has been a part of Hexagon, a global leader in sensors, software, and autonomous solutions [31], [33].

Their software specializes in analysing and visualising industrial CT data. They offer products with extensive tools for inspection, measurement, failure analysis, materials analysis and simulation. One of their key products is VGSTUDIO MAX, which enables the reconstruction of 3D visualisations (known as digital twins) from 2D projections. They also offer VGinLINE, a technical solution for fully automated inspection of CT data directly in production. The product is highly configurable due to its single modules. The company's other products include VGMETROLOGY measrement software and myVGL software for displaying finished analysis [31], [33].

Additionally, VG products are compatible with various types of CT scanners from multiple manufacturers. VGSTUDIO MAX can process CT data of products made of plastics, composites, metals, and combinations of these materials. The software is updated four times a year and is compatible with Windows. The software provides options to access macros that automate tasks and save time. It allows for the creation of a fully or semi-automatic workflow. However, its high price is a disadvantage [31], [33].

Avizo

Avizo is a sophisticated software program designed for the visualization and analysis of volumetric data. It was developed from the previous Amira software and is currently being commercially developed and distributed by Thermo Fisher Scientific [31].

The Avizo software provides a comprehensive suite of tools for importing and processing image data from a range of imaging methods and scales, including X-ray tomography (CT, micro/nanoCT), electron microscopy and synchrotron. It facilitates the manipulation of multiple data and images, including time series and very large datasets, and enables the scaling, calibration, conversion and sampling of data. Furthermore, it incorporates advanced options for enhancing image quality and reducing artefacts [34].

The segmentation of image data is made simple with the use of thresholding, automatic segmentation and object recognition tools, as well as machine learning-based algorithms. The software enables the reconstruction of 3D surfaces, the generation of finite element meshes and the application of computational fluid dynamics (CFD), and supports the image-to-simulation workflow, including direct simulations based on 3D images [34].

The Avizo software facilitates the export of analytical and visualisation results for presentation and publication. This includes the creation of animations and videos, the blending of images, geometric models, measurements and simulations, and the export of data to spreadsheets or as 3D models [34].

The software offers high-quality interactive displays, various cutting methods and isopleth extraction for the visualisation and exploration of image data. It also enables image data analysis with quantitative information and supports custom extensions using C++ modules, a Matlab bridge and a Python scripting API, thus facilitating the adaptation of the software to specific user needs [34].

SIMPLEWARE

Simpleware is a sophisticated software from Synopsys that provides comprehensive 3D image data processing tools. These tools enable the transformation of scans into detailed 3D models suitable for a range of applications, including computer-aided design (CAD), computer-aided engineering (CAE) and 3D printing. The software is ideal for a wide range of industrial applications, including biomedical research, materials science and industrial engineering [35].

The software suite, Simpleware, offers a range of advanced features for automatic and manual segmentation, quantitative analysis and the generation of finite element networks from image data. Its ability to integrate with a variety of CAD and CAE software tools enables an efficient workflow from image data to simulation and manufacturing processes. Furthermore, its modular structure supports the extension of features through AI and machine learning, thereby increasing data processing efficiency [35].

DRAGONFLY

Dragonfly by Comet Tech is a comprehensive software platform designed for advanced 3D visualization and analysis, primarily catering to scientific and industrial applications and is providing tools for quality inspection, material science, geoscience, life sciences, and more. It offers a broad range of functionalities including data processing from various imaging modalities such as X-ray, SEM, FIB-SEM, and confocal microscopy. Dragonfly is particularly noted for its capabilities in handling complex imaging data, allowing for both quantitative and qualitative analysis [36].

Dragonfly offers a comprehensive set of features (like Dragonfly 3D World) tailored for advanced 3D visualization, image processing tasks, segmentation and other analysis using Deep Learning. Beside this there are many additional modules and extensions which enhance the functionality of Dragonfly, making it adaptable to specific user needs and expanding its scope [36].

Software is praised for its user-friendly interface and the capability to streamline complex processes, from straightforward visualization to AI-based segmentation and quantification. Comet Tech also offers training programs, tutorials, and maintenance plans to ensure users Dragonfly software can fully leverage its capabilities. There is also a community support system and various resources available to assist users in maximizing their use of the software [36].

1.8.2 FREEWARE VISUALISATION SOFTWARE

In addition to paid software products, many freeware packages can be found on the Internet. Their source code is freely available to end users.

IMAGEJ

ImageJ is a versatile image processing software written in Java that operates on multiple operating systems. It handles 8-bit, 16-bit, and 32-bit images in various formats, including TIFF, GIF, JPEG, BMP, DICOM, FITS, and "raw". The software provides a comprehensive suite of analytical tools, such as area and pixel value analysis, distance and angle measurements, histogram creation, and basic image editing features like sharpening, smoothing, edge detection, and median filtering. Moreover, ImageJ supports fundamental image manipulation tasks, including resizing, geometric transformations, rotation, scaling, and more. Its open architecture facilitates the extension of its capabilities through Java plugins. Developed with Mac OS X tools, the source code of ImageJ is freely accessible [37].

3D SLICER

3D Slicer is a powerful, open-source software for visualising, analysing and manipulating medical data. It was created with contributions from an international community of scientists from many disciplines, including engineering and biomedicine, for research purposes. It supports the visualisation of various types of imaging data in MRI, CT, PET formats in 2D, 3D and 4D. It enables structure segmentation, image registration, surface detection and data analysis, including quantitative analysis and statistics. All functions are available and extensible in Python and C++. A complete Python environment is available, into which any Python packages can be installed and combined with built-in functions. There are no restrictions on the use of the software; however, it should be noted that the software has not been approved for clinical use, which is the responsibility of the user. Furthermore, the software allows the user to utilise HPC (High Performance Computing) to perform computations on remote computing devices. The source code of the software is open and allows for arbitrary modifications, and is available on Linux, macOS and Windows operating systems [38], [39].

OSIRIX

OsiriX is a sophisticated software tool for medical image processing, enabling the visualization and analysis of DICOM data from a variety of medical imaging modalities, including CT, MRI and PET. Two versions are available: the OsiriX Lite version, which is available free of charge to all users for non-commercial use, and the full version. The full version can work with 2D and 3D image data, allows registration, manual image segmentation, and more. Furthermore, it enables the user to perform basic operations on image data, such as modifying contrast, adjusting rotation size, and conducting rudimentary data analysis, including distance and volume measurement [40].

In addition to the aforementioned software tool, OsiriX offers OsiriX MD, which is not free and is designed for professional use in medical applications. Tanto software tool allows, in

addition to all functionalities available in OsiriX Lite, the handling of 4D image data, automatic segmentation of image data, and the ability to work with PACS (Picture Archiving and Communication System) for archiving and sharing medical images. The software provides support for DICOM-RT, a DICOM extension for radiotherapy, and incorporates a number of advanced features. It is employed in a variety of medical fields, including radiology, surgery and oncology [40].

PARAVIEW

ParaView is a sophisticated tool for analysing and visualising scientific datasets, particularly suited to the processing of large and complex 3D data obtained from transmission and scanning electron microscopes. The software is open-source distributed under a BSD licence, allowing users to modify and distribute it freely. The software enables scientists to investigate the structure and perform comprehensive analysis of 3D datasets through a suite of advanced tools, including those for analysis, data segmentation, histogram generation, data correlation, and more. Additionally, users can supplement these tools with custom scripts written in Python [41].

The software permits the combination of multiple datasets, the creation of colour maps, the cropping, rotation and other manipulation of 3D data, and the export of images and videos. Various filters and other advanced tools are also available. The software supports remote HPC resources, allowing the user to perform complex analyses on remote computing servers and supercomputers. The software is supported on Linux, macOS and Windows operating systems [41].

ParaView provides users with a comprehensive array of features and data manipulation options. Its user-friendly interface facilitates the exploration of data, the performance of advanced analysis, and the generation of high-quality visualisations. With its support for numerous data formats and active community support, ParaView plays a pivotal role in scientific research and industrial applications worldwide [41].

1.9 IMAGE PROCESSING IN MATLAB

Matlab is a programming environment that is widely used in research and academic activities. Its flexibility and extensive selection of libraries with specific functions allow a wide range of tasks to be solved efficiently, including those related to optimization, signal processing, statistical computing and image processing. For the purpose of the practical part of this thesis, the Image Processing Toolbox, which is a library providing tools for advanced image data processing, will be used as a key tool. The Image Processing Toolbox library enables the manipulation, filtering, analysis and modification of images.

1.9.1 IMAGE INTERPRETATION

The interpretation of the image in Matlab is analogous to that of other types of signals. However, the principal distinction is the higher dimensionality of the image data, which necessitates the utilisation of specific methodologies for the analysis and manipulation of such data [42], [48].

In Matlab, images are represented as matrices in several ways. The first type is binary images, which consist of simple black and white pixels with values of 0 and 1; where 0 represents black and 1 represents white. These images are commonly used in applications that require distinguishing objects from their background [42].

Another type of image is grayscale, which contains different values representing different grey levels. In the experimental phase, grayscale eight-bit images are employed, where the value 0 represents black colour and 255 represents white colour [42], [48].

The interpretation of colour images employs a set of matrices, with each matrix corresponding to a single colour channel. In the case of RGB images, three matrices are required, one for each colour, resulting in a three-dimensional matrix. The first two dimensions correspond to the number of pixels in the image, while the third dimension corresponds to the number of colour channels [42], [48].

The final method for interpreting images in Matlab is to utilise indexed images. In this instance, the values within the matrix contain indices that refer to the lookup table. This approach is particularly beneficial in scenarios where memory requirements must be optimised [42], [48].

The process of indexing the pixels in a Matlab image is analogous to that of indexing any other matrix, with the numbering commencing with a value of 1 for both rows and columns, beginning at the top left corner of the matrix [42], [48].

1.9.2 FREQUENCY ANALYSIS

Frequency image analysis represents a pivotal aspect of contemporary image data processing. It employs the Fourier transform (FT) to analyse the image as a two-dimensional signal. The discrete two-dimensional Fourier transform (2D DFT), which represents a generalisation of the one-dimensional Fourier transform, can be applied to images in the spectral plane of spatial frequencies. Each point in the resulting spectrum represents a specific spatial frequency [42], [47].

$$F_{m,n} = \frac{1}{N} \sum_{i=0}^{N-1} \sum_{k=0}^{N-1} f_{i,k}\, e^{-j\frac{2\pi}{N}(mi+nk)}, i,k,m,n = 0,1,\dots,N-1, \tag{1.5}$$

where f corresponds to the pixel value of the image in the original area at position i, k. F expresses the value of the complex spectral coefficient at coordinates m, n. N is the number of signal samples (pixels) for the horizontal and vertical planes, here for a square image.

The backward Fourier transform is given by [43]:

$$f_{i,k} = \frac{1}{N} \sum_{m=0}^{N-1} \sum_{n=0}^{N-1} F_{m,n}\, e^{j\frac{2\pi}{N}(mi+nk)}, i,k,m,n = 0,1,\dots,N-1. \tag{1.6}$$

The amplitude spectra of the model signals are shown in the Figure 1.9.
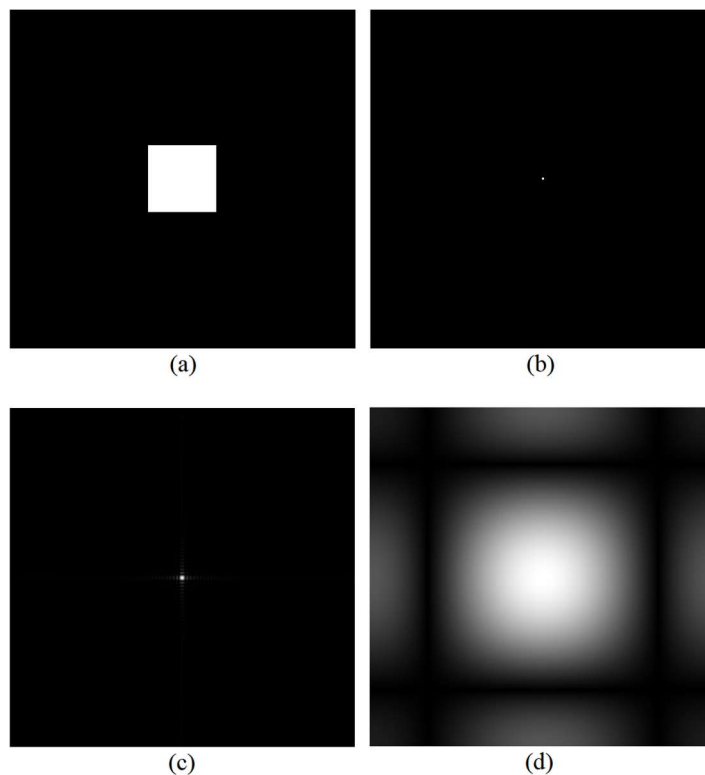

(a) (b)

(c) (d)

Figure 1.9 Model signals and their spectra: (a) model signal in the shape of a square, (b) model signal in the shape of a unit impulse, (c) amplitude spectrum of a square, amplitude spectrum of a unit impulse [42].

The amplitude spectrum of the square signal is equivalent to the two-dimensional sinc function. When the square is reduced in one of the dimensions, the sinc function dilates in the corresponding axis. The limiting case is a unit pulse whose spectrum contains all frequency components equally represented [42].

The spectrum is periodic and consists of sampled 2D basis functions [43]:

$$f(x,y) = A\cos(u_0 x + v_0 y + \varphi), \qquad\qquad (1.7)$$

where A corresponds to the brightness amplitude, φ to the phase, i.e. the displacement of the ridge relative to the origin of the coordinates, and u_0 and v_0 are the angular frequencies, i.e. the number of cycles per unit length in the x and y. The direction of propagation is determined by the ratio of the angular frequencies.
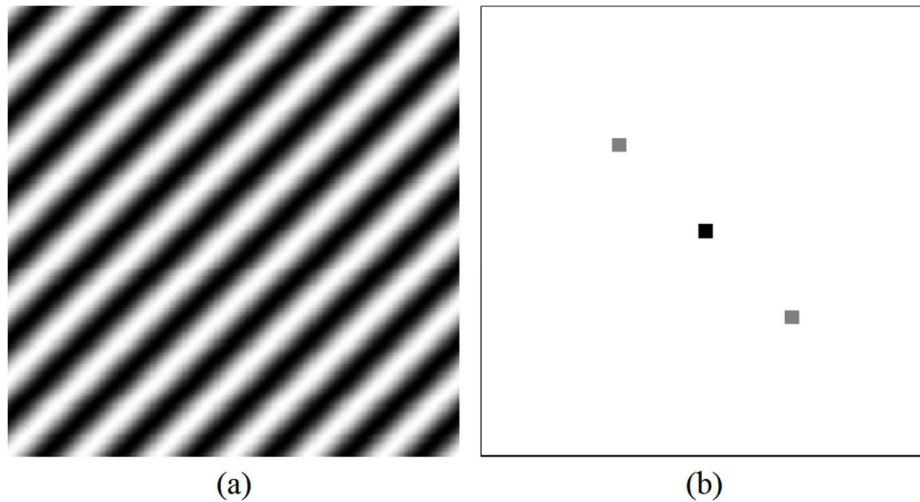

(a)   (b)

Figure 1.10 Harmonic function: (a) original image, (b) amplitude spectrum [47].

Figure 1.10 depicts a two-dimensional harmonic function and its spectrum. The function A is formed by two conjugate points that are symmetric about the origin. The distance from the origin to these points corresponds to the frequency of the image (the frequency of each wave), while the brightness of the points represents the amplitude of that frequency. The direction of the line connecting the two spectral points is the same as the perpendicular to the crests of the function in the original domain. This is a crucial aspect that is employed to ascertain the principal orientations within the image [44], [47].

1.9.3 SPECTRUM

When displaying the frequency spectrum of an image, the convention is that the DC component is placed in the middle of the image and the frequency increases towards the edges [42], [44], [47].

The Matlab frequency spectrum search utilises the `fft2` function, which positions the DC component at [1,1], i.e. in the upper left corner of the image, and increases towards the centre. For an accurate representation of the amplitude spectrum, it is beneficial to employ the `fftshift` function, which alters the order of the displayed quadrants to align with the conventional convention [42], [47].

The spectrum is always composed of amplitude and phase components. The phase component of the image is of greater importance for human perception of the image content. However, the amplitude component, which interprets the representation of the individual frequency

components in the image, is more often displayed in the spectrum. The amplitude spectrum corresponds to the absolute value (magnitude) of the complex Fourier coefficients [42], [47].

1.9.4 DETERMINATION OF SIGNIFICANT DIRECTIONS IN THE IMAGE

One potential application of the amplitude spectrum in engineering is to identify significant directions within an image. This approach leverages the geometric relationship between the amplitude spectrum and the underlying real image. For instance, a vertical bar in the real image corresponds to a horizontal beam in the amplitude spectrum. This relationship is also observed in reverse, and for every general angle. Furthermore, the direction of the rays in the spectrum is always perpendicular to the structure of the real image [46], [47].

The transition from the original image to the amplitude spectrum represents a certain simplification of the perception of an often complex image. The amplitude spectrum is centrally symmetric (all rays pass through the centre), and only half of it needs to be used for analysis [46], [47].

A highly effective method for determining the dominant direction in an image is numerical integration of the amplitude spectrum along semi-lines that originate from the centre of the spectrum at different angles. However, the semi-lines have different lengths (the spectrum is rectangular). This would significantly affect the result, so it is necessary to perform the integration only along lines of the same length, i.e. inside the circle inscribed in the spectrum [46], [47].

In order to perform the calculation, a parametric expression of these segments is often employed, which are divided into a specific number of points with non-integer coordinates. The value of the spectrum at each point is determined by interpolating the values of the nearest pixels. The result of this integration can then be plotted on a graph, depending on the angle of the integration line. The maximum on this graph determines the angle that corresponds to the most significant direction of the structures in the analysed image [46], [47].

1.9.5 CONTRAST TRANSFORMATION

Contrast transformation is a set of image processing methods whose principal objective is to enhance the image in order to improve the visual perception of the observer. This process frequently involves the correction of uneven exposure and the removal of noise, although it should be noted that this may result in the loss of information. Some of these methods serve as preprocessing for subsequent more complex analyses, such as image segmentation.

HISTOGRAM

The histogram is intimately connected to the contrast adjustment of an image. The histogram of a grayscale image is a bar chart where each bar represents a specific grey level converted to the interval [0.1] and the height of the bars represents the representation (number of pixels) of that grey level in the image. In an image that has been exposed optimally, all grey levels should be approximately equally represented. The histogram can also be employed to identify the

threshold in thresholding segmentation. Once the histogram has been normalised (that is, the value of each bar is divided by the total number of pixels in the image), it becomes an estimate of the probability density function of the distribution of grey levels in a given image [39].

HISTOGRAM EQUALIZATION

Histogram equalization is the process of adjusting the brightness values of individual pixels so that the histogram of the resulting image is balanced, i.e. all columns are approximately the same height. It is a non-decreasing linear transformation. If there is an image $f(x, y)$, with dimensions $m \times n$ and composed of r grayscale levels with a histogram h^f. This image is to be transformed into another image $g(x, y)$ with a uniform histogram h^g that has q grayscale levels and retains the same size. It is evident that the pixel counts in each grayscale class in the histogram h^g should be equal to mn/q. [45] Histogram equalization is a non-decreasing linear transformation; therefore, each class in the output image can be calculated as the sum of several adjacent classes from the original image [43]:

$$h_1^g = \sum_{k=k_l}^{k_l+\Delta k_l} h_k^f,$$

(1.8)

The transformation curve takes the form of a step function designed to ensure that each class in the histogram of the output image approaches the value mn/q. A single class of the equalized histogram can be determined as the sum of consecutive classes in the histogram of the input image until the condition is met where the current sum is less than mn/q and adding another class would exceed this value. This condition can be mathematically expressed as follows: [43]

$$\sum_{i=0}^{k_l-1} h_i^f \leq \frac{lmn}{q} < \sum_{i=0}^{k_l} h_i^f,$$

(1.9)

where i represents the index of the class in the histogram of the input image, and l represents the index of the class in the histogram of the output (equalized) image. When creating the equalized histogram, there necessarily remain empty classes between the classes that were added to neighbouring classes. The equalization using a step function is illustrated in Figure 1.11 [42]
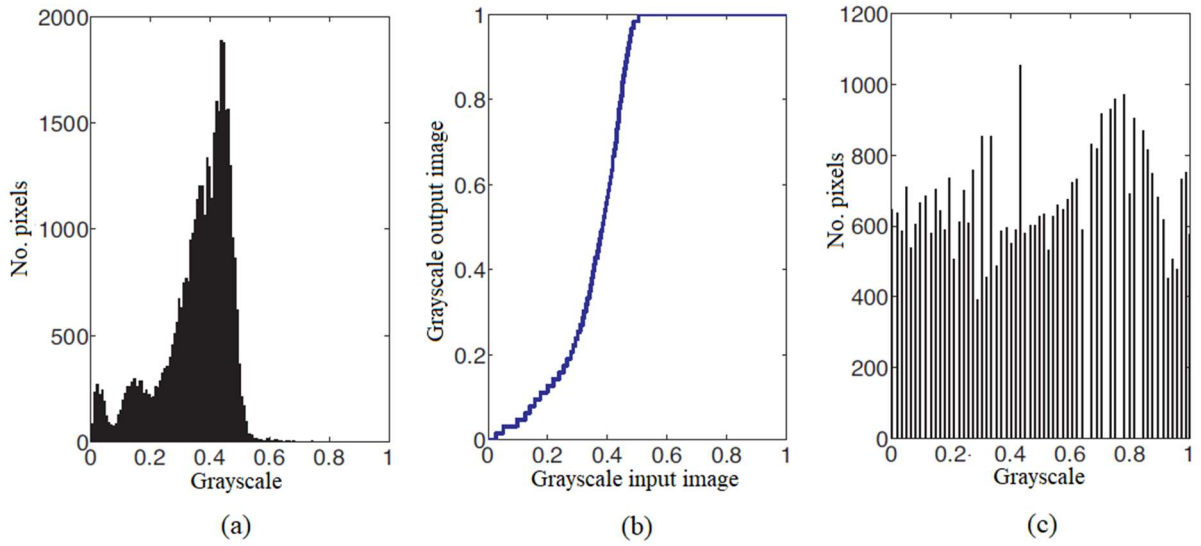
Figure 1.11 Histogram equalization of a grayscale image: (a) original image histogram (b) stepwise non-decreasing transform function Histogram equalization (c) image histogram after equalization [42]

LINEAR TRANSFORMATION FOR UTILIZING THE FULL RANGE OF GRAYSCALE LEVELS

Another method to adjust the exposure of an image is through the linear transformation of the histogram. This method does not aim to create a balanced histogram for the output image, but rather to utilize the entire range of grayscale levels. The design of this transformation function can be demonstrated through a simple consideration.

Suppose we have an image where the lowest grey level is 0.2 and the highest grey level is 0.7. To use the full range of grayscale shades, the minimum value in the image needs to be set to 0. This is done by subtracting the minimum value (here, 0.2) from the entire image. Subsequently, all the values in the image are divided by the difference between the highest and the lowest values in the image, which in this case is 0.5. This operation preserves the lowest value of the image ($0/0.5 = 0$) while shifting the highest value to 1 ($0.5/0.5 = 1$). The values of other pixels between these extreme values are linearly spread across the interval $\langle 0; 1 \rangle$ [42].

In addition to linear transformation, exponential transformation or gamma correction is often used in practice as needed. The properties of an image transformed by a nonlinear function are very different and depend on the type of function used and its parameters. Depending on the base used for the exponential function, these transformations can enhance the intensity of light pixels or, conversely, increase the contrast in dark areas. An example of an exponential transformation function is as follows [42]:

$$g_{i,k} = a^{f_{i,k}}, \tag{1.10}$$

where a is the base of the exponential function, $g_{i,k}$ are the intensity values of pixels in the output image, and $f_{i,k}$ are the intensity values of pixels in the input image.

In addition to exponential transformation functions, gamma correction is also widely used, which is defined by the formula [42]:

$$g_{i,k} = f_{i,k}{}^{\gamma},\tag{1.11}$$

where γ is the gamma parameter that usually takes values in the range $\langle 0,6; 2,5 \rangle$.

By changing the gamma parameter, it is possible to increase contrast in areas of low intensity (for $\gamma < 1$), or conversely, in areas of high intensity (pro $\gamma > 1$). If $\gamma = 1$ the output image is equal to the input image. A major advantage of gamma correction is that it does not change the brightness range of the image, meaning the maximum and minimum brightness values remain preserved after the transformation, thus additional normalization is not necessary. [42], [45]

2 EXPERIMENTAL PART

The experimental part of this thesis focuses on developing a methodology for analyzing abnormalities in CT scans of a specific type of gascooler. For this purpose, a procedure was designed, which was then transformed into an algorithmic form and significantly automated. During development, the algorithm was fine-tuned on eight pieces of gascooler to optimize its accuracy and efficiency. Subsequently, this algorithm was tested on two additional pieces, which allowed for the verification of its universality and robustness. The results of the algorithm were then confronted and compared with results obtained by traditional manual evaluation, enabling an objective assessment of the accuracy and efficiency of the proposed solution.

2.1 DEFECT ANALYSED

Within the experimental section of this thesis, a specific defect type of a clogged channel on the tube at the point where the tube enters the collection manifold was examined. This type of defect was identified on the gascooler model, which was introduced into mass production in 2023. A visualization of a representative defect is shown in Figure 2.1.
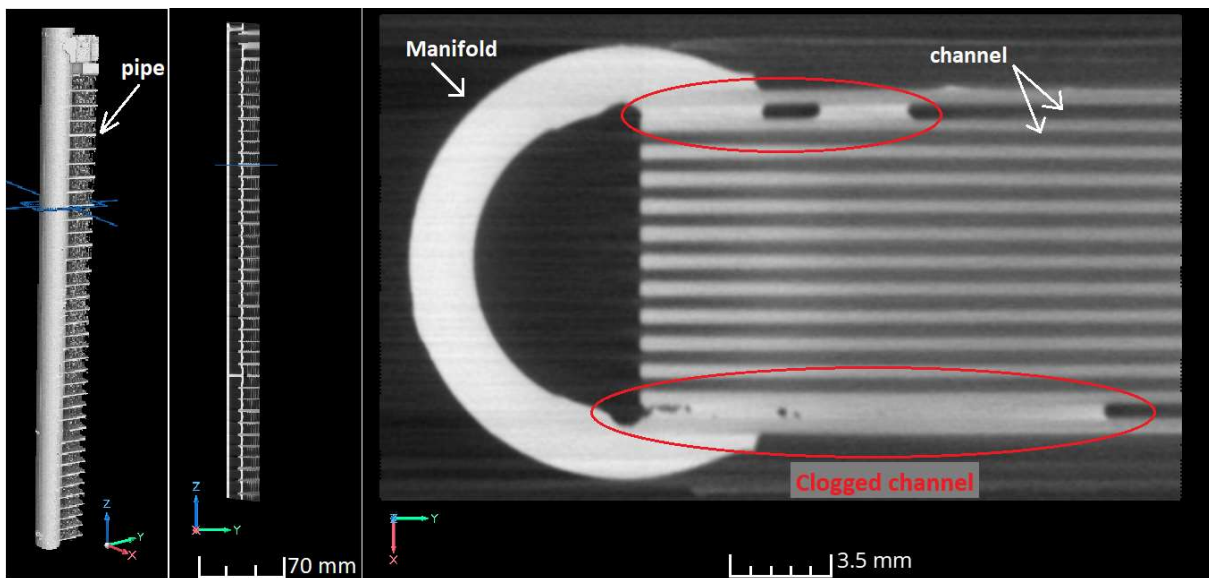

Figure 2.1 Clogged channel in the gascooler.

2.2 CAUSE OF THE DEFECT

Clogged channels at the point where they enter the manifold represent a relatively common problem for this type of gascooler. This defect usually occurs during the manufacturing process. During soldering, a special chemical agent is applied to the parts being joined, which promotes the decomposition of aluminium oxides on the surface of the contact areas at elevated temperatures. The entire component is heated to a higher temperature until the passivation layer of oxides dissolves and the surface of the mating areas melts. When the melted surfaces come into contact, an inseparable joint is formed. The clogging of the channels occurs if the melted material flows into the openings of the channels. Due to the very small dimensions

of the channels, capillary pressure acts at their openings, contributing to the penetration of liquid metal inside the channel, where, upon solidification, the metal leaves irreversible damage. The process is illustrated in Figure 2.2.
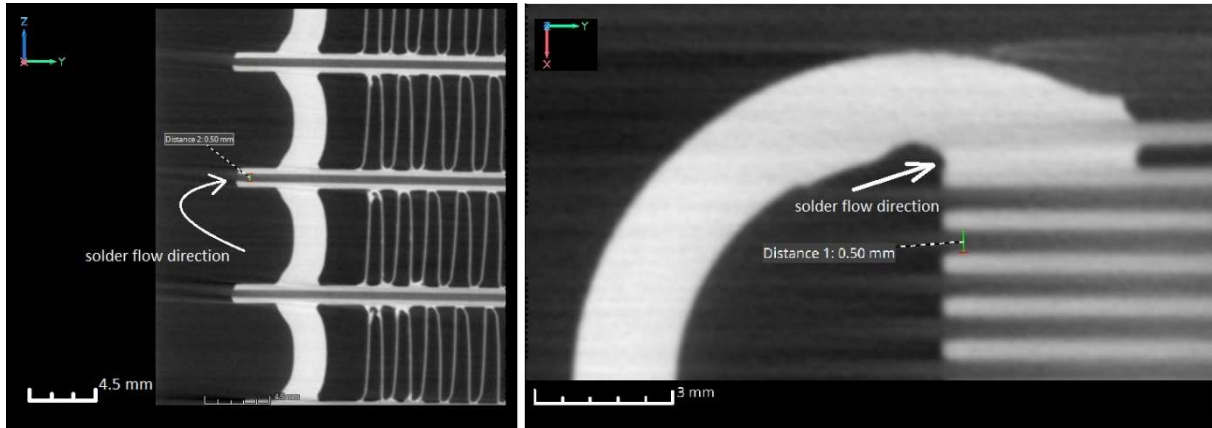

Figure 2.2 Solder flow direction.

This technology requires very precise adjustments of several parameters including the chemical composition of the solder material, its amount, the intensity of component heating, soldering temperature, and the duration of exposure to this temperature. Incorrect calibration of the technology leads to solder flowing into the openings of the channels, and its subsequent wicking.

2.3 CONSEQUENCES OF THE DEFECT

The infiltration of metal solder into the channels inevitably leads to their clogging and thus to irreparable damage. This obstruction has negative impacts on the overall functionality of the gascooler, particularly by increasing pressure losses in the coolant as it passes through the system. As a result, the volume of coolant passing through is reduced, which directly affects the cooling performance of the device. This reduction in performance can lead to inefficient cooling and increased energy demands of the gascooler, which ultimately means higher operating costs and reduced reliability of the device.

2.4 CURRENT APPROACH TO DEFECT ASSESSMENT

Given the serious consequences that clogging of channels brings, this abnormality is strictly monitored. Quality control is conducted using both destructive and non-destructive methods. In destructive testing, the manifold of the tested piece is cut off, as shown in Figure 2.3, and the openings of the channels are then carefully inspected using a magnifying glass. The results are recorded in an Excel spreadsheet and evaluated, determining the percentage of contamination for the specific piece. Based on these results, adjustments are made to the manufacturing process parameters to optimize it.

Figure 2.3 Destructive method of investigation clogged channels.

In addition to destructive tests, non-destructive testing methods such as Computer Tomography (CT) scanning are also used to verify the quality of pieces. This technology allows for the creation of a highly accurate digital reconstruction of the examined piece, often referred to as a digital twin. Based on this reconstruction, possible abnormalities or damage to the piece can then be efficiently identified and analysed using specialized software.

2.4.1 CT SCANNING

Scanning of pieces for development or production purposes is carried out by the Central European Institute of Technology (CEITEC) based on a contract with Hanon Systems Autopal s.r.o. After the scanning is completed, CEITEC provides Hanon with the digital CT data in *.vgl* format, known as the digital 3D twin. This data can be viewed through the freely available myVGL viewer offered by Volume Graphics.

Only the manifold area of the gascooler is scanned due to its larger dimensions. This area is marked in Figure 2.4. Due to the limitations of scanning technology, both the left and right areas of the component are divided into four sections. To ensure the complete scanning of the entire component, marks are applied to the manifold using adhesive from a glue gun. This material was chosen for its sufficient reflectivity, which ensures its recognizability within the resulting CT reconstruction, while simultaneously not creating undesirable artifacts. The marks primarily serve to facilitate easy navigation between the scanned sections on the examined piece and ensure that the operator scans each area from one mark to the next, always with a slight overlap, to ensure the continuity of the scan.

Figure 2.4 Destination of the area being scanned.

2.4.2 COORDINATE SYSTEM DEFINITION PROCESS AND CT DATA EVALUATION

After the CT data reconstruction is completed, the operator defines the coordinate system using the Simple Alignment tool. The data are then saved and sent to Hanon Systems, where they undergo evaluation. A specialist opens the data in the myVGL software, a freely available CT image viewer, and carefully scrolls through the individual planes of the tubes to gain an overview of the condition of each channel. The adhesive marks on the manifold help the specialist efficiently determine the sequence of the tubes and assign them to the corresponding slices, which is crucial for accurate evaluation. Identified defects and their positions are subsequently manually recorded in a Microsoft Excel spreadsheet. Figure 2.5 shows a part of the manifold with the CT reconstruction, where the adhesive marks are clearly visible.
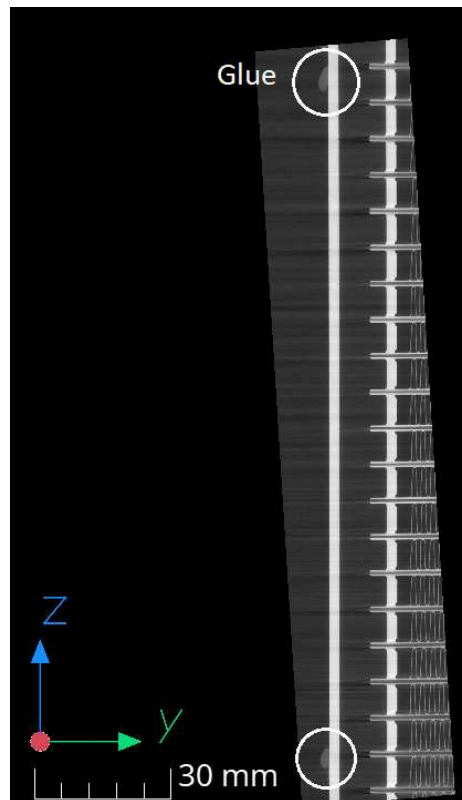
Figure 2.5 CT scan of the part of the
manifold with the glue mark.

2.4.3 ESTABLISHED PIPE AND PORT MARKING

For clear communication within Hanon Systems, a system for labelling each tube and channel was developed. The labelling is based on the orientation of the gascooler, as shown in the Figure 2.6.

CT reconstructions from the left side of the gascooler are marked with an "L", while those from the right side are marked with an "R", as illustrated.

Each tube is numbered from 1 to 72 according to their order. Tube number 1 is always located in part L4 or R4, respectively.

Each tube contains 12 channels. The numbering of the channels is arranged such that the channel located at the top in the orientation according to the Figure 2.7 is labelled number 12. Conversely, the channel that is located at the bottom in this orientation, closest to the base, is labelled number 1.
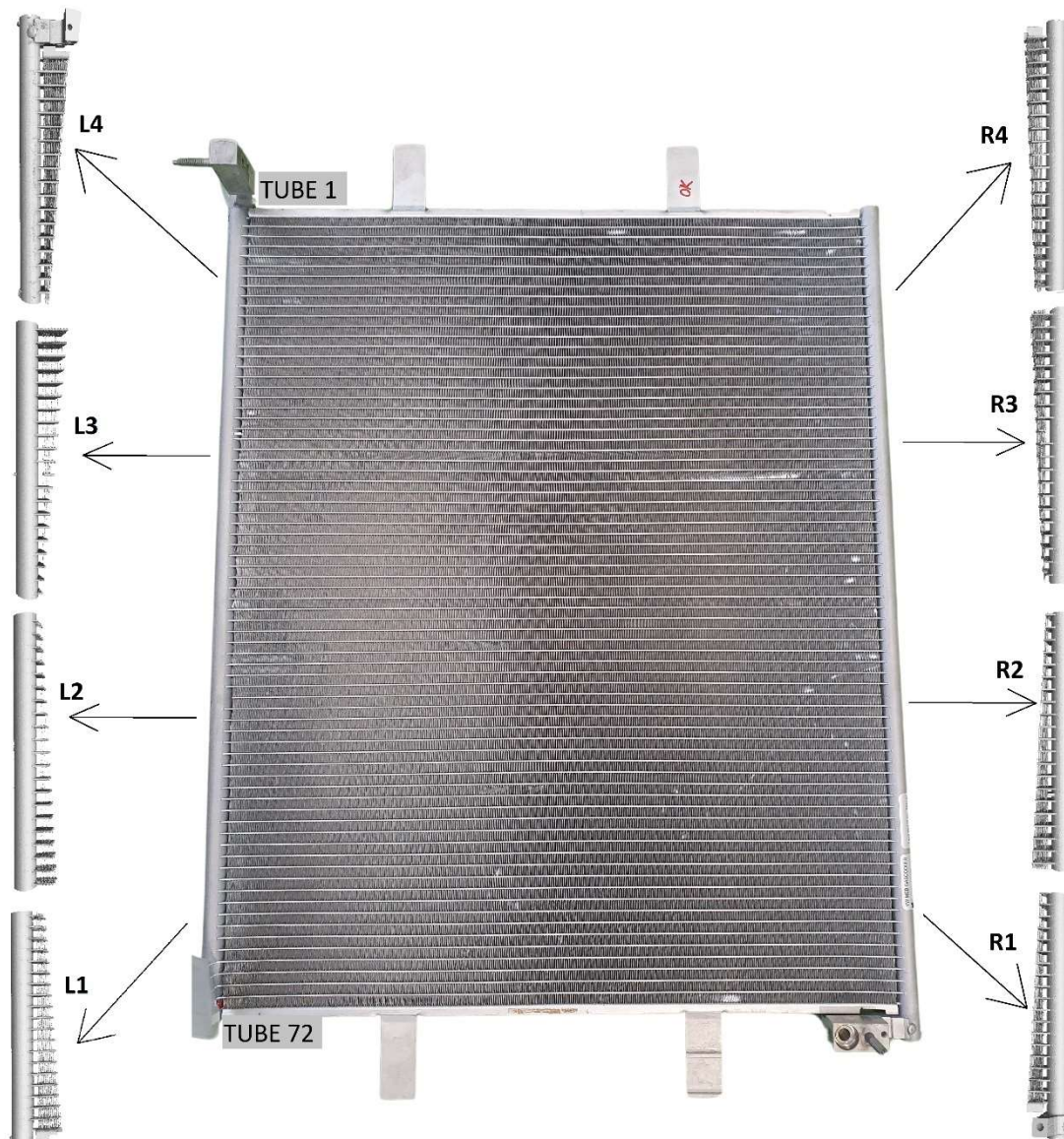
Figure 2.6 Marking of individual parts of the gascooler for scanning and numbering of pipes.
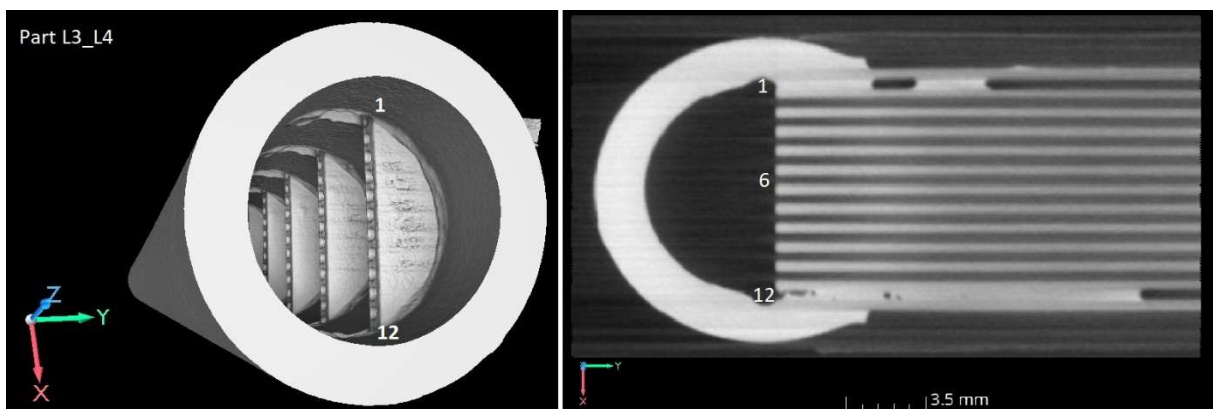

Figure 2.7 Marking of channels on left side.

2.5 DESIGN OF AN ALGORITHMIC PROCEDURE FOR CT DATA EVALUATION

 Previously used approaches to anomaly assessment typically involved manually reviewing CT reconstructions. Due to the high time and financial costs of the entire process, efforts are being made to algorithmize and automate this process. The new method utilizes the already established advanced software tool VGSTUDIO MAX and custom scripts in Matlab. The algorithmic approach to evaluating CT data should ensure repeatability and good reliability of assessments, and allow for partial or full automation. The goal is to reduce the financial and time costs of this process. The diagram of the process as generally proposed is shown in Figure 2.8.
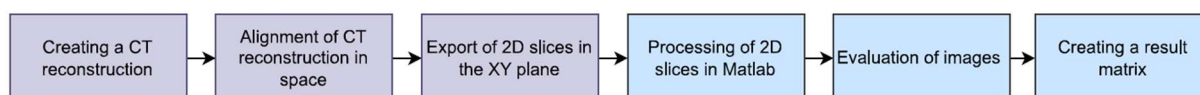

Figure 2.8 General diagram of the CT data evaluation process.

2.5.1 COMPLICATION IN THE ALGORITHMIZING OF THE CURRENT CT DATA EVALUATION PROCEDURE

The current process of evaluating CT data contains several aspects that complicate its full algorithmizing. One of the main challenges is the non-uniform division of the gascooler into individual scanned areas. This is due to the approximate nature of the division and manual application of adhesive, which can lead to variations in the number of tubes scanned between individual sections. Another issue is the adhesive marks themselves, which vary in shape and size and are not always placed directly opposite specific tubes. These marks also often lack sufficient contrast, which does not hinder the manual orientation of a human operator who can determine the order of the tubes based on them. However, for digital identification of these marks and subsequent recognition of specific tubes in CT scans, this would pose a significant challenge.

Each side of the gascooler is divided into four scanned areas. Two of these CT reconstructions are obtained from the edge parts and two from the central part of the device. Details of this division and the placement of individual areas are shown in the Figure 2.6.

For parts L2 and L3 or R2 and R3, which are located in the central part of the gascooler's side, there is a risk of incorrect orientation of the CT reconstruction around the tube axis, as illustrated in the Figure 2.9. These areas usually do not contain distinctive shape elements that would allow the identification of the section's orientation. This can easily lead to a mistake where the top side of the reconstruction is turned upside down, leading to incorrect identification of tube positions and potentially invalidating overall results. Since the establishment of CT data in space is currently done manually, this error is usually eliminated by the CT scanner operator. In automatic evaluation, it is not effectively possible to verify whether the CT reconstruction from the central part has been turned to the incorrect position. Checking the orientation would only be possible based on the shape of the adhesive marks at the ends of each section.
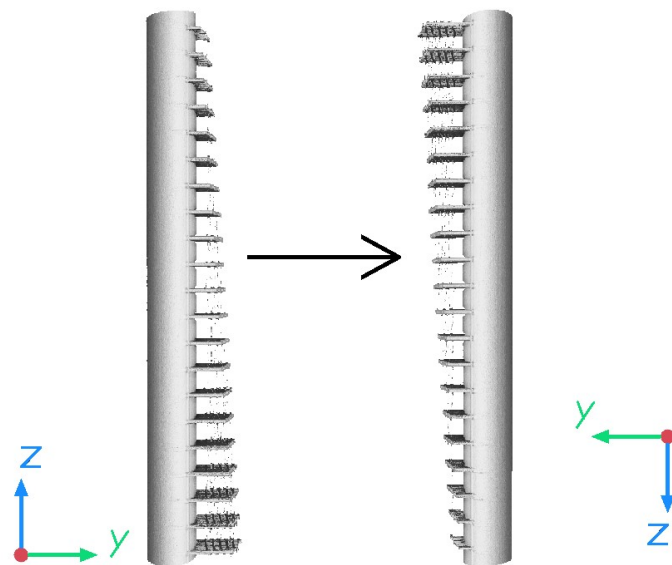
Figure 2.9 Illustration of rotating the image around the port axis.

2.5.2 USING MULTISCAN TECHNOLOGY

The issues of scanning and orientation of data have been effectively resolved using multi-scan technology, which allows for an increased range of the scanned area. The scanning process begins with the acquisition of one specified part (for example, L1); after its completion, the scanner automatically moves and begins to scan the adjacent area (in this example, L2). Once the initial setup is done, no further operator intervention is required. The movement of the scanner and the merging of data occur automatically. The software then combines both scanned parts into one complete CT reconstruction. The result is a reconstruction of double the size.
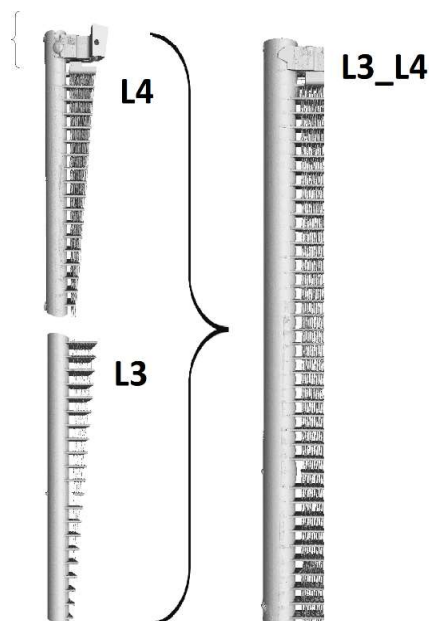

Figure 2.10 A scan from a multiscan.

This approach simplifies orientation in the resulting 3D data, as it allows for the entire left (L) or right (R) side of the gascooler to be scanned in just two images using multi-scan technology. Each image includes the edge part of the gascooler, which clearly defines the orientation of the CT reconstruction. An image from the multi-scan is shown in Figure 2.10.

2.5.3 IMPACT OF TECHNOLOGY CHANGE ON THE SCANNING PROCESS

The use of multi-scan technology in scanning introduces specific technical challenges and requires minor adjustments to the process. During scanning, the object is positioned between the detector and the source of X-ray radiation. Since aligning the edges of the object parallel to the incoming X-ray beams can lead to the formation of artifacts at these edges, it is necessary to tilt the gascooler at a certain angle. This tilt prevents the parallel incidence of the beams on the edges of the object and minimizes negative visual effects in the final image.

The inclination of the gascooler is the reason why the CT reconstruction is wedge-shaped. Although the examined area is only the entry of the channels into the manifold, due to the tilt, the scanned area must gradually expand. In the case of multi-scan, twice the length of the manifold is scanned in one clamping of the piece in the scanning device. This results in a double expansion of the scanned wedge. Therefore, the time for multi-scan reconstruction is not only twice as long as the previous approach but is also slightly extended due to the expansion of the CT data. Additionally, during reconstruction, the alignment of two scanned areas is performed, leading to a further extension of the reconstruction time.

The quality of the CT reconstruction, especially its resolution, is influenced by the amount of energy used during scanning and the distance between the source of X-ray radiation and the collimator. These parameters determine not only the quality of the image but also the duration of scanning and its cost. Therefore, emphasis was placed on maintaining these parameters. Despite the fact that multi-scan requires moving the piece during scanning so that after one part is imaged, the adjacent scanned area is moved in front of the X-ray source, a suitable spatial configuration of the clamping has been found so that the distance between the collimator and the source is not changed and the quality of the images is preserved. Clamping now represents a more challenging task with greater emphasis on accuracy to prevent collision between the scanned piece and the source of X-ray radiation during movement. A compensation for the more complex clamping is the fact that it is now done four times instead of eight, leading to an overall reduction in manipulation time and securing of the gascooler before scanning.

All changes ultimately led to a reduction in the total time for scanning and CT data reconstruction by 27.8%. The most significant influence on time savings was undoubtedly the fact that thanks to multi-scan, the entire gascooler can be scanned in four sections instead of the previous eight. The time savings are directly proportional to the savings in financial costs incurred for scanning a single piece of gas cooler.

Given the substantial advantages and only minor disadvantages of using multi-scan technology, it was adopted. The main arguments were the cost of the resulting CT reconstruction and the enhanced potential for algorithmizing.

2.6 CT DATA ALIGNMENT AND EXPORT OF SLICES

After successfully scanning a section of the piece and reconstructing the 3D digital twin, it is necessary to rotate the CT data in space into a predetermined coordinate system. Previously manual positioning has been replaced by an automatic process.

The coordinate system, according to which the CT reconstruction is defined in space, is determined by a digital 3D STEP model of the piece. This model is reduced to only the area of interest relative to the scanned part and is located in a known spatial arrangement. Attempts to align the CT data with the full model of the gascooler in automatic mode always ended unsuccessfully.

The definition of data in space utilizes the Best Fit function in the commercial software VGSTUDIO MAX, which allows the user to align reconstructed data with another 3D reconstruction, 3D mesh (.stl), or 3D CAD model (.step). According to the software tool's documentation, this function works with the least squares method. The entire process, including other necessary actions, is illustrated in the diagram on Figure 2.11. The functions used and their parameters were determined based on experimentation. All these steps were recorded into a macro, which performs them automatically and independently.
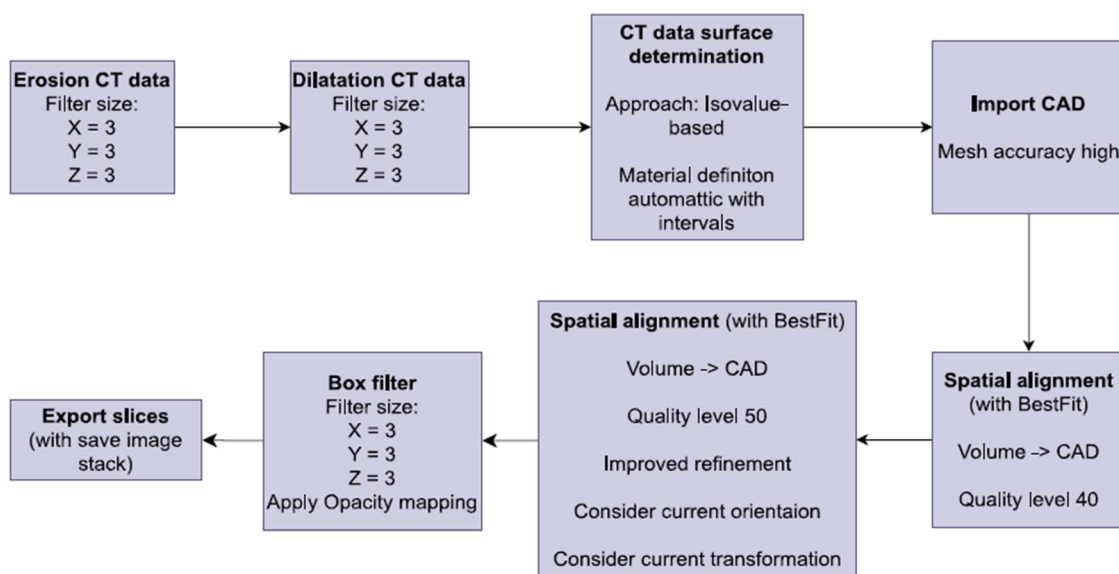

Figure 2.11 Macro diagram in VGSTUDIOMAX.

In addition to the Best Fit function, the automatic macro also utilizes erosion and dilation of data, which aim to remove small voxels scattered in the area between the channels' planes and to seal any pores on the surface of the CT data that could complicate alignment with the geometrically ideal CAD model. Small formations in the area between the channels arise during scanning, where in the actual piece this area contains corrugation. However, this structure is imprecisely captured and is not part of the CAD model. The presence of small geometric formations in the area between the channels unnecessarily complicates the alignment, hence the effort to remove these formations as well as pores before the actual alignment. The cross-section in the xy plane before and after erosion and dilation is shown in Figure 2.12.
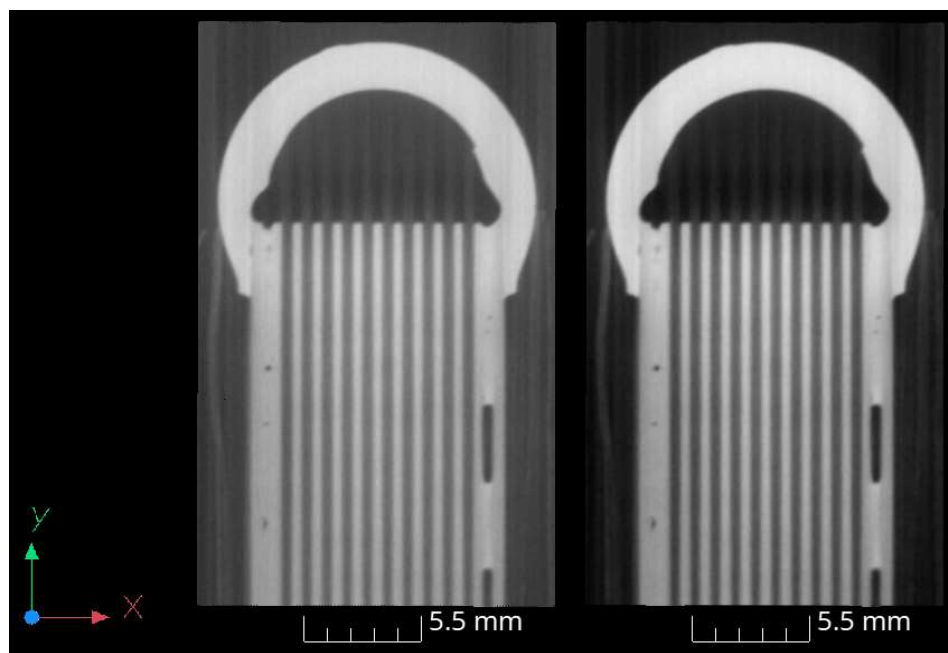
Figure 2.12 Section in the XY plane: Left before erosion and dilation, right after erosion and dilation.

Each of the four scanned sections is geometrically distinct and is always aligned with the CAD model that corresponds to the scanned section. The spatially aligned section with the corresponding CAD model is shown in Figure 2.13. Therefore, these macros are defined four times, individually for each section.
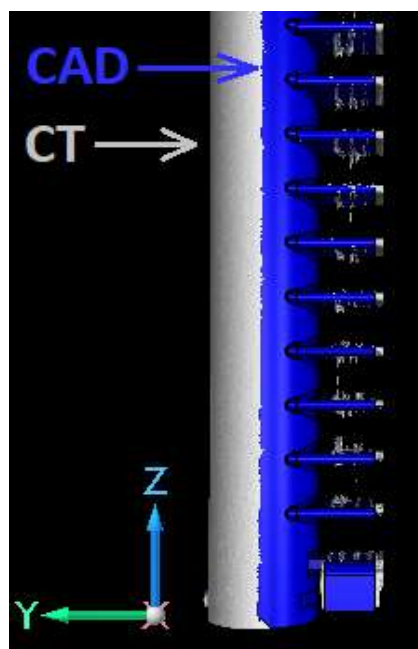

Figure 2.13 CT reconstruction aligned with a CAD model of the gascooler.

After successfully determining the CT data in space, slices in the XY plane are exported, on which the condition of the individual channels is clearly visible. The export always occurs in a defined order to determine which slice belongs to which tube. Since the channels are very

narrow and there is a risk that the plane of the cut will not be entirely parallel to the plane of the channels, 7 slices are exported from the area of each tube, spaced 0.04 mm apart and evenly distributed above and below the plane of the channels' axis of one tube. The areas from where the slices are made are shown in Figure 2.14. In the next phase of the algorithm, these slices are combined into a single image, ensuring greater robustness of the algorithm.
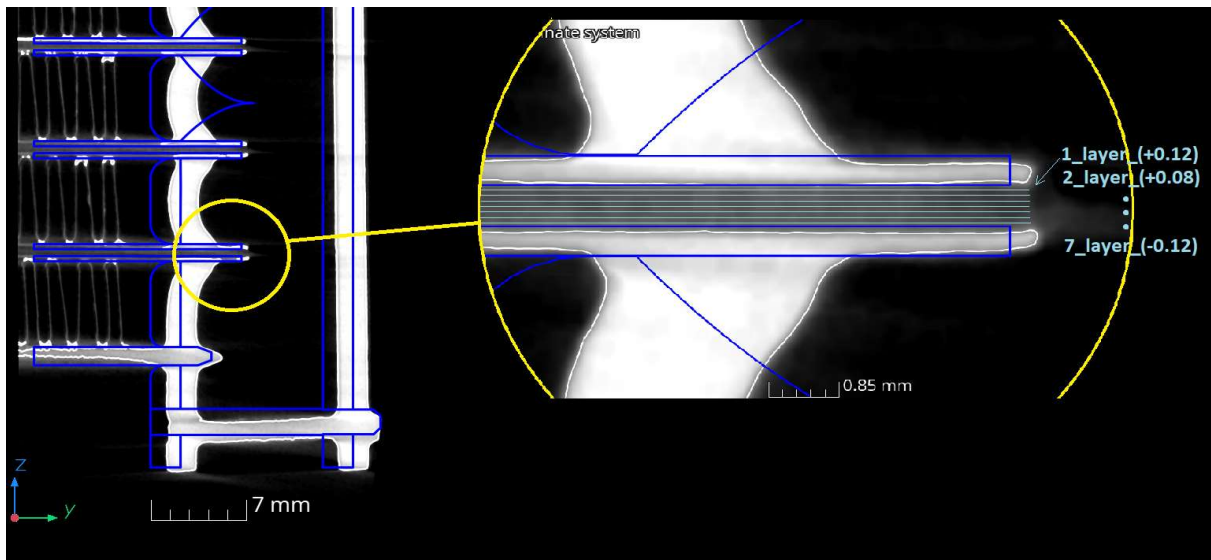

Figure 2.14 Planes from where sections within one pipe are exported.

2.6.1 DIRECTORY STRUCTURE OF STORED IMAGES

Each part of the gascooler has its macro, so there are four macros that contain the same functions and only differ in the CAD model they use for positioning the CT data in space. Each of these macros subsequently saves slices from defined planes into directories labelled according to the section from which the slices originate.

For the exported images, the following directory structure has been established, illustrated in Figure 2.15. All images are stored in a directory named "Sample_xx." In this name, the user changes "xx" to the number of the scanned piece after exporting all data. This directory contains four subdirectories, each named according to the scanned section ("Slices_L1_L2," "Slices_L3_L4," "Slices_R1_R2," "Slices_R3_R4"). Each subdirectory contains a further seven directories, which are named "1_layer_(+0.12)," "2_layer_(+0.08)," ..., "7_layer_(-0.12)." These directories house the actual images. The meaning of the names corresponds to the planes from which the given set is exported and is illustrated in Figure 2.14. The first number determines the sequence of the slice, and the number in parentheses indicates the distance of the slice from the axis of the channels.
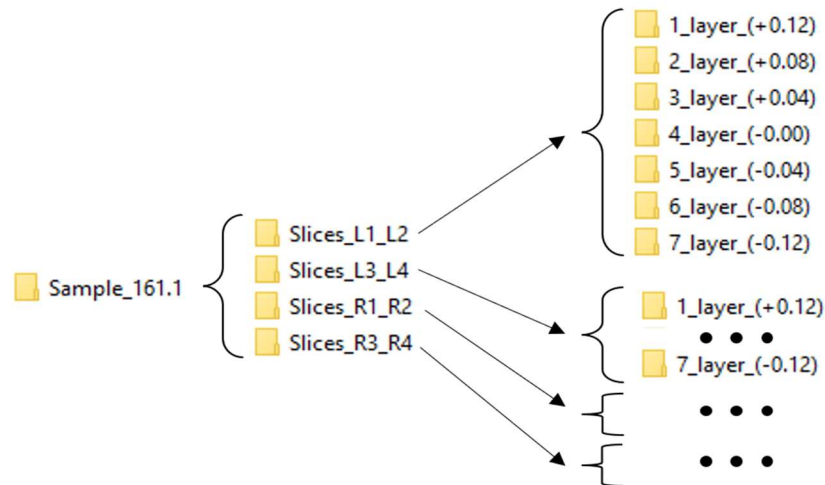
Figure 2.15 Directory structure.

2.6.2 RANDOM ERRORS IN AUTOMATIC CT DATA ORIENTATION

Although the CT data is filtered before aligning with the CAD model and the CAD model is reduced to the region of interest only, when using the Best Fit function, inaccurate fitting of the CT reconstruction and CAD model occurs in the sense of shifting the CT data in the Z-axis by a distance equal to a multiple of the spacing of the individual tubes. This error is illustrated in Figure 2.16. In order to ensure that images of all important locations to be evaluated are always exported from the CT reconstruction, the macro exports sections from multiple planes (specifically 50 planes). After evaluation, it is necessary to export slices from 36 planes. The extra plane images are distributed evenly over and under the CT data area, ensuring that if there is a shift in the Z-axis during downsampling, all important planes are captured. Consequently, some planes are situated above the CT data area, while others are located below
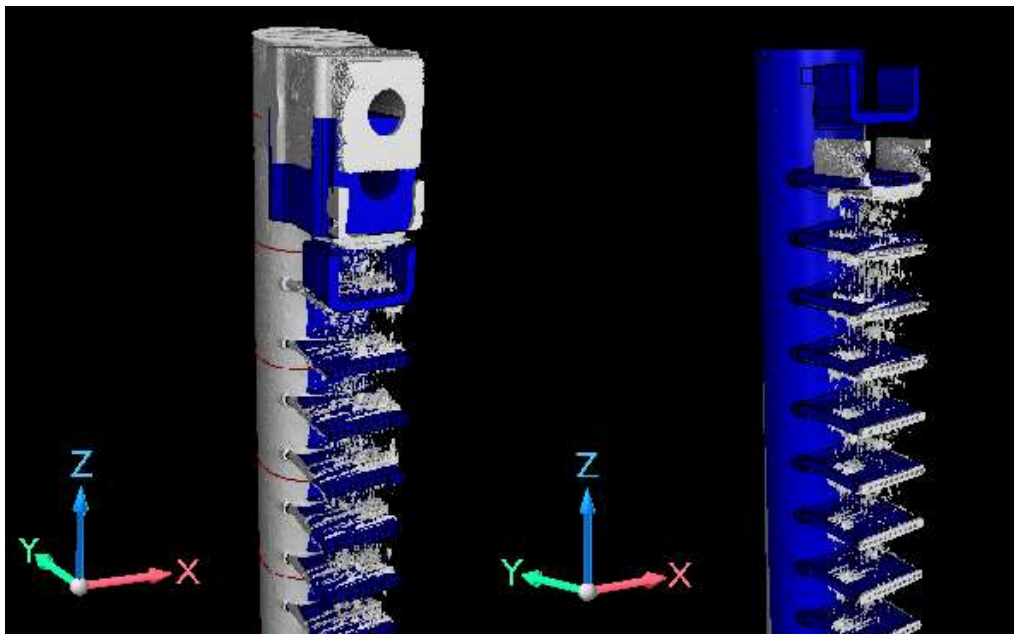

Figure 2.16 Shifted alignment of CAD model and CT data.

it. Consequently, the resulting image set always contains empty images – black (see Figure 2.24).

Another common deviation that occurs when setting up CT data is inversion, specifically rotation around the Y-axis (the axis of the channel). This is illustrated in Figure 2.17, which shows that the slices are exported in reverse order. The export of the slices is usually in the Z-axis direction, but if the scanned section is rotated, this is what causes the order of the exported slices to be reversed.
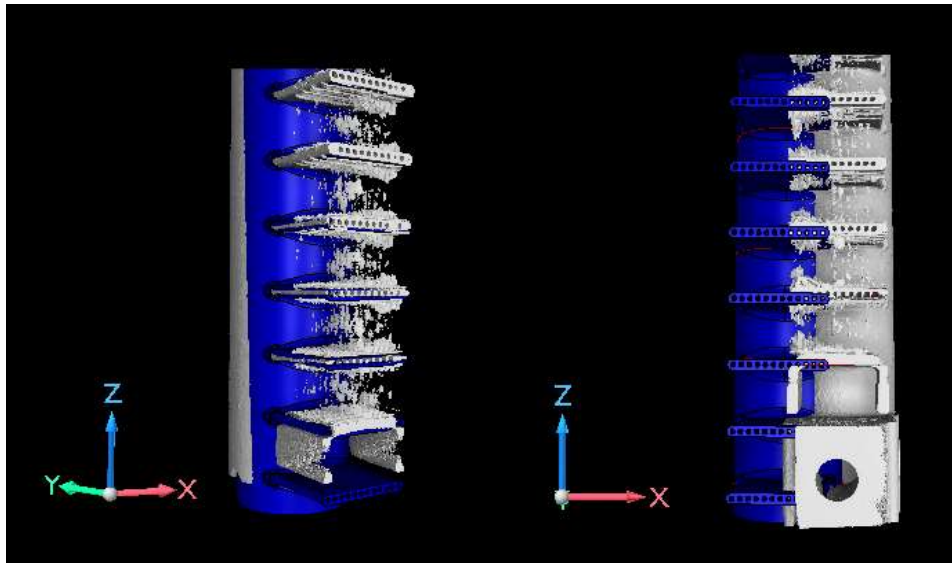

Figure 2.17 Incorrect alignment: turning the section upside down (around Y axis).

The second and most significant consequence of this error is that the slices are exported in a mirrored orientation. VGSTUDIO MAX always takes a cut in the XY plane in the view opposite to the Z-axis direction [49]. Consequently, if the section is rotated but the view is not rotated to create the cuts, the images are mirrored.

The third type of abnormality in the spatial definition of a CT reconstruction is its rotation about the Z-axis by an arbitrary angle. As illustrated in Figure 2.18, these angles are typically small, in the order of units of degrees. However, following alignment in space, a situation may arise where the reconstruction is rotated about the Z-axis by nearly 90° or 180°. Consequently, the exported images are also rotated by this angle, which must be compensated for subsequently.
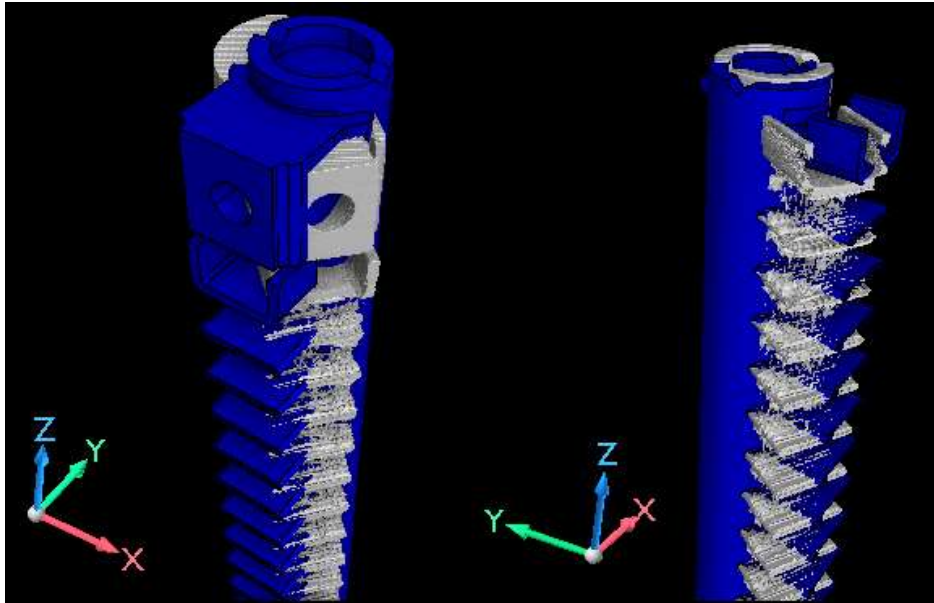
Figure 2.18 Incorrect alignment: Rotation around *Z* axis.

All of these situations occur randomly and independently of each other. They can occur individually or all at once and are the result of the Best Fit algorithm used in the commercial software VGSTUDIO MAX, which uses a least squares method implemented in an unspecified algorithm to descend. Therefore, in further evaluation, it is necessary to account for these anomalies and implement corrective mechanisms to avoid invalidating the results.

The spatial layout of the sections is shown in Figure 2.19. This layout is based on the actual orientation of the sections and is considered the correct and default configuration. Any deviation from this layout is considered an error in the spatial determination of the Best Fit functions.
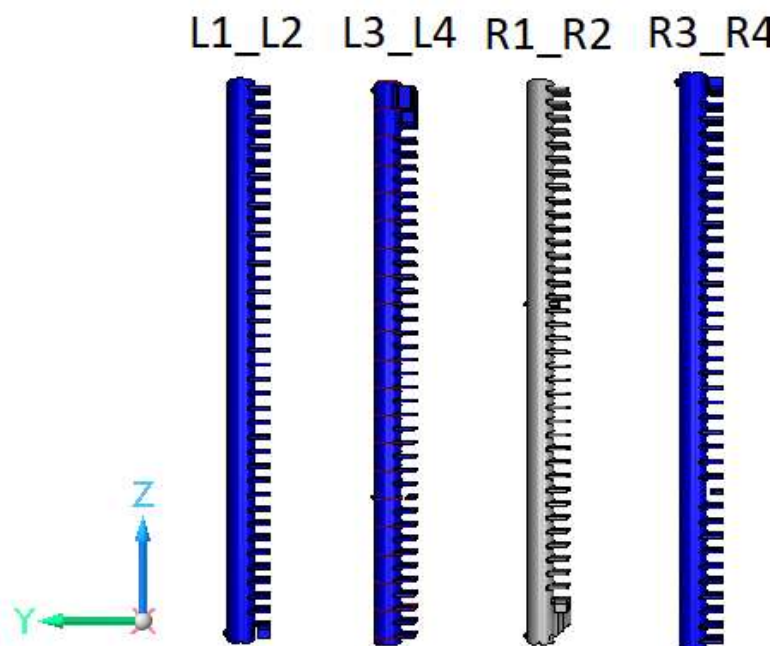

Figure 2.19 Default layout of sections in VGSTUDIO MAX

2.7 PROCESSING OF EXPORTED SLICES IN MATLAB

In the initial phase of the proposed algorithm, the CT data was established in space utilising the automatic functions of the VGSTUDIO MAX software. Subsequently, sets of sections with defined spacing in planes parallel to the plane of the channels were exported. In the second phase of the algorithm, these images are processed using a script in Matlab software. The script employs advanced features of the Image processing toolbox library from MathWorks and custom functions designed to address specific issues in the evaluation process.

The output of this stage of the algorithm is a script that generates a matrix of ones and zeros from the exported section directories. The structure of the resulting matrix corresponds to that of a previously established matrix, which was created by a specialist in charge of CT data evaluation at Hanon.

2.7.1 PREPROCESSING

The image processing function in Matlab is also divided into sections. At the outset, the user is prompted to select the folder containing the images of the gascooler being evaluated. The user is required to select one main folder labelled "Sample_" and the number of the specific piece. At this juncture, the script verifies that this marked directory includes subdirectories containing the evaluated snapshots with predefined names. If the directories are missing, the user is informed of this.

The path to this directory is then passed to the `makeImds` function, which creates four Image Datastores from each section. An Image Datastore is a structure used by the Image Processing Toolbox to facilitate faster processing of images. This structure is employed throughout the algorithm, entering each of the individual functions. Prior to its creation, it is verified that there are no Temp or Eval subdirectories remaining from a previous run of the software.

Seven slices are exported from a single channel plane region, as illustrated in Figure 2.20. One representative image is to be created from this data. To this end, the function `processRawImages` was created. Prior to calling this function, the number of slices exported from one plane of channels (according to the number of directories) is checked. This information, together with the image datastore, forms the input to the `processRawImages` function. This function has no output. Upon invocation, a representative image is generated and stored in the temporary directory.

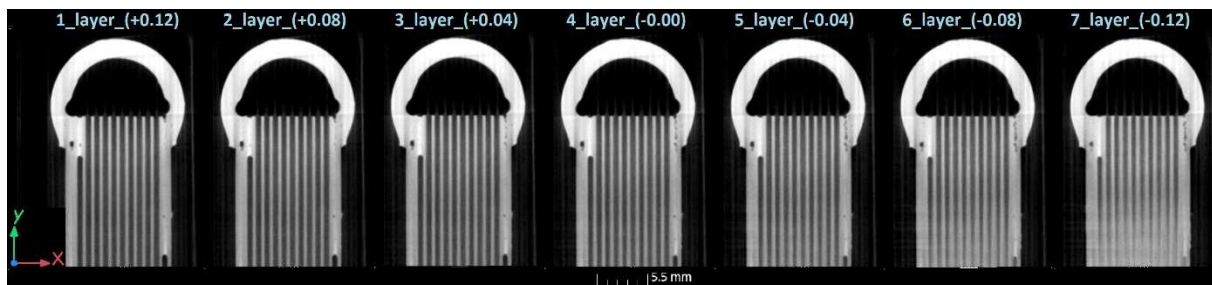Figure 2.20 A set of images from a single pipe area.

A representative image is created by combining all seven images. This is achieved by having the `processRawImages` function read all seven frames and compare the values of the corresponding pixels. The resulting image then contains at each position the lowest pixel value found among all seven images. If any of the frames is partially or completely outside the

channel plane, its pixel values are not considered in this examined region because the pixels are dark in the channel region. The resulting image is shown in Figure 2.21.
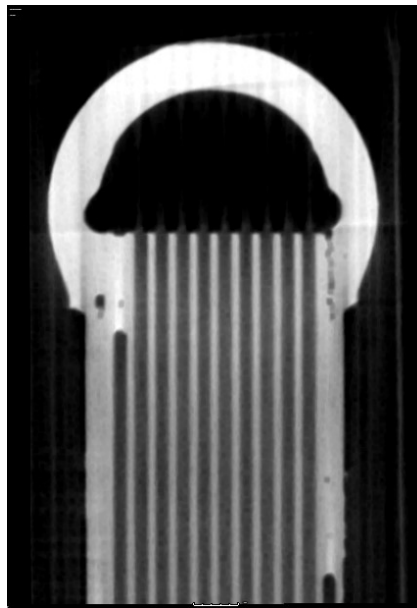

Figure 2.21 Single pipe composite image
produced by the `processRawImges` function.

2.7.2 IDENTIFICATION AND ASSIGNMENT OF SECTIONS TO INDIVIDUAL PIPES

Following the processing of the images and their saving to the Temp folder, the directory contains a total of 50 images with indexes 1 to 50. The next step is to identify the channel snapshots and assign them a number that corresponds to their position on the gascooler. Due to errors in CAD model downloading and CT reconstruction in VGSTUDIO MAX, more sections are exported than are needed for evaluation. It is therefore necessary to identify the images that will be evaluated and separate them from the others.

This is achieved by utilising the `FindSideSupp` function, which is used to locate the gascooler edge section among all the slices. This section is referred to as side support in Hanon terminology. This cut corresponds to the position before and after the first and last evaluated cut, respectively, and is geometrically distinct from the other cuts. It can be easily identified. Figure 2.22 illustrates the side support, transition, and following frames.
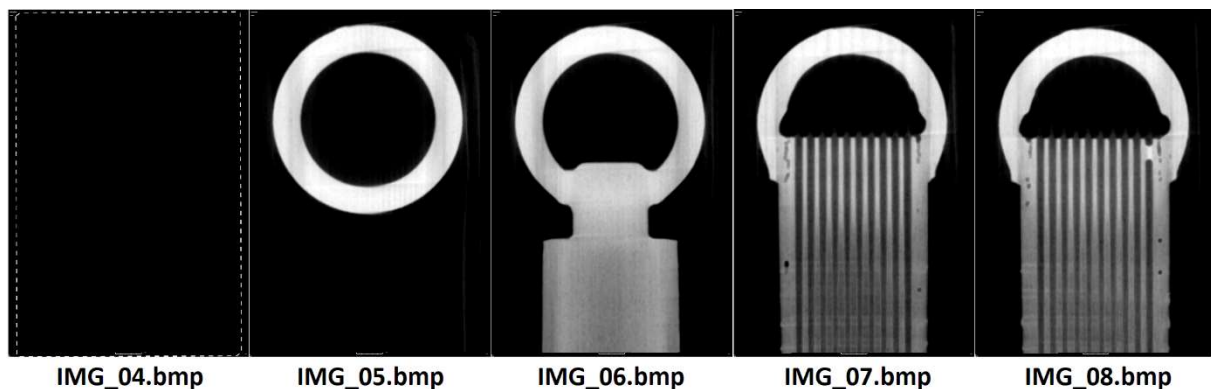

IMG_04.bmp   IMG_05.bmp   IMG_06.bmp   IMG_07.bmp   IMG_08.bmp

Figure 2.22 Side support (IMG_6.bmp) and surrounding images in the exported slice set.

In order to identify this image, a two-phase correlation is employed, whereby the selected images are compared with a representative side support image. Initially, all empty frames within the Temp folder are identified and subsequently discarded from further processing, thus reducing the total number of frames. Assuming that the entire gascooler section has been scanned, the folder must contain a minimum of 36 consecutive slices through each pipe for evaluation. Consequently, the side support is typically identified from the 37th non-zero frame onwards. For instance, if there are 38 non-zero frames in the folder, the 37th and 38th non-zero frames are examined, as well as the 1st and 2nd non-zero frames in the event that the order of the frames in the folder is reversed for some reason.

The image with the highest correlation coefficient is identified and designated as the boundary image for the entire section.

The Matlab function normxcorr2 is employed to calculate the correlation coefficient. This function performs a two-step correlation between the template and a specific image. The output of this function is a matrix of correlation coefficients, c, which indicate the degree of correspondence between the template and different parts of the image. The correlation coefficients can take values in the interval $[-1, 1]$, where a value of -1 indicates a very weak or no match and a value of 1 indicates a very strong match between the image and the template. The maximum value in this matrix is considered as the correlation coefficient of the investigated image and the template.

Then, the correlation coefficients of each examined image are compared. The image with the highest correlation coefficient should be the most similar to the template among the investigated images. This image is considered to be the side support structure image and its index is stored. A dialog box appears and displays to the user the frame that has been identified as the initialising frame using the two-phase correlation.

Figure 2.23 Dialog box asking if the side supp has been correctly identified.

The dialog box is shown in Figure 2.23. The user has the option of answering the question of whether the frame was correctly identified by selecting "Yes" to confirm the correct identification, or "No" if the frame was incorrectly identified. Should the user select "No", the

software will prompt them to manually select the snapshot and automatically verify the folder in which the initialization snapshot is to be identified.

In the event that the user indicates an error in the identification of the initialization snapshot, `ConfirmSideSupp` corrects the stored index of the initialization snapshot. This corrected index, in conjunction with the Image datastore of the section being evaluated, is then input to the `vectOfEvalImg` function. This function creates a vector of image indices to be evaluated. The order of the indices in this vector corresponds to the sequence of channel planes on the scanned piece.

The ordering of the indices is contingent upon the index position of the Side Support image. If this index is situated in the initial portion of the image set (with indices ranging from 1 to 25), the images to be evaluated possess higher indices than the initialization image and are situated subsequent to this image. Conversely, if the index of the Side Support frame is in the second half of the set (with indices ranging from 26 to 50), the evaluated frames have lower indices than the Side Support frame. This is the case if the index of the frame in question lies in the folder before this frame. To illustrate, if the Side Support frame has an index of 43, the software will ascertain that the evaluated frames have lower indices than this frame and construct a vector of evaluated frame indices in the order 42, 41, ..., 7. A Temp folder containing the entire set of frames where this issue can be more clearly observed is shown in Figure 2.24.

Figure 2.24 Set of images in the Temp folder (Sample 161, part L1_L2).

The spatial arrangement of each section is fixed and illustrated in Figure 2.19. Images of each section in the XY planes are exported in the Z-axis direction, from the bottom of the reconstruction upwards, using the VGSTUDIO MAX software. Therefore, the arrangement of the images in the Temp folder for each section is known in advance. In sections L1_L2 and R1_R2, the side support image should appear at the end of the set of evaluated sections. Conversely, in sections L3_L4 and R3_R4, the side support frame should appear at the beginning of the set of frames. It is of the utmost importance to verify this sequence of images in order to identify and rectify any spatial misorientation of the CT reconstruction in a timely manner.

In order to evaluate a section correctly, the `vectOfEvalImg` function reads the Image datastore path and identifies which section is currently being evaluated. It then checks if the position of the side support image matches the expected position in that section. If it does not, it can be concluded that the CT reconstruction in VGSTUDIO MAX has been spatially reversed according to the slice plane, and that the images have been incorrectly arranged (Figure 2.17). Should such an error be identified during this process, the `vectOfEvalImg` function will adjust the order of the indices in the output vector, and additionally set the "mirroring" flag to "true" for that section. This flag indicates that all slices of this section are VG Studio export slices viewed against the Z-axis direction. If the section is inverted in this direction, the view of all slices is rotated, which is the reason for the apparent mirroring of the images. The creation of the mirrored images due to "upside-down" orientation od section is visualized in Figure 2.25.
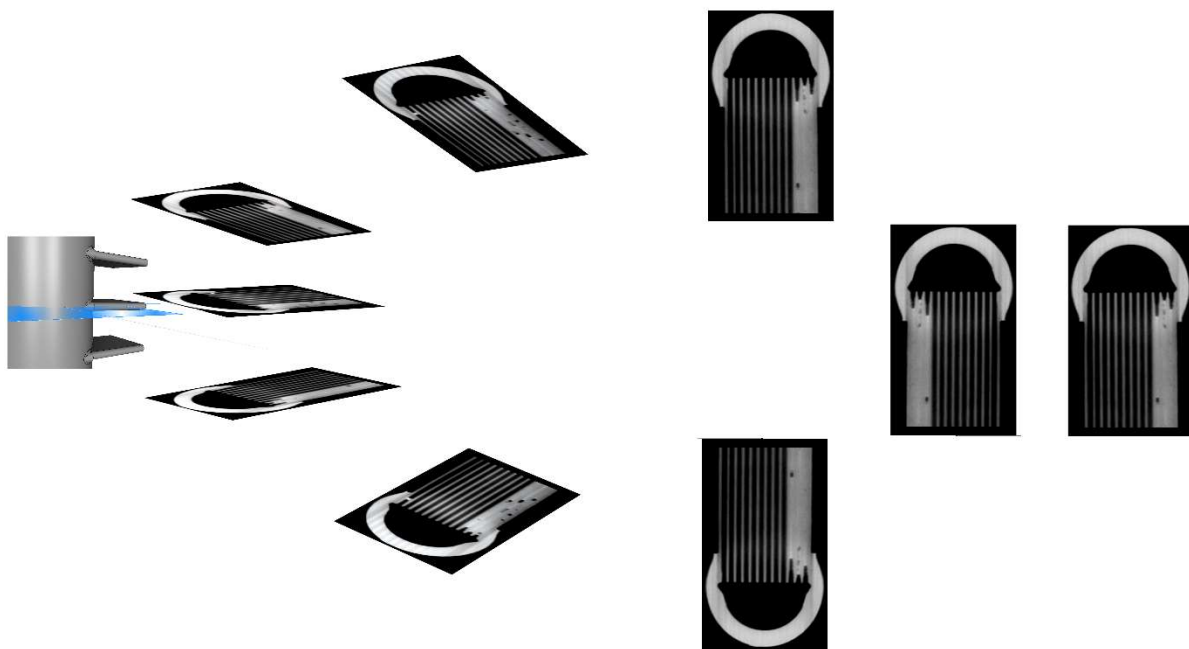

Figure 2.25 Visualization of creation the mirroring images.

Then the `PickImgToEval` function is called, whose input is an ordered vector of indexes of the evaluated frames, Image datastore of the evaluated section and the mirroring flag. This function then modifies the images and saves them in the Eval folder.

2.7.3 EXPORT OF SLICES TO EVAL FOLDER

The `PickImgToEval` function is responsible for saving images to the Eval folder. Initially, this function performs a check to ascertain which section of the gascooler is currently being evaluated. It then retrieves the images according to the vector of evaluated image indices, which it assigns numbers from 1 to 72, corresponding to the original slice position. Following minor adjustments, these images are stored in a temporary Eval folder. A diagram of the `PickImgToEval` workflow is presented in Figure 2.26. During processing, the function rotates the images to the correct orientation, crops, adjusts contrast, resizes the images to 600 pixels wide, and mirrors the images if necessary for the section.
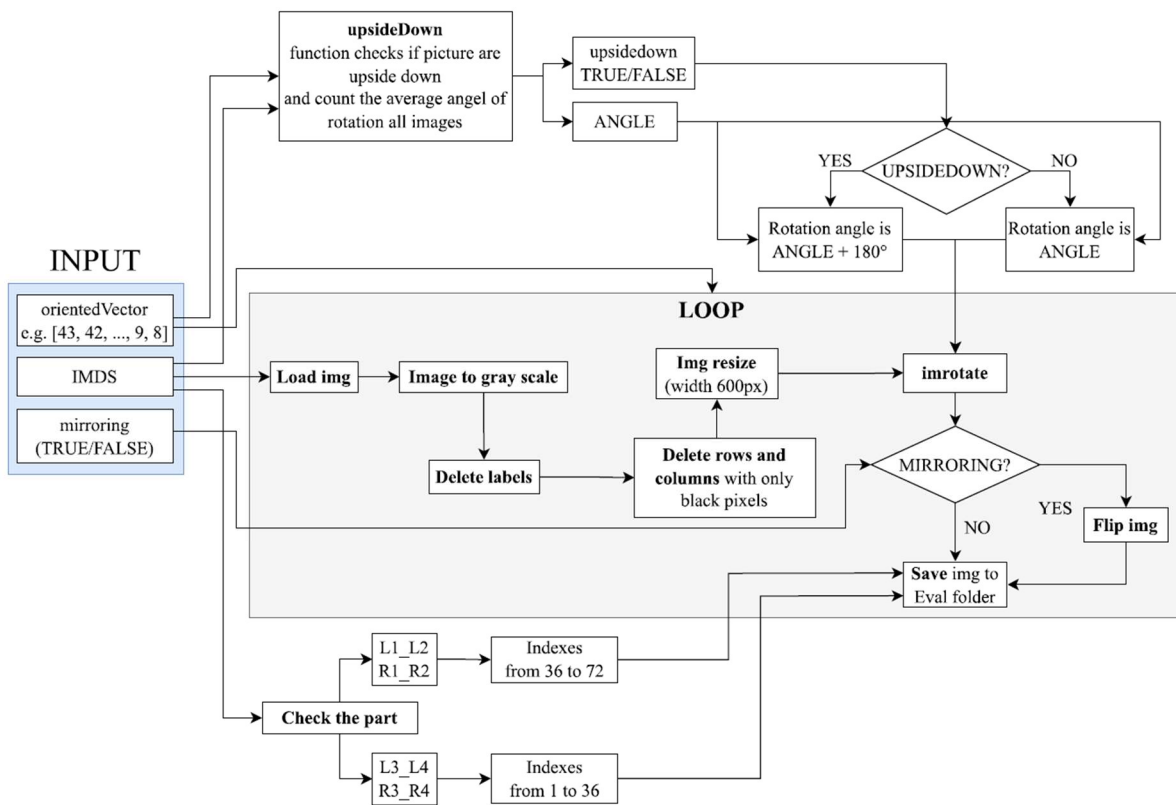
Figure 2.26 Schematic of the `PickToEval` function.

During processing, the image labels are removed from the images, which contain scale and other accompanying information that is unnecessary for image evaluation. Furthermore, all rows and columns of pixels that carry only black colour are removed from the images. This is the background, and the image is thus cropped to the region of interest only. The image after editing is shown in Figure 2.27.
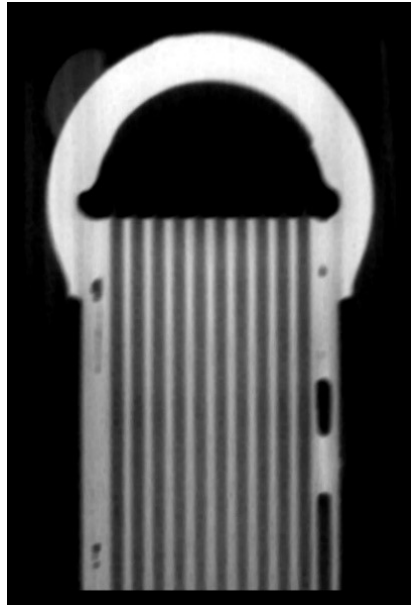
Figure 2.27 Image after processing with
`DeleteLabels` and `CropImg` functions.

For all images, the orientation is further evaluated and checked for incorrect orientation with the top side down. This could be caused by an error during the VGSTUDIO MAX downsizing. The `UpsideDown` function is used for this purpose. This function takes as input the path to the Temp directory from which it reads the individual frames, as well as the index vector of the frames being evaluated. The output of the function is the angle by which the frames are skewed, and an *upsidedown* flag with a value of "TRUE" or "FALSE". This indicates whether the given set of frames was exported from the misoriented CT data.

To determine these output variables, the `UpsideDown` function retrieves individual images Z to the index vector. These images come from the Temp folder, are unmodified and in their original format. First, the labels are removed from the images, and then the median of all pixel values is calculated. This is followed by a filtering process that assigns a value of zero to each pixel with a value less than the median of the pixels in the image. This removes the grey areas around the identified structure. The image after this processing is shown in Figure 2.28.

In the next stage of processing, the contrast of the images is adjusted. For this purpose, the `myContrastAdj` function has been specially designed to allow dynamic contrast adjustment on CT slices according to the specific needs of this evaluation. A detailed description of the working principle of this function will be provided later in the paper The output of this function is a contrast-optimized image ready for further processing.

The images are then binarized using the `imbinarize` function, which is part of the Image Processing Toolbox library in Matlab. This method sets an appropriate threshold at which pixel values above the threshold are converted to 255 (white), while values below the threshold are converted to 0 (black). This process produces a binary image containing only white and black pixels.
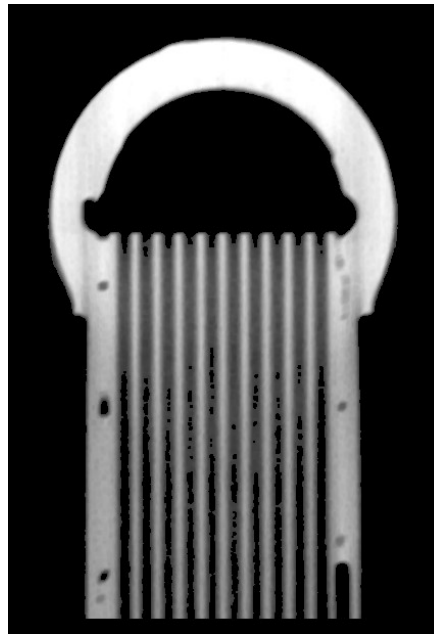
Figure 2.28 Image after processing
by median filter.

Any blank rows and columns of pixels that were created during contrast adjustment and binarization are removed from the image, after which the image is processed by the `rotateImg` function. This function is specifically designed to identify the rotation angle of the image, and rotates the submitted image to a vertical position. It uses a two-dimensional Fourier transform to do this. A detailed description of how this function works will be described later. The output of the function is the angle, the rotated image to the vertical position, and the angle by which the image was rotated.

To identify whether the image is upside down, dilation of the binarized image is performed using the built-in `imdilate` function. An octagon with a radius of 6 pixels is chosen as the structural element. Dilation is a process whereby pixels are "widened" or "stretched" in an image, which typically increases the white areas in binary images. In this instance, the use of a large structural element results in the black areas within the structure being "filled in". The resulting image is shown in Figure 2.29.
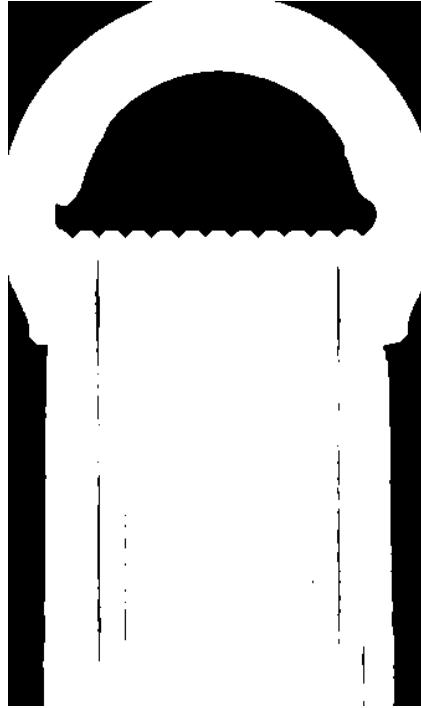
Figure 2.29 Binarized image after dilatation.

If the sum of the pixels on each row is performed on the image thus modified, and if these values are plotted on a graph, the maximum can then be identified on this graph. The graph is shown in Figure 2.30. The maximum on this graph represents the index of the row with the largest amount of white pixels. Given the geometry of the entire structure, the row with the largest number of white pixels corresponds to the point where the channels exit into the manifold. By the position of this row (whether it is at the top or at the bottom of the image) it can be identified whether this image is upside down or not.

Figure 2.30 plot of the sum of pixels on the rows.

This process is performed on all frames to be evaluated according to the vector of frames to be evaluated. In order not to depend on only one frame to evaluate the bad rotation of the whole set, this evaluation is performed with all frames. If upside-down rotation is identified for the majority of frames, it can be assumed that the entire set of frames from one section of the gascooler has upside-down frames and the *upsidedown* flag is set to "TRUE".
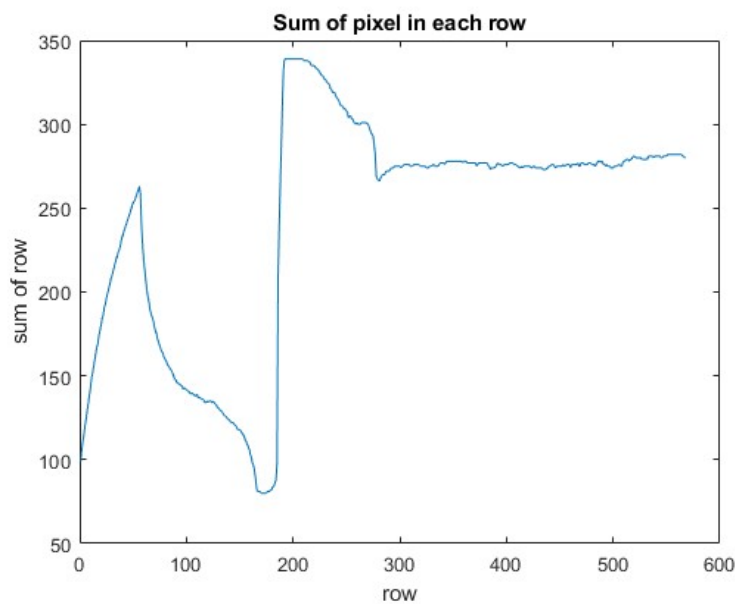
Once the image editing process has been completed in the `PickImgToEval` function, the entire set of images is rotated in accordance with the upside-down flag, which is the output of the same function. At this point, the unmodified images from the Temp folder are once again subjected to processing, rather than the modified images. Subsequently, the contrast of the images is adjusted using the built-in `imadjust` function, which assigns a value of 255 to only the lightest pixels in the image and 0 to the darkest pixels. The other pixel values are recalculated according to how much the lightest pixel has been brightened or the darkest pixel darkened, ensuring that the full range of values of the eight-bit image is utilised.

In the event that the mirroring flag for a given section is set to TRUE, the built-in flip function is employed to mirror the images. Subsequent to these adjustments, the images are stored in the Eval folder with the appropriate indices corresponding to the position on the gascooler.

2.7.4 IMAGE CONTRAST EQUALIZATION

The channels are evaluated from the images stored in the Eval folder. Their evaluation is provided by the evaluate function. This is a more extensive function that uses a larger number of built-in Matlab functions and custom designed functions. The input to this function is the image datastore of the section being processed. The output of this function is a result matrix consisting of ones and zeros. The rows in the matrix represent individual pipes and are arranged according to their actual order. The individual values on the rows of the matrix represent the throughput rating of the individual channels within the respective pipe. A convention for indicating the throughput is established: 1 indicates a clogged channel, 0 indicates a through channel. A schematic of the evaluate function is shown in Figure 2.31.
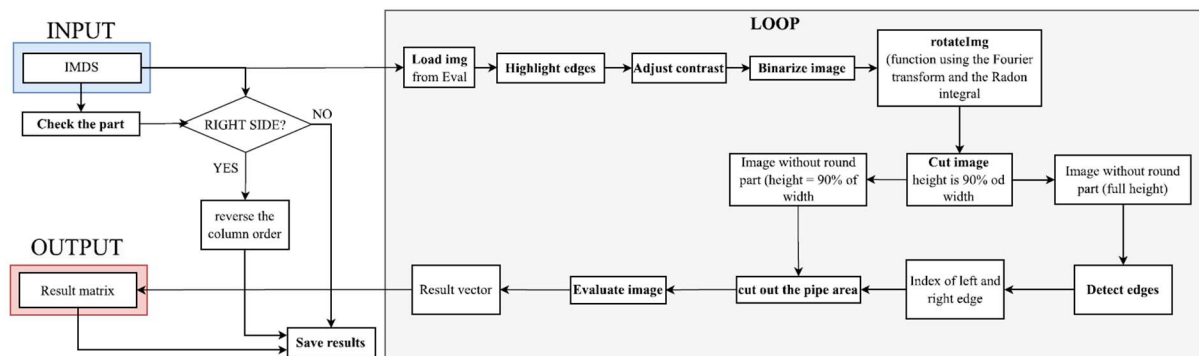

Figure 2.31 Schematic of `evaluate` function.

Similar to the `PickImgToEval` function, the evaluate function first identifies the gascooler section to be evaluated based on the path to the files in the input image datastore. Then, this function creates a new image datastore from the data located in the Eval folder and performs further processing only with images from this directory.

Each image is processed sequentially. The first step is to load the image and highlight the edges of the structure using the `highlightEdges` function, whose input is an image from the Eval directory. This function detects and highlights the right and left edges of the structure in the image. This should ensure that the edges of the pipe are very distinct and will not be drawn during further processing and binarization. A schematic of this process of finding the edges of the structure is illustrated in the attached Figure 2.32.
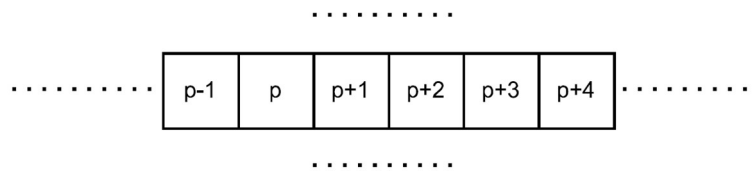
Figure 2.32 Schematic of finding the edge of the structure in the image.

Identifying the left edge of the image is done by searching each row of pixels on the left side of the image. A pixel p whose value is less than 10 is searched, and the next pixel has a value greater than 15 times the value of pixel p. At the same time, the next two pixels in the row have a higher value than the pixel before them.

$$h(p) < 10, \tag{2.1}$$

$$h(p + 1) > 15 \cdot h(p) \tag{2.2}$$

$$h(p + 4) > h(p + 5) \tag{2.3}$$

$$h(p + 6) > h(p + 4) \tag{2.4}$$

where p is an index of pixel on the row and $h(p)$ is the intensity value of the pixel taking natural numbers from the interval $h(p) \in \langle 0,255 \rangle$

If this condition is met, the pixel value $h(p)$ is set to 0 and the intensity of the next five pixels is increased by 50%.

The identification and highlighting of the right edge of the structure in the image is done analogously from the right side of the image. An image with the edges highlighted is shown in Figure 2.33.

Figure 2.33 Image with highlighted edges.

After highlighting the edges of the structure in the image, contrast adjustment is performed using `myContrastAdj`, which dynamically adjusts contrast throughout the image and is effective for different images with different intensities. This function was designed specifically for this application because no other suitable function in Matlab for dynamic contrast adjustment was found applicable to all processed and tested images from different gascoolers.

The `myContrastAdj` function divides the input panel into several parts (windows), for which it sets the local threshold. One window has the size of the image width and height of several pixels. The size of the window can be changed by setting the *widow_height* input parameter of the `myContrastAdj` function. The best results for all evaluated image sets were obtained when the window height was set to one pixel. Thus, one window consists of one row of image pixels.

The local threshold in the window is then equal:

$$LocThrshld_i = \frac{MaxPix_i + MinPix_i}{2} - 0{,}1 \cdot (MaxPix_i - MinPix_i), \qquad (2.5)$$

where $LocThrshld_i$ is the threshold value for a particular window i, $MaxPix_i$ is the highest pixel value in window i a $MinPix_i$ is the lowest pixel value in window i.

In order for the pixel values in a particular window to be adjusted, the following condition must be met:

$$MaxPix_i - MinPix_i > 30 \qquad (2.6)$$

If the condition is satisfied, the value of window i pixels higher than $LocThrshld_i$ is increased by x, the value of pixels lower than $LocThrshld_i$ is decreased by x, where x is estimated as:

$$x = \frac{7000}{MaxPix_i} \qquad (2.7)$$

After editing the pixel values in a given window, the new pixel values are stored in the *newImage* variable, and the process continues by evaluating the next window of the input image.

This process of contrast adjustment is essential, especially since the bright areas in the upper region of the image typically exhibit significantly different intensities compared to the bright areas in the lower part of the image. In some images, the dark pixels at the top of the image may have similar intensity to the light pixels at the bottom. While the human eye has the ability to adaptively assess intensity depending on the surrounding context, digital image processing faces a challenge as it is not possible to simply set a universal threshold for the entire image.

The `myContrastAdj` function adjusts individual pixel values according to conditions in specific areas of the image. This ensures that each part of the image is processed with respect to its specific lighting conditions. With this method, details in differently lit areas can be effectively highlighted to improve the overall image quality for subsequent analysis. An example of a processed image is shown in Figure 2.34. A different image was chosen that better represents the problem and can better show the functionality of the developed process.
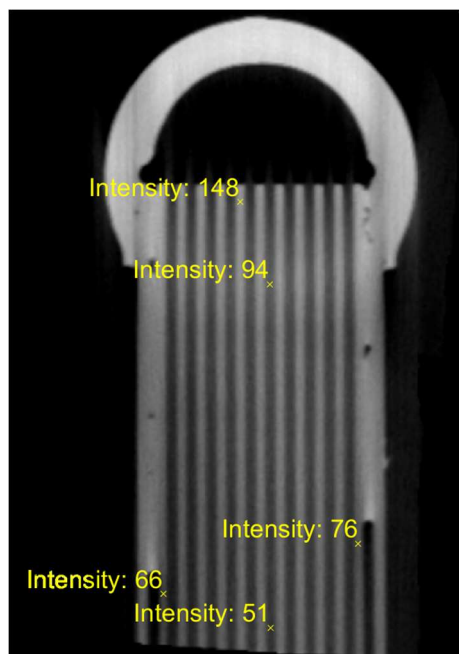

Figure 2.34 Intensity values in
different parts of the image.

After adjusting the pixel intensity of the image, the image is stored in the variable *newImage* and its contrast is further adjusted using the built-in `adapthisteq` function, which can increase the contrast locally based on histogram equalization in individual areas of the image.

The sizes of each region are set to 64 pixels. Although this value is significantly higher than commonly used values, it has been shown to produce optimal results for these images.

The resulting image is then sharpened using the built-in `imsharpen` function. The step-by-step adjustment of each image is shown in Figure 2.35.
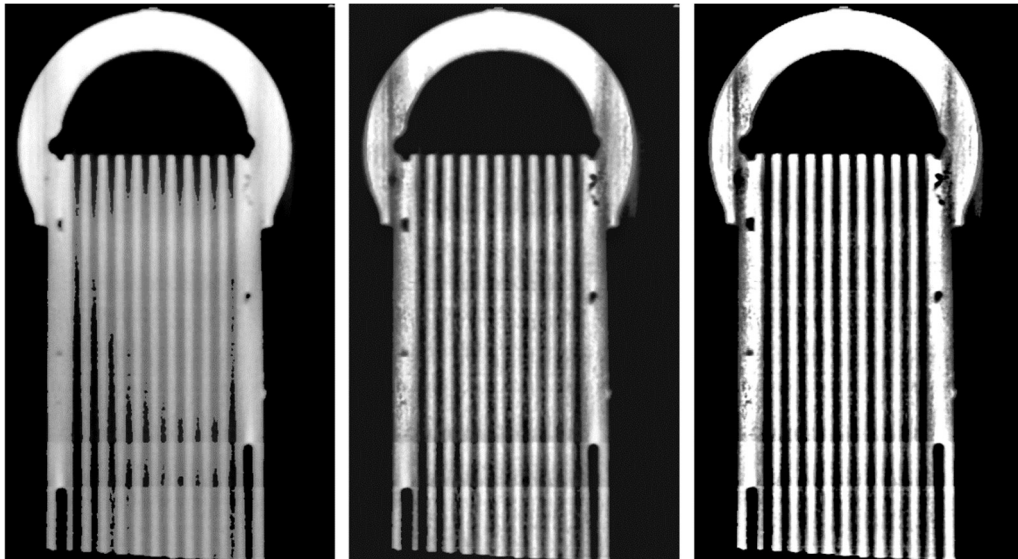
Figure 2.35 Gradual image adjustment in the `myConstrastAdj` function.

This modified image is the output of the `myContrastAdj` function, which is passed back to the evaluate function. The image is then binarized using the `imbinarize` function, which is part of Matlab. Before the final evaluation, the images are checked once more for spins.

2.7.5 IMAGE ROTATION CHECK

The `rotateImg` function is used to control the rotation of the image. This function was already used before exporting images to the Eval folder and to determine the rotation angle of images in the `UpsideDown` function. To demonstrate the image rotation correction, an image that suffers from this defect was selected and can be seen in Figure 2.36.
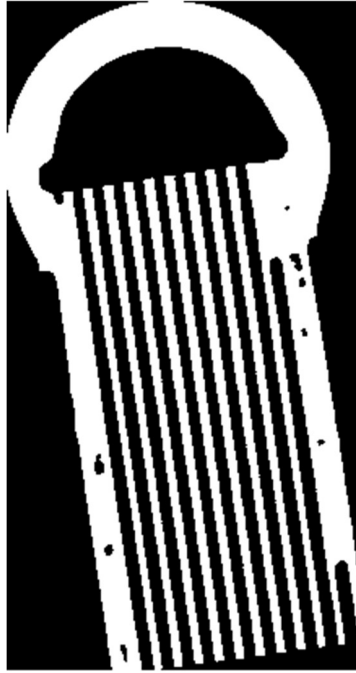
Figure 2.36 Input image of
`rotateImg` function.

The input of this function is the image that is analysed, and the output of the function is the image rotated to the correct position, while the angle by which the image was rotated is also determined. The Fourier transform of the image is used to determine the cardinal directions and rotation of the image and then integrated in segments starting from the centre of the amplitude spectrum of the image.

Before applying the two-dimensional Fourier transform, a Hanning filter is applied to the image. This step ensures the removal of high frequency components and noise at the edges of the image. First, the coordinates of the image centre must be determined and then the distance from the image centre to the nearest edge must be determined. This distance is denoted as R. Subsequently, r is set as 80% of R, which represents the radius of the image within which the image remains unchanged. For each pixel of the image, the square of its distance from the centre of the image is then computed, allowing to determine whether the pixel belongs to the defined circle or lies outside it.

Pixels lying outside the circle of radius R are set to 0. Pixels inside a circle of radius r remain unchanged. A cosine-based weighting function is applied to pixels lying between the small circle r and the large circle R, which gradually decreases the pixel values towards the outer circle R [47]:

$$p_{ij} = p_{ij} \cdot 0.5 + 0.5 * \cos\left(\pi \cdot \frac{\sqrt{\rho_2} - r}{R - r} \right) \tag{2.8}$$

The value of the cosine is adjusted to vary gradually from 1 for radius r to 0.5 for radius R. This cosine curve provides a smooth transition and effectively suppresses artifacts at the edges of the filtered region. The image after applying the Hanning filter is shown in Figure 2.37.

Figure 2.37 Image after filtering
with a Hanning filter.

A two-dimensional Fourier transform is then applied to this image using the built-in fft2 function in Matlab. This process converts the image from the spatial domain, where pixel values are represented by their location and intensity, to the frequency domain, where pixel values are represented by frequency and phase. To facilitate spectrum interpretation, the `fftshift` function is used to shift the zero frequencies to the centre of the spectrum. This places low frequencies in the centre of the image and high frequencies at the edges.

The following is the calculation of the amplitude spectrum, which is defined as the magnitude (absolute value) of the complex numbers obtained by Fourier transformation. The result of this step is an amplitude spectrum that illustrates the intensity of the individual frequencies in the image. A snapshot of the magnitude spectrum of the image under investigation in logarithmic coordinates is shown in Figure 2.38.

The amplitude spectrum is then cropped into a circular region with a radius corresponding to half of the shorter side of the image. The pixel values outside this region are set to zero. In this way, the high frequency components are removed from the spectrum, allowing more focus on the main frequency components.
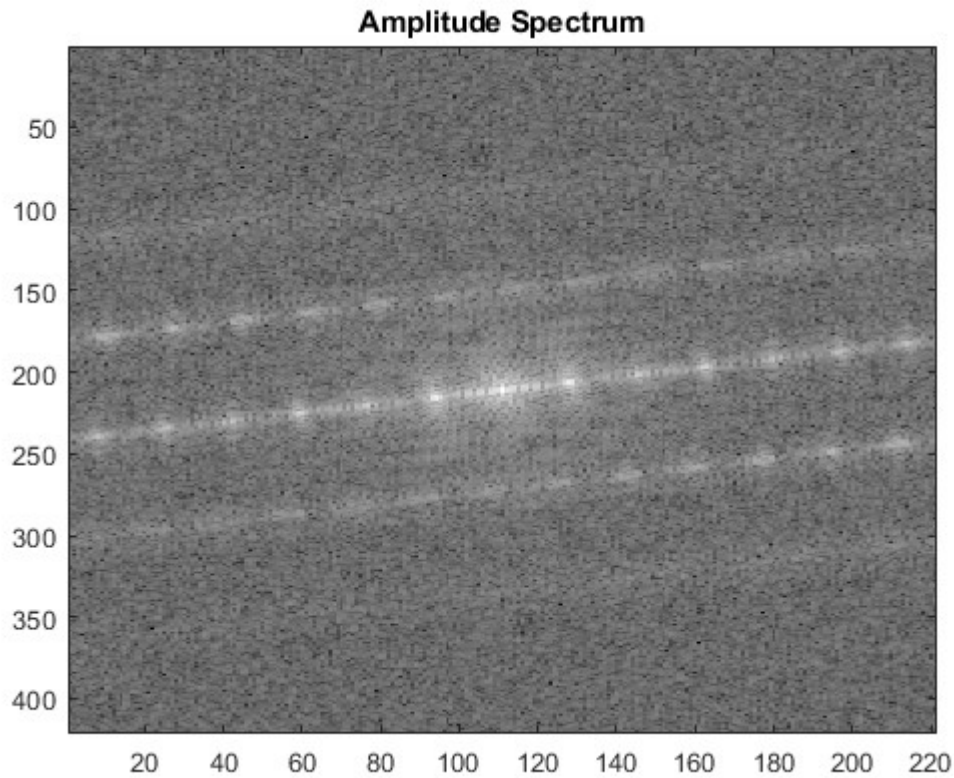
Figure 2.38 Amplitude spectrum of the image.

The Radon transform in the amplitude spectrum is used to determine the main directions in the image. This method converts the image from the spatial domain into a parametric space of angles and distances and analyses the distribution of frequency components in different directions. The dominant orientation is identified in the direction where the integral values reach a maximum, indicating the main direction of features in the image. The identification of this dominant orientation allows to calculate the angle by which the image has been rotated. Subsequently, a rotation correction is made for this angle in the opposite direction, which returns the image to the correct orientation.

In Matlab, the diagonal length of the image was first determined, which represents the length of all integration lines, ensuring that the line is long enough to cover the entire image regardless of its orientation. The integration along this line takes place at discrete points, with each line divided into j discrete points for which the value of the amplitude spectrum is determined. The integration lines pass through the centre of the image and vary in angle. A total of 180 lines are integrated along the image with an angular difference of 1° between each line. Before the integration, the coordinates of the points x and y on the line are determined, in which the value of the amplitude spectrum is subsequently determined:

$$x_i = s_x + d \cdot \cos\left(\frac{\theta_i}{180} \cdot \pi\right) \tag{2.9}$$

$$y_i = s_y + d \cdot \cos\left(\frac{\theta_i}{180} \cdot \pi\right) \tag{2.10}$$

where x_i and y_i are vectors of coordinates of points along the line at which the value of the amplitude spectrum for integration will be detected, s_x and s_y are the coordinates of the image centre, d is a vector of distances from the image centre at which integration will be performed, θ_i is the angle of the corresponding integration line in degrees and i is an index taking natural numbers from the interval $\langle 0,180 \rangle$.

For each pair of $[x, y]$ coordinates, the coordinates of the four nearest pixels are calculated from the x and y vectors and a bilinear transformation is performed between them to determine the value of the amplitude spectrum at $[x, y]$. If the point $[x, y]$ lies outside a circle of radius half the length of the shorter side of the original image, the value of the amplitude spectrum is zero.

To perform the bilinear transformation, the weights Δx and Δy are first determined as:

$$\Delta x = x - x_{down} \tag{2.11}$$

$$\Delta y = y - y_{down} \tag{2.12}$$

where x_{down} and y_{down} are the nearest lower coordinates of the pixel that lies around the point $[x, y]$.

The coefficients b_1 to b_4 for the bilinear transformation are determined from the functional values of the amplitude spectrum in the nearest four pixels:

$$b_1 = f(x_{down}, y_{down}) \tag{2.13}$$

$$b_2 = f(x_{up}, y_{down}) - f(x_{down}, y_{down}) \tag{2.14}$$

$$b_3 = f(x_{down}, y_{up}) - f(x_{down}, y_{down}) \tag{2.15}$$

$$b_4 = f(x_{up}, y_{up}) - f(x_{up}, y_{down}) - f(x_{down}, y_{up}) + f(x_{down}, y_{down}) \tag{2.16}$$

where x_{up} and y_{up} are the nearest higher coordinates of the pixel that lies around the point $[x, y]$.

The bilinear transformation is then calculated:

$$f(j) = b_1 + b_2 \cdot \Delta x + b_3 \cdot \Delta y + b_4 \cdot \Delta x \Delta y \tag{2.17}$$

where $f(j)$ is the interpolated value of the amplitude spectrum at the corresponding discrete point on the $[x, y]$ line along which the integration is performed.

The resulting value of integration along one integration line is given by the sum of the interpolated values of the amplitude spectrum at all discrete points along this line:

$$I_i = \sum_{j=1}^{N} f(j) \tag{2.18}$$

where $f(j)$ is the interpolated value of the amplitude spectrum for a particular point on the integration line and j takes natural numbers from 1 to the total number of discrete points on the integration line. The values of the individual integrals for different angles of the integration line are shown in Figure 2.39.
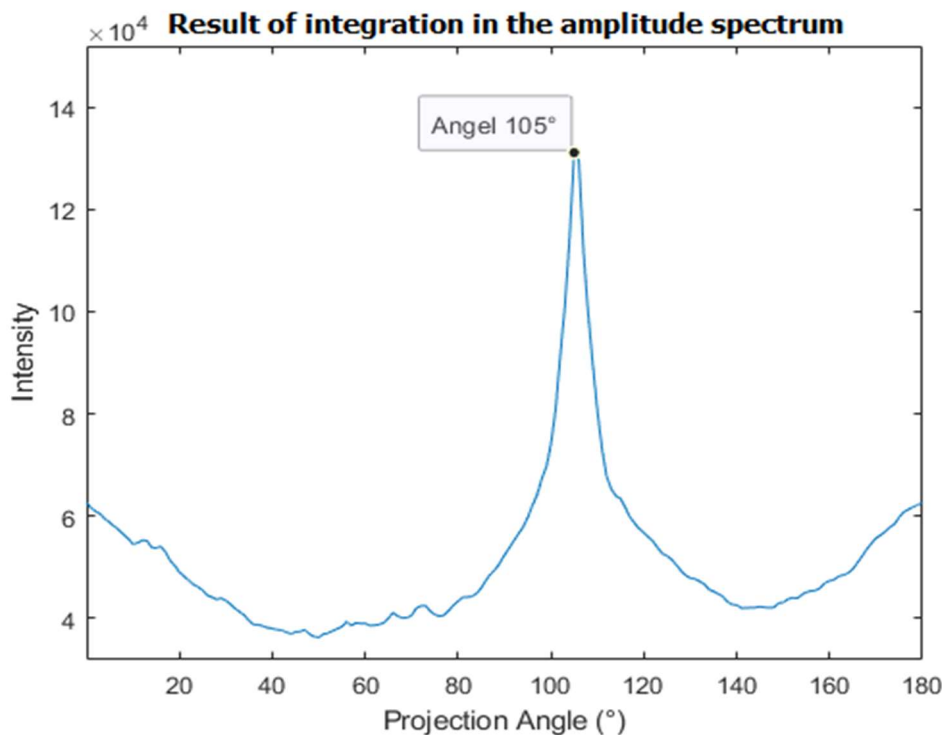
Figure 2.39 The result of integration in the amplitude spectrum.

Subsequently, local maxima around 90° and 180° are determined from this waveform. These maxima indicate the angle of the principal directions in the image. Due to the regular structure of the images, it can be argued that maxima should be found at 90° and 180°. If the maxima deviate from these values, the image is considered rotated. The correction angle φ for such an image is calculated as:

$$\varphi = \frac{(\varphi_{1\,max} - 90\,°) + (\varphi_{2\,max} - 180\,°)}{2} \tag{2.19}$$

where $\varphi_{1\,max}$ is the maximum found around 90° and $\varphi_{2\,max}$ is the maximum found around 180°.

The image at the input of the `rotateImg` function is then corrected by the angle $(-\varphi)$. The output of this function is the corrected image shown in Figure 2.40 and the corrected angle.
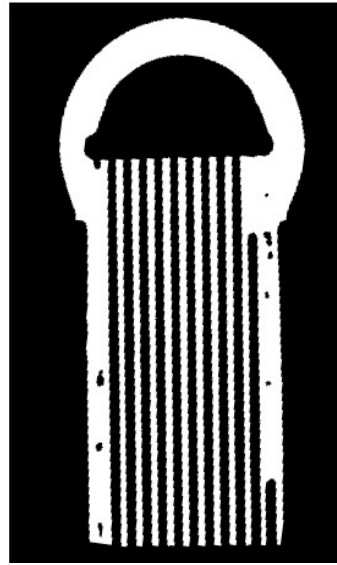
Figure 2.40 Corrected image.

2.7.6 FINAL EVALUATION

An image on which the contrast has been aligned so that it can be correctly binarized and which has been rotated to the vertical position enters the `CutImg` function, which crops the image at the entry point of the channels into the manifold. The clipping location is identified in a similar manner to that previously used in the `UpsideDown` function to determine the image `flip`.

The input to the `CutImg` function is a binarized image to which the `imdilate` function is applied with a 6 pixel radius octagonal structure kernel. The resulting image after dilation is shown in Figure 2.41.
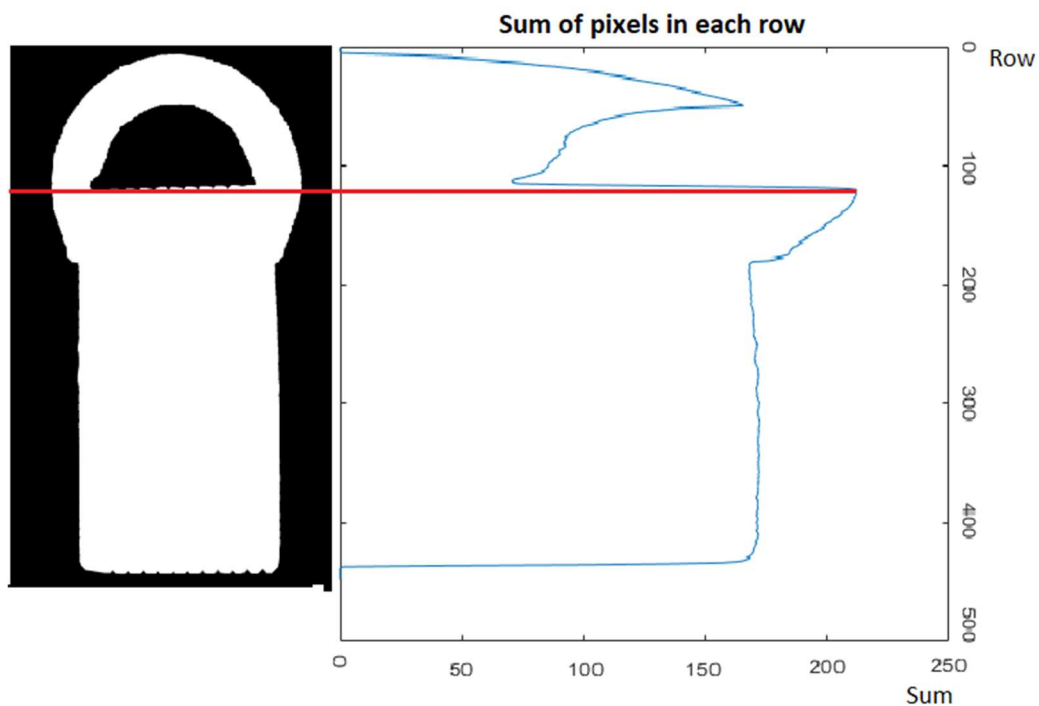
Figure 2.41 Image after dilatation.

In this image, the sum of the pixels in each row is performed, then the row with the highest sum is determined and used as a reference. The image is cropped horizontally at a point ten pixels above the reference row, leaving the bottom of the image. The reason for shifting the cut is to be more certain that the edge of the channels will not be removed from the image, which could lead to a bias in the evaluation result. Should the height of the resulting image exceed 90 % of the image width, the height of the image is also reduced from the bottom to a maximum image height equal to 90 % of the image width. This size appears to be sufficient for the final evaluation. The reason for this step is the poor quality at the bottom of the image for some datasets. The cropped image is shown in Figure 2.42.

Figure 2.42 Cropped image.

In the next step, the left and right edges of the tube with channels are identified. The identification is performed by the function detectEdges, whose input is an image that does not contain the round top of the manifold, but whose height has not been reduced to 90% of the image width. This is to increase the accuracy of identifying the edges of the structure in the image.

Each row of pixels in the input image is searched with a for loop from its edge towards the centre of the image. The algorithm works with an already binarized 8-bit image, so the value of each pixel is either 0 or 255. If the loop finds a pixel with a value of 255, it checks the next 4 pixels on the same line. If all these pixels have a value of 255, the loop stores the order of the first pixel in the appropriate variable and continues on the next line.

When searching for the left edge, the rows are traversed from the left edge and the indexes found are stored in the *firstIdx* variable; analogously, when determining the right edge of the structure, the rows of pixels are traversed from the right edge of the frame and the indexes stored in the *lastIdx* variable.

The left edge of the structure is then determined as the median of the values in the corresponding variables. These values are the output of the detectEdges function. A cropped image according to the edge indices determined in this way is shown in Figure 2.43.
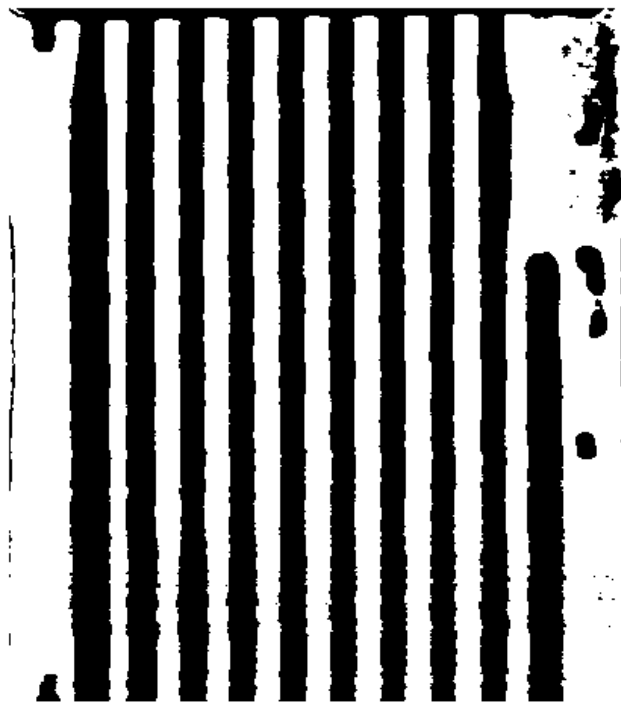
Figure 2.43 Image of tube (both edges cut off)

The actual evaluation of channel patency starts by first adjusting the image to a width of 500 pixels and then entering the `evalTube` function, which creates a vector of twelve values (1 or 0) from the image, depending on whether the individual channels in the image are passable (value 0) or clogged (value 1).

The evaluation itself in this function is based on the assumption that the structure of each tube is regular and the same on all pieces. This assumption is based on a manufacturing technology where individual tubes with channels are produced by extrusion so that all channels in the tube are of the same width and their axial distances are the same.

Based on the width of the image, the axial coordinates of the individual channels are calculated as seen in Figure 2.44. Next, the width of one channel in pixels is determined; if the image width is 500 pixels, one channel has a width of 20 pixels. These values are stored in the appropriate variables. The evaluation itself consists of summing the columns of pixels in the image in the channel area. This is defined by its axis and the width of the channel in pixels. The pixel columns in the vicinity of the axis corresponding to the channel width are summed. Since the algorithm works with a binarized image, the values of each pixel are either 0 or 255. If the sum of pixels in at least one column around the channel is zero, the channel is considered to be through and the process continues by analysing the next channel in the same way.

Once this evaluation is complete, a vector of logical values is constructed, where 0 represents a through channel and 1 represents a clogged channel. The order of the values in the vector corresponds to the order of the channels in the image. This vector is the output of the `evalTube` function and is passed back to the `evaluate` function.
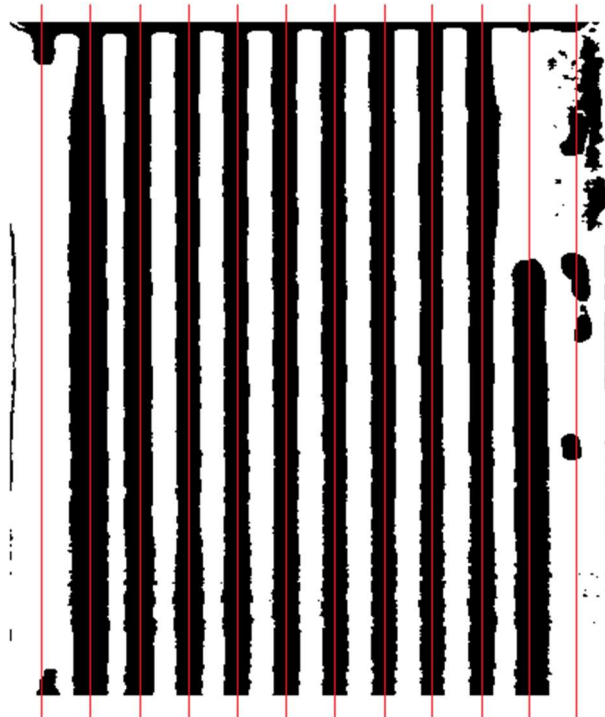
Figure 2.44 Scheme of evaluation of images - the axes of the channels are marked.

The individual logical vectors are used to construct the result matrix, which is then stored in the result_<part>.txt file in the Sample_xx directory. Where <part> is replaced by the label of the section being evaluated.

2.7.7 PREREQUISITES FOR THE CORRECT FUNCTIONING OF THE ALGORITHM

For a successful and reliable evaluation of the entire image set, some assumptions on the quality of the images that enter into this evaluation need to be met. Poor image quality in any of these respects can lead to unreliable results.

The quality of the evaluation depends mainly on good contrast and resolution of the images. Good image resolution is ensured by appropriate settings of the scanner, the energy used and the distance between the X-ray source and the shield. In addition, the export of images with a black background is also necessary.

Undesirable from the point of view of image quality are poor contrast, too dark shades, blending of the channels with their baffles, or blending of the edges of the tube with the background. In such images, it is very likely that poor binarization of the image will occur and the evaluation will not be valid. Images that have too thin channel walls are also unsuitable. This defect is illustrated in Figure 2.45. A is usually caused by inappropriate filtering of the CT data in VGSTUDIO MAX before exporting the slices. In these images, there is a risk that thin walls will not be detected at all.
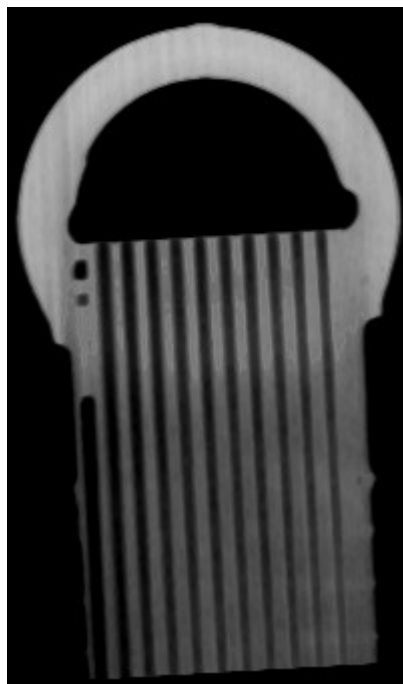
Figure 2.45 Low-contrast image,
hard-to-detect left edge.

The second very important prerequisite is the correct orientation of the image (with the exception of a slight misalignment, e.g. up to 10°). Despite the fact that the algorithm implements functions and procedures that should correct the rotation of the image by up to 40°, or detect if the image is vertically flipped, there may be a situation where one of the image rotation mechanisms malfunctions and the image is rotated so that the individual channels are not pointing vertically downwards, but horizontally. This error typically occurs when the images are offset by 45° to 135°. In this case, the evaluation for all channels will be completely wrong. The user can check the correct orientation of the images in the Eval folder. For small angles of incorrect image rotation, the implemented algorithms work very reliably.

For correct detection of the edges of the pipe in the image, it is very important that the surroundings of the part being scanned are not contaminated by artifacts from the scan. This type of image is shown in Figure 2.46. An anomaly of this type is corrected for by storing the pixel index when searching for the left and right edges of the pipe before the final evaluation, only after the next four pixels are white. The median of the vector of indices stored in this way is then taken as the pipe edge. However, if there were a larger artifact in the image that was parallel to the edge of the image, it could be mistaken for a pipe edge. This error would result in cropping of the image at an undesirable location, misidentification of the position of the axes of the individual channels, and investigation of a region that is not surrounding the axis of the channels. The result matrix would therefore be unreliable.
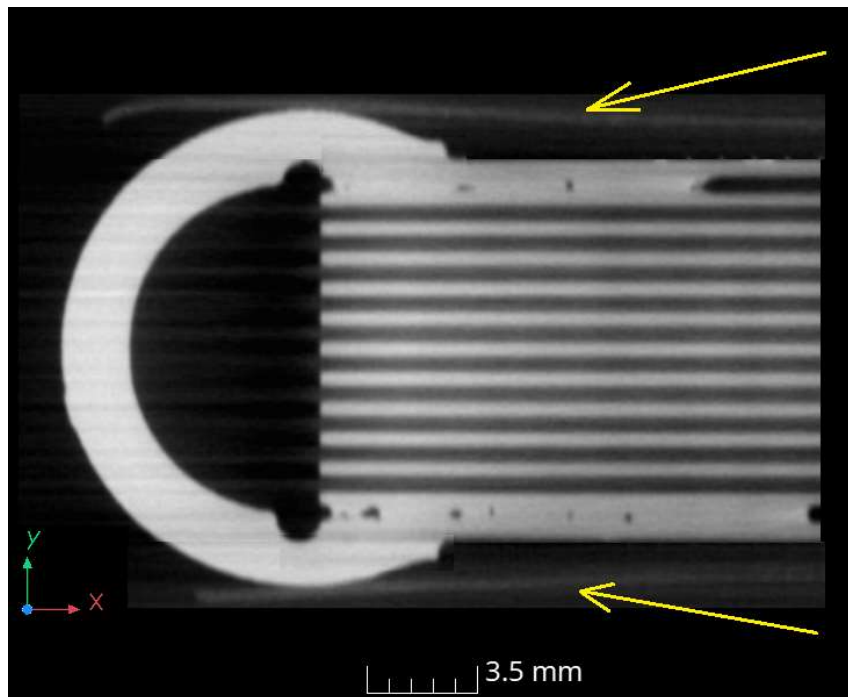
Figure 2.46 Artifacts around the slice.

Last but not least, the correct function of the evaluation script is also ensured by the accurate alignment of the CAD model and CT reconstruction. In the case of inaccurate alignment in VGSTUDIO MAX, the CT reconstruction is inaccurately positioned in space and exports images from planes that are outside the channel planes, see Figure 2.47. In this case, the images will not show the desired section in the plane of the channels, thus the images will not contain information about how the channels look in section and correct evaluation will be impossible. Possible artefacts in the CT data may also cause complications when establishing the 3D reconstruction in space.
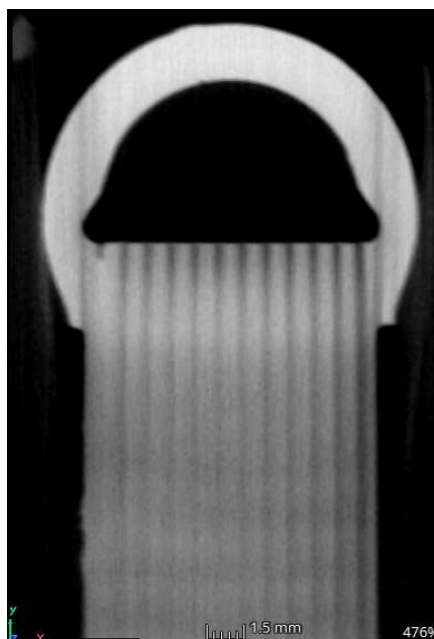
Figure 2.47 An image that was created
out of the plane of the channels.

In order for the automatic spatial arrangement of the CT reconstruction functions of Best Fit to work properly, a manual cropping of the CT data and the area to be evaluated is required after reconstruction. Due to the tilt, the reconstructions are wedge-shaped and too long tube sections are scanned at the bottom of the reconstruction. This causes difficulties when using the Best Fit function, as the tubes are deformed at a greater distance from the manifold and their shape does not match the ideal .step model. The Best Fit function incorrectly determines planes and slices are exported from inappropriate areas. This is illustrated in Figure 2.48.
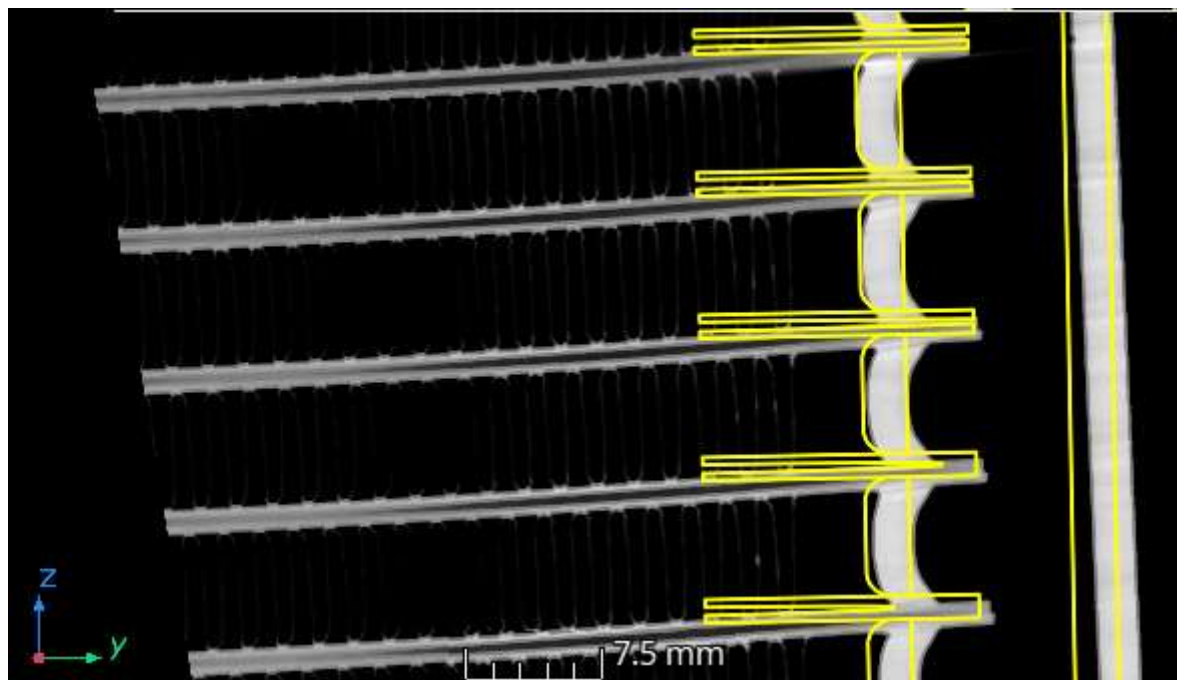
Figure 2.48 Incorrect alignment of sample 176 R1_R2 due to untrimmed data.

2.7.8 USER INTERFACE OF APPLICATION

For easy use of scripts for automatic evaluation of clogged channels from CT data slices in XY planes, an application in .exe format has been created, which is executable on standard PCs with the Windows operating system and installed Matlab Runtime. The application was developed using the App Designer tool in Matlab and features a simple user interface, a preview of which is displayed in Figure 2.49.

At the start, the user can either manually enter the path to the folder with slices from the CT reconstruction or use the "Browse" button to open a menu where they can search for and select the appropriate folder. The user then has the option to evaluate the entire gascooler with all its four sections or to focus on individual sections. By pressing the "Process and evaluate all parts" or "Process and evaluate selected part" button, the described algorithm for evaluation is initiated.

The evaluation process is visually represented by a progress bar. During the process, a dialog box appears asking the user if the image with the "Side Support" part has been correctly identified. The dialog box is shown in Figure 2.23. The user can confirm the correct identification by pressing the "Yes" button, or if the image was not correctly identified, pressing the "No" button will prompt another window where the user is asked to select the correct image.
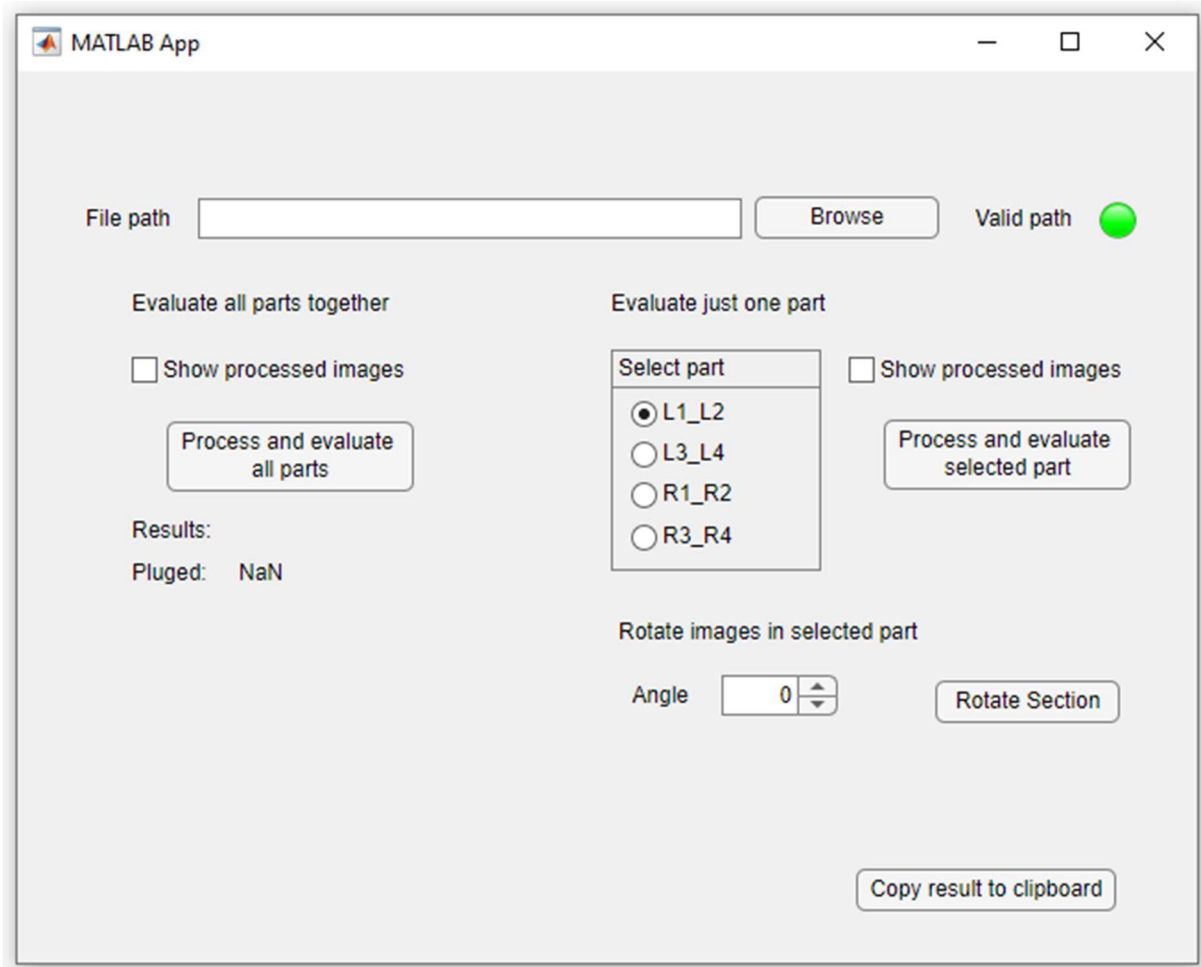
Figure 2.49 A preview of the user interface of the application.

After identifying the image, the evaluation proceeds as described. The results are saved in the directory "Sample_<sample number>" in the form of text documents named "result_<part>.txt". These results can be easily copied to the clipboard using the "Copy result to clipboard" button and then pasted, for example, into a pre-prepared table in Microsoft Excel, which calculates the percentage of clogging of the gascooler. This table, used by Hanon for evaluation, automatically calculates the percentage of clogging of the gascooler. The results are transferred by selecting the first cell in the table and pressing the CTRL+V keyboard combination. The table is shown in Figure 2.50

Information about the percentage of clogging of the gascooler is also displayed in the application along with an indication of successful completion of the evaluation. The information is displayed on the appropriate line below the "Process and evaluate all parts" button.

Figure 2.50 Excel table used for evaluation.

		Bottom side									Top side			Top side										Bottom side			
	Header 1	1	2	3	4	5	6	7	8	9	10	11	12	12	11	10	9	8	7	6	5	4	3	2	1	Header 2	No of plugged holes
V	1	1												1	1										1	1	3
V	2	1												1	1									1		2	4
V	3																								1	3	1
V	4	1												1												4	2
V	5	1										1		1											1	5	2
V	6	1												1											1	6	1
V	7	1													1										1	7	2
V	8	1												1											1	8	1
V	9	1												1	1											9	3
V	10	1												1											1	10	2
V	11	1	1											1											1	11	3
V	12												1	1											1	12	2
V	13	1												1											1	13	2
V	14		1										1	1	1										1	14	4
V	15	1	1											1											1	15	3
V	16	1																							1	16	1
V	17	1																							1	17	1
V	18	1												1											1	18	2
flat	19	1									1	1													1	19	3
V	20	1	1											1											1	20	3
V	21	1												1		1									1	21	3
V	22	1												1	1										1	22	2
V	23	1												1											1	23	2
V	24	1											1	1									1	1	1	24	3

Information about the percentage of gascooler clogging is also displayed in the application together with an indication of successful completion of the evaluation. The information is displayed on the appropriate line under the *"Process and evaluate all parts"* button.

Before starting the evaluation, the user has the option to activate the "Show processed images" feature. This function ensures that the temporary "Eval" folder is not deleted after the evaluation is completed. This folder contains pre-processed and sorted images intended for subsequent evaluation. Keeping these images provides the user with better control over the quality of data entering the evaluation. It allows for the detection of potential issues such as incorrectly oriented images, missing, or damaged images that are not suitable for evaluation.

Additionally, it allows the user to perform a quick check of the result matrix based on these images. The order of the images in the "Eval" temporary folder corresponds to the order of images in the folder with the original data, which facilitates the identification of potential errors in the evaluation. The "Eval" folder is located in the folder corresponding to the evaluated section of the gascooler.

Another feature of this application is the ability to perform a batch rotation of images. If images are exported that are rotated by a large angle (approximately more than 10 degrees), the user can rotate the images in the given section by the selected angle. This better eliminates the error of incorrect evaluation of images due to their unsuitable orientation.

2.8 TESTING AND RESULTS OF THE PROPOSED ALGORITHM

During the design of this algorithm and its parameters, work was carried out with a total of eight different datasets of scanned gas coolers. Table 2.1 presents the success rate of the algorithm in evaluating the clogging of channels. The calculated percentages were determined by comparing the result matrix created by the algorithm with the result matrix evaluated by a human. If all positions of ones and zeros in both matrices were identical, the success rate of the algorithm is determined as 100%. If some positions in the result matrices differ, the success rate is given by the ratio of matching positions to the total number of positions in the matrix.

Table 2.1 Evaluation result of eight samples of gascoolers

Marking	Evaluation success [%]
Sample_161	99,08
Sample_163	98,27
Sample_165	95.43
Sample_166	94,16
Sample_172	97,63
Sample_175	98,79
Sample_176	80,33
Sample_179	99,37

The average success rate of correctly identifying the clogging of channels by the entire algorithm is 95.38%. This success rate is influenced by the entire evaluation process, including the correct alignment of CT data and CAD model in VGSTUDIOMAX before exporting the images. It is evident that this part has the most significant impact on the overall success of the evaluation. If poor images are exported, reliable data cannot be assessed from them.

The overall average success rate is significantly reduced by the evaluation of the gas cooler with number 176. The success rate of evaluating individual sections in this sample is in Table 2.2:

Table 2.2 Results of evaluation of individual sections in sample 176

Sample 176	L1_L2	L3_L4	R1_R2	R3_R4
Evaluation success [%]	89,12	97,69	48,38	86,11

The highest proportion of incorrect results is attributed to the R1_R2 section, whose incorrect assembly is shown in Figure 2.48. Due to this improper assembly, images were exported that do not clearly indicate whether the channels are clogged or not. These incorrect images are shown in Figure 2.51.
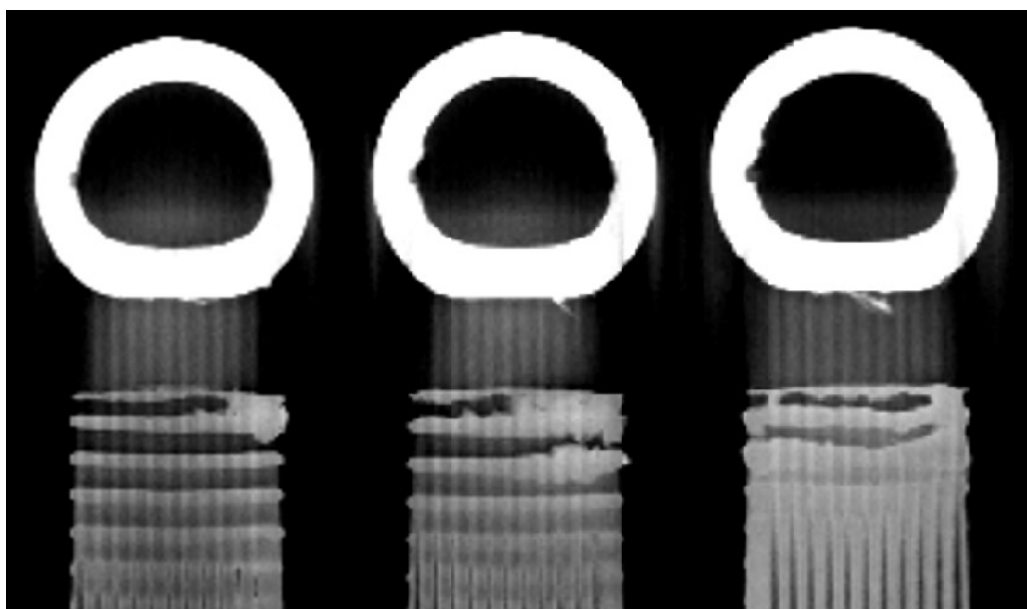

Figure 2.51 Unevaluable images from sample 176 section R1_R2.

Based on this error, various experiments were conducted with the settings of the *BestFit* function, erosion, dilation, and other filters including different methods for determining the surface of CT data. All these attempts resulted in very similar outcomes, which are most likely due to the size of the dataset of the scanned sample 176. The CT data are not reduced to just the area where the channels open into the manifold, but the channels are left in their entire scanned length. A different geometry of the CAD model and CT data probably causes a misalignment, which leads to the export of inappropriate sections.

The same macro and the same settings of the entire evaluation algorithm were subsequently applied to the CT data of two gas coolers that had not yet been evaluated and were kept for testing purposes. These are completely randomly selected CT scans. The success rates of evaluating these pieces are in Table 2.3.

Table 2.3 Results of evaluation of test samples

Marking	Evaluation success [%]
Sample_160	98,50
Sample_164	97,86

In evaluating the test data on two samples of gas coolers, a very similar success rate in assessing clogged channels was achieved as with the previous eight datasets. The average success rate for evaluating the test data is 98.18%. This average is 2.8% better than the training datasets.

Repeated testing confirmed that the image processing algorithm in Matlab works reliably if the input images meet the conditions for proper algorithm function as described in section 2.7.7. Therefore, further efforts were made to design a more efficient automatic image export from VGSTUDIOMAX, which would ensure high-quality slice images in the required planes of CT data.

For fully automatic spatial alignment in VGSTUDIOMAX, it is necessary to use the *BestFit* function, therefore the macro was modified by changing filters, but the function itself remains the same after alignment. Among the modifications, the most successful macros are shown in Figure 2.52.

With these macros and the same script in Matlab, the following results were achieved on eight test datasets, as recorded in the Table 2.4:
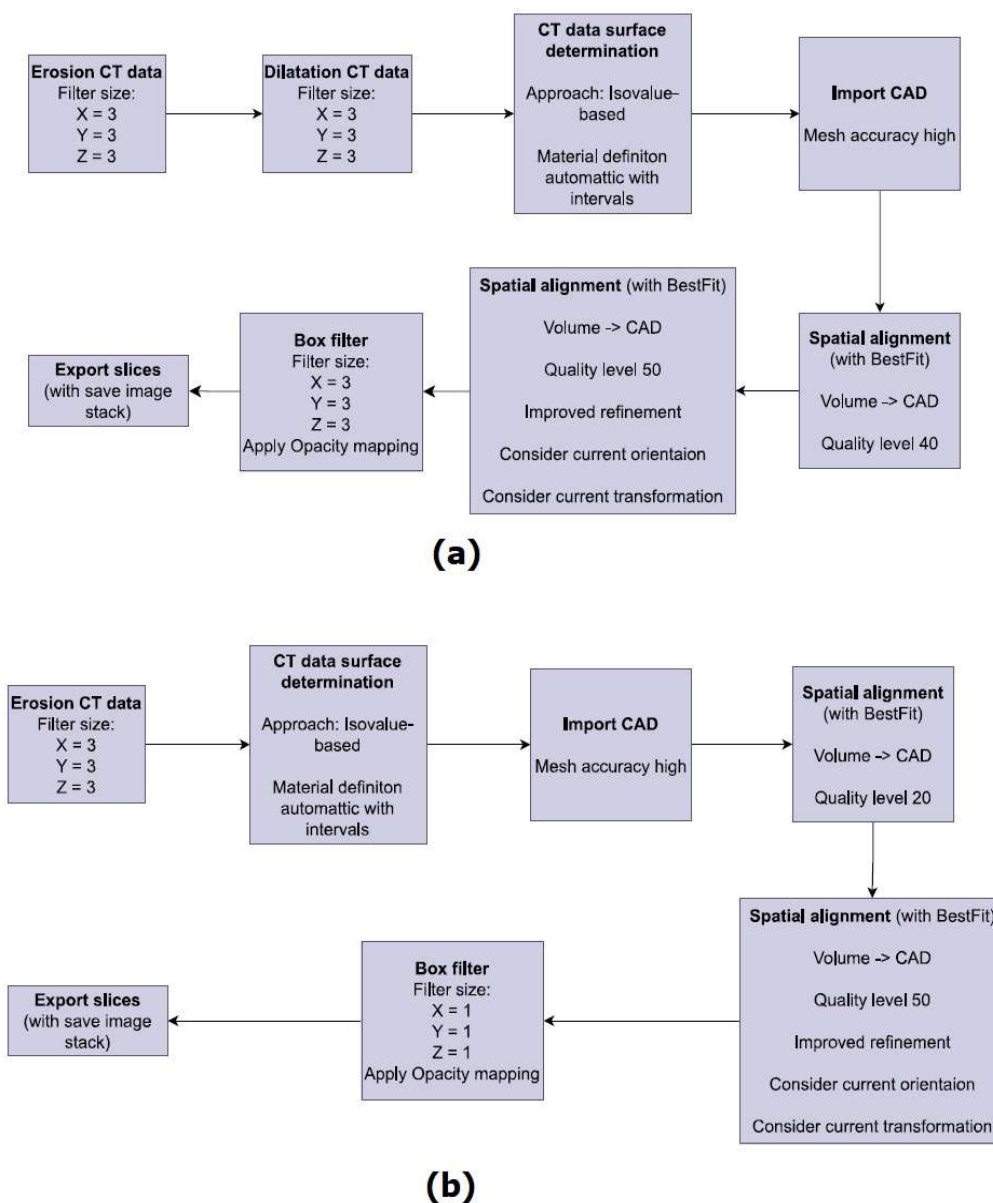

Figure 2.52 Schematic of modified macros: (a) Modification I, (b) modification II.

Table 2.4 Evaluation result with modified macros

| Marking | Evaluation success [%] | |
	Modification I	Modification II
Sample_161	97,86	98,61
Sample_163	98,84	98,90
Sample_165	99,01	98,74
Sample_166	99,59	99,89
Sample_172	95,02	98,09
Sample_175	97,57	99,08
Sample_176	79,57	84,66
Sample_179	97,68	99,48

When applying modified macros to the test datasets and using the same Matlab script to evaluate the exported images, the success rate achieved is recorded in the Table 2.5:

Table 2.5 Evaluation results of test CT data with modified macros

| Marking | Evaluation success [%] | |
	Modified macro I	Modified macro II
Sample_160	77,19	81,42
Sample_164	92,53	94,21

Using the first modification, the average success rate in evaluating channel clogging increased to 95.64% across eight trial datasets. However, for the test datasets, the success rate decreased by 13.32% to just 84.86%.

The second modification of the macro brought an even more significant improvement in the success rate of evaluating channel clogging for the eight trial scans, averaging 97.83%. However, the test data were evaluated with a success rate of 87.82%.

From these results, it can be concluded that the accuracy of the entire algorithm is highly dependent on the proper export of images from VGSTUDIOMAX. Using standard functions of this software did not further improve the results of image exporting. Therefore, it would be possible to further work on improving image export from VGSTUDIOMAX by programming advanced mathematical functions for more precise interpolation of evaluated slices and their export.

2.9 IMAGE QUALITY ESTIMATION BY NEURAL NETWORK

Significant influence of image quality on the results of the evaluation in the application created in Matlab introduces a significant element of uncertainty into the entire process. It was deemed appropriate to design an image quality evaluation system that would identify images unsuitable for this type of evaluation and exclude them from the evaluation. This would increase the reliability of the output data. Areas with poor-quality images would be marked and recommended for manual review by the user.

Evaluating images based on the amount of noise, sharpness, and contrast did not yield reliable results, because even a technically high-quality sharp image without noise and with sufficient contrast may not be exported from a suitable location in the CT reconstruction. Such an image shows good qualitative values but does not contain the necessary information as seen in Figure 2.51.

One possible way to evaluate image quality based on content is to create a deep convolutional neural network that would be trained on specific CT data images, which would be sorted into two or more classes, based on the number of poorly evaluated ports.

For this purpose, a set of images exported using different macros from the examined CT data of gas coolers was created. These images were subsequently evaluated by an algorithm in MATLAB and the result compared with the result obtained by manual evaluation. Given the amount of data required for classification tasks, the images were divided into only two groups. The first group of images were high-quality images that were evaluated without error. The second category of images were slices that encountered 2 or more errors in evaluating the patency of the channels. An error here means the incorrect evaluation of a single channel.

In this manner, 31 475 images were sorted, forming the training and validation dataset for the neural network. The images were slightly augmented, mainly by shifting. Another 3 119 images from completely different CT reconstructions formed the test dataset.

Initially, several shallow neural networks with three to five convolutional layers were trained. During their training, various settings for parameters such as learning rate, minibatch size, number of epochs, etc., were experimented with. A dropout layer was also applied, which randomly deactivates neurons during training to prevent overfitting of the network and to increase reliability when evaluating new data. The best result during validation of these networks was approximately 90% accuracy (on the validation dataset). This result does not provide a high degree of reliability. The reason could be the still small number of images and the shallow depth of the network, which may not capture the complexity of evaluating image quality.

In the next step, the ResNet-50 convolutional neural network, which is already pretrained for classification tasks and is available from MathWorks, was therefore trained. This network contains 50 convolutional neural layers and should better propagate gradients, as it uses residual connections. The training of this network is shown in Figure 2.53.
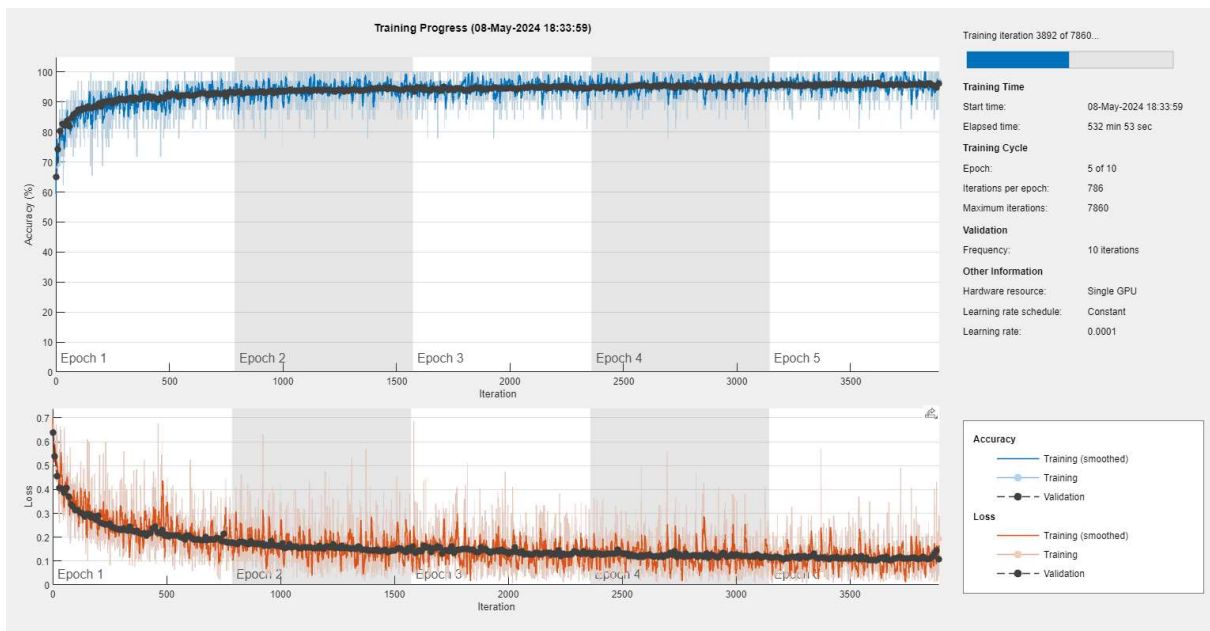
Figure 2.53 Visualization of neural network training.

Training was stopped after five epochs when training loss began to increase. The network validation reached 96.2%, which represents a promising result.

This neural network was applied to previously unseen data from different CT reconstructions. The classification success of these data is illustrated by the confusion matrix in Figure 2.54. Zero represents the class where errors were found in evaluating the patency of the channels, and one indicates the class of images that were evaluated without error.
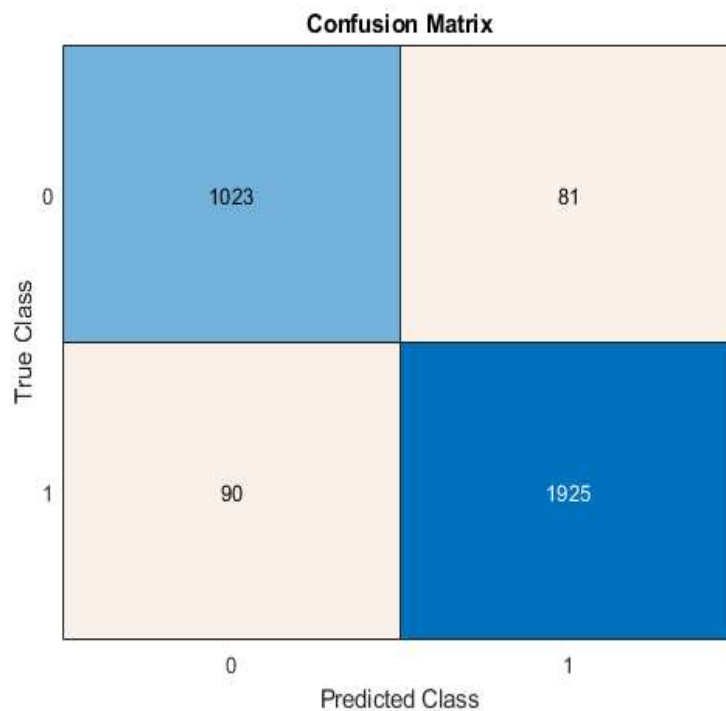

Figure 2.54 Confusion matrix classification of test data.

The numbers in the confusion matrix indicate that the network correctly identified 1023 images where errors occurred during evaluation (True Negatives – TN), but 81 inappropriate images were marked as suitable (False Positive – FP). Additionally, 1925 images were correctly identified as suitable for evaluation (True Positives – TP) and 90 images were marked as unsuitable, although they were suitable (False Negatives – FN).

From these values, certain parameters can be determined, such as the overall accuracy of the network, Recall, which represents the rate of correct identification of a given class, Precision, which is a parameter expressing the number of correctly identified images in a given class compared to all images of that class, and the $F1$ score, which is used for comparing different models.

$$A = \frac{TP + TN}{TP + FP + TN + FN} = \frac{1925 + 1023}{1925 + 90 + 1023 + 81} = 94{,}52\ \%, \tag{2.20}$$

$$P_1 = \frac{TP}{TP + FP} = \frac{1925}{1925 + 90} = 95{,}53\ \%, \tag{2.21}$$

$$R_1 = \frac{TP}{TP + FN} = \frac{1925}{1925 + 81} = 95{,}96\ \%, \tag{2.22}$$

$$F1_1 = 2 \cdot \frac{P_1 R_1}{P_1 + R_1} = \frac{0{,}9553 \cdot 0{,}9596}{0{,}9553 + 0{,}9596} = 95{,}74\ \%, \tag{2.23}$$

$$P_0 = \frac{TN}{TN + FN} = \frac{1023}{1023 + 81} = 92{,}66\ \%, \tag{2.24}$$

$$R_0 = \frac{TN}{TN + FP} = \frac{1023}{1023 + 90} = 91{,}91\ \%, \tag{2.25}$$

$$F1_0 = 2 \cdot \frac{P_0 R_0}{P_0 + R_0} = \frac{0{,}9266 \cdot 0{,}9191}{0{,}9266 + 0{,}9191} = 92{,}45\ \%, \tag{2.26}$$

where A is the overall accuracy, P is precision, R is recall, and the indices 1 or 0 correspond to the individual classification classes.

These results can be interpreted to mean that the overall accuracy (Accuracy) and $F1$ score are relatively high for both classes, which would suggest that the model is capable of effectively identifying both classes. The recall values indicate that the model can distinguish well between the classes, and along with the relatively low number of false positives and negatives, this suggests good results on unseen data.

This model was then applied to images that were exported using the macros mentioned in this work. In determining the quality of images during their evaluation, a confusion matrix was found, which is shown in Figure 2.55.

This result is significantly worse than when classifying the test data. The individual indicators have the following values:
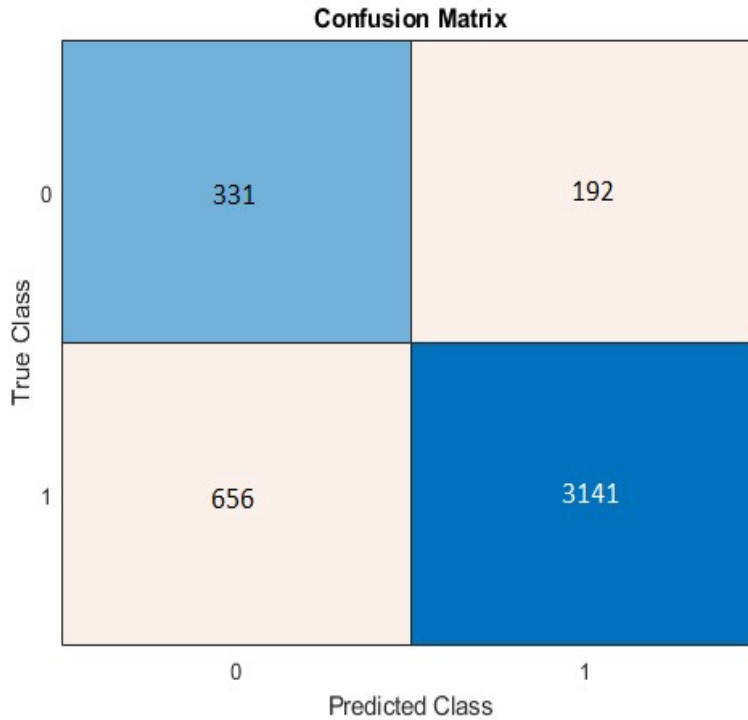
Figure 2.55 Confusion matrix classification during evaluation.

$$A = \frac{TP + TN}{TP + FP + TN + FN} = \frac{3141 + 331}{3141 + 656 + 331 + 192} = 80,37 \text{ \%},\tag{2.27}$$

$$P_1 = \frac{TP}{TP + FP} = \frac{3141}{3141 + 656} = 82,72 \text{ \%},\tag{2.28}$$

$$R_1 = \frac{TP}{TP + FN} = \frac{3141}{3141 + 192} = 94,24 \text{ \%},\tag{2.29}$$

$$F1_1 = 2 \cdot \frac{P_1 R_1}{P_1 + R_1} = \frac{0,8272 \cdot 0,9424}{0,8272 + 0,9424} = 88,11 \text{ \%},\tag{2.30}$$

$$P_0 = \frac{TN}{TN + FN} = \frac{331}{331 + 192} = 63,29 \text{ \%},\tag{2.31}$$

$$R_0 = \frac{TN}{TN + FP} = \frac{331}{331 + 656} = 33,54 \text{ \%},\tag{2.32}$$

$$F1_0 = 2 \cdot \frac{P_0 R_0}{P_0 + R_0} = \frac{0,6329 \cdot 0,3354}{0,6329 + 0,3354} = 43,84 \text{ \%},\tag{2.33}$$

The overall accuracy of the network when evaluating composite images is 80.37%. While good images are identified with relatively high precision, the network very inaccurately detects images on which evaluation is done incorrectly.

One possible explanation for this situation is that the training dataset was not balanced. Out of the 31 475 images used, 10 003 were in category 0 and 21 472 in category 1. Therefore, the network learned to recognize good images better.

Another possible explanation for the deterioration in image classification results is that in the evaluation in MATLAB, a single image is composed of seven exported images, which is then evaluated. The network was trained on images that were not composed of multiple other images, primarily due to their quantity.

Overall, it can be said that evaluating image quality using a neural network has yielded results and proved to be useful. The network is relatively accurate in determining good images, but very unreliable in determining bad images. To improve the network's accuracy, it would be necessary to gather a larger number of images, especially images from category 0, and retrain the network on them. Changing the network architecture or suitable image filtering could also positively influence the model.

2.10 DISCUSSION OF THE SOLUTION AND RESULTS

The results of the algorithmic evaluation indicate that the chosen approach to this task is functional. The average success rate for determining the channel throughput is greater than 95% for both the test data and the data used to debug the algorithm. Therefore, the approach chosen was to use the commercial software VGSTUDIOMAX to determine the 3D reconstruction after scanning the CT data and then automatically export the sections at predefined levels. The selection of this specific approach was influenced by a number of factors. One of the most significant was the requirements of Hanon, which stipulated that the output should be in the form of software or other know-how that would be primarily in the hands of Hanon. A commercial licence of the VGSTUDIOMAX software is very expensive and unprofitable for Hanon. For this reason, part of the evaluation is being carried out by CEITEC. This is the part of the algorithm that is performed in VGSTUDIOMAX. Therefore, the work with this software was limited to the minimum necessary to handle the required task.

A number of alternative approaches to CT data evaluation were discussed during the solution. The first option is to perform the entire image evaluation in the VGSTUDIOMAX software, where the information about the channel occlusion would be obtained not from the 2D images but from the 3D reconstruction itself. This approach necessitates a profound familiarity with the VGSTUDIOMAX software, which may also entail the development of bespoke functions and scripts within this environment. The potential outcome is a highly sophisticated tool. The full automation of this process is open to further discussion, given that at the outset of any evaluation, there will always be the task of spatial determination of CT data, for which there is, in principle, only the *BestFit* function. The principal disadvantage of this approach is that all the expertise remains concealed within the functions and the programmed matrix for the commercial tool VGSTUDIOMAX, which Hanon does not possess.

The second alternative and also discussed approach is the complete processing of CT data in Matlab or Python. This approach involves working with 3D data in these programming tools, which is very demanding on the operating memory of the computer. To provide an example, a scan of one section that is already reduced to the region of interest represents approximately 8 GB of data. It should be noted that few tools exist for working with 3D data in Matlab or

Python. Therefore, it would be necessary to develop a method for spatially identifying this data in the first step. The question remains whether a more accurate method for this application could be found than the *BestFit* function in the commercial VGSTUDIOMAX software environment. In the event that such a method cannot be identified, spatial alignment in a commercial tool would have to be performed, or the automatic spatial determination would have to be abandoned. The significant advantage of this approach is that the evaluation is conducted in only one application and tool that Hanon owns. Consequently, the developed methodology would be within their control.

It is evident that numerous alternative approaches could be conceived to address this issue. The methodology employed in this thesis was designed to ascertain the viability of automated CT data evaluation. Consequently, a straightforward solution was devised, integrating the strengths of both the commercial software VGSTUDIOMAX and the flexibility of customising functions within the Matlab environment. The commercial software is always necessary for CT reconstruction processing because it provides the calculation of 3D reconstruction from a large number of 2D projections. The objective of the proposed algorithm was to follow the reconstruction process and perform the remaining evaluation fully automatically.

The spatial determination of the CT reconstruction in space proved to be a significant technical challenge, which has a considerable impact on the reliability of the entire method. Consequently, it represents a significant weakness in a large algorithm that requires effective improvement. Two potential solutions are presented. The first is to eliminate the fully automatic spatial alignment and perform it manually. This will also ensure its correct execution at all times. The second option is to design and construct a suitable clamping stand for the gascooler to ensure the scan is always in a defined and known position. Ideally, it would be advisable to provide the stand with small metal objects of defined shape made of the same or other material. The size of the object could be approximately 3 mm. This object should then be modelled as part of the .step model of the gascooler.

Once the gascooler has been scanned on a fabricated stand with an integrated metal licence plate, a 3D model can be reconstructed containing this metal plate at defined locations. If the exact position of the gascooler is known in advance during scanning and combined with the metal markers, it would be possible to perform an extremely accurate automatic alignment of the model in space. The accuracy of the stand in which the gascooler is to be mounted during scanning is expressed in millimetres, in order that the software may automatically detect and correctly match the corresponding surfaces. In essence, this approach mechanically preassembles the model. The fitting is only fine-tuned by the software. The markers are for better orientation and should facilitate the assembly of the CT data and the CAD model.

Once the CT data and CAD model have been accurately aligned, it is necessary to identify the appropriate planes from which the sections are to be exported. In the current approach, sections are exported from planes. To ensure better images and a more accurate identification of the surface of the channels, which may be axially deformed in some places as seen in Figure 2.56. It is necessary to develop a method to detect the axis-like or any other sagging of the channels, to interleave this sagging with a mathematical surface, and to export a snapshot of this surface. This phenomenon is not unique and makes the export of suitable sections very difficult. In this approach, the issue is partially mitigated by exporting seven images from seven planes situated within a single channel. These images are then composited into a single representative image. However, a more optimal solution would be to develop a method for detecting axis-like or any

other sagging of the channels, interleaving this sagging with a mathematical surface, and exporting a snapshot of this surface.
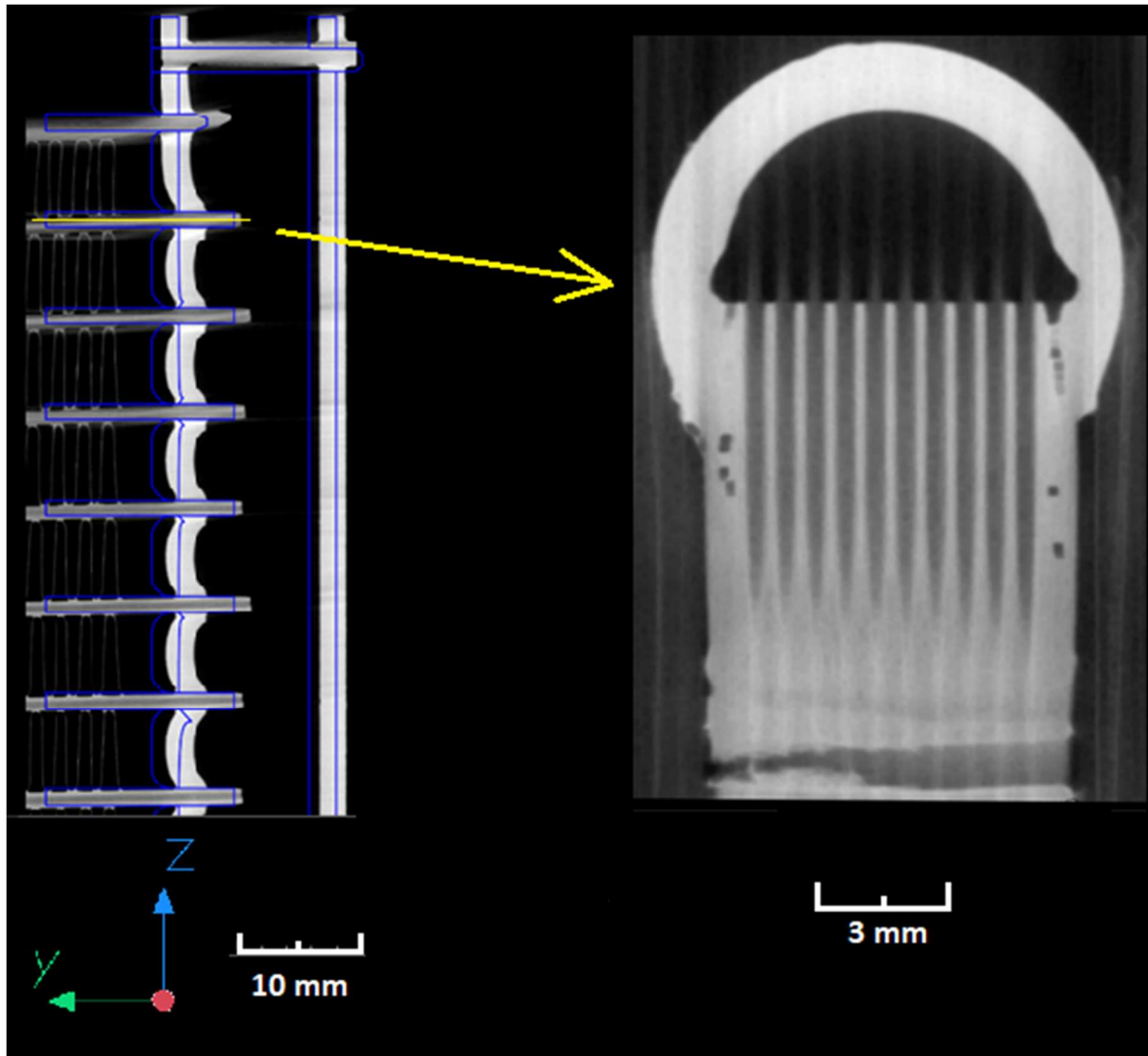

Figure 2.56 Ace-shaped tube deformation.

Once this has been completed, precise cuts would be exported, which would be easily readable and identifiable in the created tool in Matlab. The simple application in Matlab could be further developed and its algorithm improved to make it more robust for take evaluation. A major area for improvement is to design a suitable quality assessment of the input images so that the software can reliably exclude from the evaluation those images where it would make an error in the evaluation. These locations would be evaluated in turn by the operator.

CONCLUSION

This thesis addresses the algorithmisation and automation of the process of evaluating the channel throughput in a gascooler. In the theoretical section, the differences between gascoolers and condensers, which are used in air conditioners in order cars, are discussed. Subsequently, common manufacturing defects of gascoolers and techniques for their detection are considered. The thesis devotes considerable attention to the CT scanning method, describing the generation and detection of X-rays and the creation of a 3D reconstruction of the scanned object. The theoretical part of the thesis contains a review of commercial and freely available software for the visualisation, manipulation and analysis of CT data, which are used both in medical and industrial applications. A significant portion of the research involved the manipulation and processing of two-dimensional images within the Matlab environment. This included the application of histogram equalization and frequency analysis techniques, which were employed to identify the principal axes of the image.

In the practical part of the thesis, the approach to the evaluation of the clogging of gascooler channels, which occurs in the process of their production, is analysed in detail. The scanning process is modified to make it algorithmisable. The change consists in the use of multiscan and the division of the scanned piece into four sections, instead of the previous eight sections. This facilitates the algorithmic approach. Furthermore, a workflow for an automatable approach to slide evaluation is proposed, where the whole process is divided into two steps. The first step is the spatial determination of the CT reconstruction and the subsequent export of 2D slices from the channel plane regions. This step takes place in the commercial software VGSTUDIOMAX and is fully automated by a user-run macro during the evaluation. The output of this section is a directory of ordered images of the gascooler slices from the predefined gascooler planes.

The second step is to process these images in the Matlab environment using the Image Processing Toolbox libraries designed for working with images. Due to the difficulties in automatic prosore determination of CT reconstruction and to increase the robustness of the solution, seven slices are exported from each axial plane, from which one image is created at the beginning of processing in Matlab. Next, the smeared images are identified for evaluation, which are ordered and numbered according to their position on the actual slice. Subsequently, each image is subjected to a series of adjustments with the objective of achieving an appropriate binarisation. To this end, a bespoke function has been devised to modify the pixel intensities in accordance with the values of their surrounding regions.

Once the intensity has been adjusted, the image is binarised, with the dark background being separated. This adjusted image then enters the generated image rotation detection function, which is able to identify the main direction of the image and its rotation relative to the vertical direction by integrating the amplitude spectrum of the image. Subsequently, a correction is performed. Prior to the actual evaluation, important edges of the image are detected. The binarised image is cropped to only the channel region, which is now vertical. After adjusting the image to a width of 500 pixels, the columns of pixels in the channel region are identified. These columns are approximately 20 per channel. The sum of the pixels in these columns is used to identify whether there is material in the channel area (the channel is blocked – there are white pixels) or whether there are black pixels in the channel boundary, i.e. the channel is passable.

The information regarding the patency of the channel is recorded in the result vector, where the value 0 represents a passable channel and the value 1 represents a blocked channel. Finally, the vectors are assembled into a result matrix, where the rows of the matrix represent individual channel planes and the positions in the rows of the matrix represent individual channels. The arrangement of the result matrix is predetermined.

Furthermore, the evaluation algorithm incorporates additional features for the early detection of spatial misdetermination of CT reconstruction using the *BestFit* function in the commercial software VGSTUDIMAX. The detection of errors in the spatial determination of CT data from which 2D slices have been extracted is of paramount importance for the correct assignment of images to individual channel planes on the real gascooler.

Furthermore, efforts were made to evaluate the input frames to the algorithm in Matlab with the objective of detecting inappropriate frames in which channel patency misdetermination occurs. A deep convolutional neural network comprising fifty layers was trained for this purpose. The pre-trained ResNet network available in Matlab, which was trained on more than 31,455 images divided into two categories, was utilised. The images were categorised as those that the algorithm evaluated completely correctly and those that the algorithm evaluated incorrectly. The image sorting process involved exporting the images from the CT data and manually evaluating them initially. Subsequently, the images were evaluated by the developed software. If the result of the automated evaluation was identical to that of the initial evaluation, the image was marked as having been initially evaluated, and vice versa.

Upon testing the learned model on unseen data representing more than 3,000 images, an overall accuracy of 94.52% was achieved. However, after implementing this model in the aliquot, the overall accuracy of the model dropped to 80.37%. It has been observed that the model has a tendency to identify unsuitable images as suitable for evaluation. One potential explanation for this discrepancy is the imbalanced nature of the training dataset, which comprised over 21,000 high-quality images and only 10,000 low-quality images.

The entire algorithm, created in Matlab, was finally processed in the form of a simple user application executable on a PC without the need for a Matlab licence. This allows either the evaluation of the entire gascooler at once or of some of its four sections separately. The results are copied by the user to the clipboard with one button and can be pasted into a prepared and already used MS Excel spreadsheet.

The algorithm for assessing gascooler duct patency from CT reconstructions was calibrated on eight CT reconstructions, achieving an average success rate of 95.38%. The success rate was determined by comparing the result matrix obtained by manual evaluation with the result matrix obtained by automated honing, which included not only the processing in MTLAB but also the tasks automated in the VGASTUDIOMAX software. Finally, the algorithm was tested on two additional datasets that had not been seen before and were selected at random. It achieved a success rate of 98.18%.

The weakest point of the whole algorithm was identified as the spatial determination task of the CT data in VGSTUDIOMAX, which greatly affects the exported slices. If this task is not performed accurately, the exported sections lack adequate image information and cannot be validly evaluated.

The proposed enhancement to the algorithm primarily entails the improvement and augmentation of the spatial determination of CT data subsequent to their reconstruction and the optimisation of the interleaving of channel planes. This approach has been demonstrated to be effective in interleaving with a mathematical curve, rather than a plane alone. This necessitates the utilisation of expert knowledge with the VGSTUDIOMAX software. A second significant enhancement could be the development of a more dependable assessment of the software input frames in Matlab. This would identify inappropriate frames and specific locations would be subject to manual examination.

RESOURCES

[1] JURIGA, J. *Design of pressing machines for manifold assembly of condensers in car air-conditioning unit.* Brno: Brno University of Technology, Faculty of mechanical ingeneering, 2016. 112 p. Master thesis supervisor doc. Ing. Radek Knoflíček, Dr.

[2] BEZDĚK, L. *Testing method of car air-contions.* Brno: Brno University of Technology, Faculty of mechanical ingeneering, 2009. 46 p. Bachelor thesis supervisor doc. Ing. Josef Štětina, Ph.D.STONE, Richard. *Introduction to Internal Combustion Engines.* Fourth Edition. Basingstoke: Palgrave Macmillan, 2012. ISBN 978-0-230-57663-6.

[3] PAVELEK, Milan et al. *Termomechanika.* 1. ed. Brno: Cerm, 2011. ISBN 978-80-214-4300-6.

[4] CZECH NEWS CENTER A.S. *První auto s klimatizací stálo skoro dva roční příjmy. Vpředu vůbec nefoukala a zabírala místo, kde ho bylo potřeba nejvíce.* Online. AUTOREVUE.CZ. 17 June 2023n. l. Dostupné z: https://www.autorevue.cz/prvni-auto-s-klimatizaci-stalo-skoro-dva-rocni-prijmy-vpredu-vubec-nefoukala-a-zabirala-misto-kde-ho-bylo-potreba-nejvice. [cit. 2024-05-24].

[5] How the cooling works. In: Chladírenský servis Jedlička [online]. Plzen: CHLADÍRENSKÝ SERVIS JEDLIČKA, s.r.o., 2015 [cit. 2024-01-03]. Accessed from: https://www.chsjedlicka.cz/rady/jak-funguje-chlazeni/

[6] PAVLŮ, Jaroslav. *Computing software and methodology development tor refrigeration minichannel condenser evaluation.* Brno, 2012, 150 p. PhD thesis. Brno University of Technology, Faculty of Mechanical Engineering. Thesis supervisor doc. Ing. Jiří Pospíšil Ph.D.

[7] LinkedIn Corporation. www.slideshare.net. SlideShare: Automotive air conditioning training manual. [online]. 2016 [cit. 2024-02-25]. Accessed from: http://www.slideshare.net/taufiqatan1/automotive-air-conditioning-training-manual

[8] Online. Spares Direct. Available from: https://sparesdirect.co.za/product/vw-golf-7-condenser-1-2t-1-4t-2-0t-2-0d-13-21/. [cit. 2024-01-21].

[9] Jan Doležal *Draft cooling system for food.* Brno, 2015. 186 p., 16 p. appendices Bachelor thesis. Brno University of Technology, Faculty of Civil Engineering, Department of Technical Equipment of Buildings. Thesis supervisor Ing. Marian Formánek, Ph.D.

[10] PÍREK, Ondřej. *Cooling systems for catering operations.* [online]. Brno, 2023 [cit. 2023-01-12]. Master thesis. Brno University of Technology, Faculty of Civil Engineering, Department of Technical Equipment of Buildings. Thesis supervisor Ing. Marian Formánek, Ph.D. Accessed from: https://www.vutbr.cz/studenti/zav-prace/detail/143463.

[11] Carbon Dioxide (R744) - The New refrigerant 2017 [cit. 2024-01-15]. Downloaded from: https://www.ohio.edu/mechanical/thermo/Intro/Chapt.1_6/Chapter4c.html

[12] COUNCIL OF THE EUROPEAN UNION. Proposal for a Regulation of the European Parliament and of the Council on fluorinated greenhouse gases, amending Directive (EU)

2019/1937 and repealing Regulation (EU) No 517/2014: Letter to the Chair of the European Parliament Committee on the Environment, Public Health and Food Safety (ENVI). In: . 2023, Interinstitutional File: 2022/0099(COD), p. 206. Accessed from: chrome-extension://efaidnbmnnnibpcajpcglclefindmkaj/https://eur-lex.europa.eu/legal-content/EN/TXT/PDF/?uri=CONSIL:ST_14409_2023_INIT

[13] ENTALPIA EUROPE. *Chladiva ze skupiny HFO (R1234yf, R1234ze) – význam a použití* [online]. [cit. 2024-01-24]. Accessed from: https://entalpiaeurope.eu/cs/chladiva-ze-skupiny-hfo-r1234yf-r1234ze-vyznam-a-pouziti/

[14] ŠTUDLAR, Václav. *Změny v technologii chlazení s důrazem na environmentální dopady a s ohledem na legislativní omezení.* [online]. Plzeň, 2018, 63 p. [cit. 2024-01-24]. Accessed from: chrome-extension://efaidnbmnnnibpcajpcglclefindmkaj/https://dspace5.zcu.cz/bitstream/11025/31367/1/Studlar%20Vaclav-DP%202018.pdf. Master thesis. University of West Bohemia in Pilsen, Faculty of Mechanical Engineering. Thesis supervisor doc. Ing. Michal Edl, Ph.D.

[15] MYSLIKOVJAN, Martin. *Design of inner condenser - heat exchanger for R744 refrigerant* [online]. Plzeň, 2018, 105 s. [cit. 2024-01-24]. Accessed from: chrome-extension://efaidnbmnnnibpcajpcglclefindmkaj/https://dspace5.zcu.cz/bitstream/11025/33357/1/Martin_Myslikovjan_final.pdf. University of West Bohemia in Pilsen, Faculty of Mechanical Engineering. Thesis supervisor doc. Ing. Václava Lašová, Ph.D.

[16] HELLIER, Charles J. Handbook of nondestructive evaluation. Third ed. New York: McGraw-Hill, [2020]. ISBN 978-1260441437.

[17] KOPEC, Bernard a BRODSKÝ, Bohumil. *Nedestruktivní zkoušení: defektoskopie : encyklopedický přehled metod nedestruktivního zkoušení materiálů a výrobků.* 2013. Brno: Czech Society for Non-Destructive Testing, 2013. ISSN issn1213-3825.

[18] SWAIN, Michael V a XUE, Jing. State of the Art of Micro-CT Applications in Dental Research. Online. International Journal of Oral Science. 2009, roč. 1, č. 4, s. 177-188. ISSN 1674-2818. Available from: https://doi.org/10.4248/IJOS09031. [cit. 2024-05-21].

[19] MARTZ, Harry E., Clint M. LOGAN, Daniel J. SCHNEBERK a Peter J. SHULL. *X-Ray Imaging: Fundamentals, Industrial Techniques and Applications*. 1st Edition. CRC Press: Boca Raton: Taylor & Francis, 2017. ISBN 9780849397721.

[20] DE CHIFFRE, L., S. CARMIGNATO, J.-P. KRUTH, R. SCHMITT a A. WECKENMANN. Industrial applications of computed tomography. *CIRP Annals*. 2014, **63**(2), 655-677. ISSN 00078506. Available from: doi:10.1016/j.cirp.2014.05.011

[21] STOCK, Stuart. *Microcomputed tomography: methodology and applications*. Boca Raton: CRC Press, 2009. ISBN 978-142-0058-765.

[22] CARMIGNATO, Simone, Wim DEWULF a Richard LEACH, ed. *Industrial X-Ray Computed Tomography*. 1 edition. Cham: Springer, 2018. ISBN 9783319595719. Available from: doi: https://doi.org/10.1007/978-3-319-59573-3

[23] SUN, W.; BROWN, S. B.; LEACH, R. K. An overview of industrial X-ray computed tomography. 2012.

[24] FELDKAMP, Lee A.; DAVIS, Lloyd C.; KRESS, James W. Practical cone-beam algorithm. Josa a, 1984, 1.6: 612-619.

[25] CIERNIAK, Robert. *X-Ray Computed Tomography in Biomedical Engineering*. [online]. London: Springer London, 2011. ISBN 978-0-85729-026-7. Available from https://doi.org/10.1007/978-0-85729-027-4. [cit. 2024-01-25].

[26] PAN, Tinsu. Computed Tomography: from Photon Statistics to Modern Cone-Beam CT. [online]. *Journal of Nuclear Medicine*. 2009, vin. 50, č. 7, s. 1194-1194. ISSN 0161-5505. Available from: https://doi.org/10.2967/jnumed.109.064501. [cit. 2024-01-25].

[27] ŠALPLACHTA, Jakub. *Quantitative computed tomography*. Brno, 2023. Doctoral Thesis. Brno University of Technology, Central European Institute of Technology, Central European Institute of Technology BUT. Supervisor Jozef Kaiser.

[28] ALLÉ, P, E WENGER, S DAHAOUI, D SCHANIEL a C LECOMTE. Comparison of CCD, CMOS and Hybrid Pixel x-ray detectors: detection principle and data quality. *Physica Scripta*. 2016, **91**(6), 15. ISSN 0031-8949. Available from: doi:10.1088/0031-8949/91/6/063001

[29] YAFFE, M J a ROWLANDS, J A. X-ray detectors for digital radiography. [online]. Physics in Medicine and Biology. 1997, vin. 42, č. 1, s. 1-39. ISSN 0031-9155. Available from: https://doi.org/10.1088/0031-9155/42/1/001. [cit. 2024-02-27].

[30] HAO YAN a XUANQIN MOU. Projection correlation based noise reduction in volume CT. [online]. In: IEEE Nuclear Science Symposuim & Medical Imaging Conference. IEEE, 2010, s. 2948-2953. ISBN 978-1-4244-9106-3. Available from https://doi.org/10.1109/NSSMIC.2010.5874336. [cit. 2024-02-27].

[31] SUN, W.; BROWN, S. B.; LEACH, R. K. An overview of industrial X-ray computed tomography. 2012.

[32] SMITH, Bruce D. Cone-beam tomography: recent advances and a tutorial review. [online]. Optical Engineering. 1990, vin. 29, č. 5. ISSN 00913286. Available from: https://doi.org/10.1117/12.55621. [cit. 2024-02-27].

[33] VOLUME GRAPHICS. VGSTUDIO MAX. [online]. Available from: https://www.volumegraphics.com/en/products/vgsm.html. [cit. 2024-05-02].

[34] THERMO FISHER SCIENTIFIC. Avizo. [online]. Available from: https://www.thermofisher.com/cz/en/home/electron-microscopy/products/software-em-3d-vis/avizo-software.html. [cit. 2024-05-02].

[35] SYNOPSYS. Simpleware. [online]. Available from: https://www.synopsys.com/simpleware.html. [cit. 2024-05-02].

[36] COMET TECH Dragonfly. [online]. Available from: https://dragonfly.comet.tech/. [cit. 2024-05-02].

[37] IMAGEJ. ImageJ development team. [online]. Available from: https://imagej.net/ij/docs/index.html. [cit. 2024-05-04].

[38] 3D SLICER. [online]. Available from: https://www.slicer.org/#what-is-3d-slicer. [cit. 2024-05-04].

[39] 3D SLICER. Slicer Read the Docs. [online]. Available from: https://slicer.readthedocs.io/en/latest/user_guide/about.html#what-is-3d-slicer. [cit. 2024-05-04].

[40] PIXMEO SARL. OsiriX [online]. © 2024. Available from: https://www.osirix-viewer.com/ [cit. 2024-05-04]

[41] KITWARE. ParaView [online]. © 2023. Dostupné z: https://www.paraview.org/ [cit. 2024-05-04]

[42] WALEK, Petr a JAN, Jiří. *Analýza biomedicínských obrazů*. Online. Second updated ed.. Brno: Brno University of Technology, 2015. ISBN 978-80-214-4792-9. [cit. 2024-05-04].

[43] JAN, Jiri: *Medical image processing, reconstruction and restoration: concepts and methods*. Boca Raton: Taylor & Francis, 2006, ISBN 0-8247-5849-8, 730 s.

[44] PETROU, Maria, Costas PETROU: *Image processing: the fundamentals*. Chichester: Wiley, second edition, 2010, ISBN 978-0-470-74586-1, 794 s.

[45] PIZER, Stephen M., E. Philip AMBURN, John D. AUSTIN, Robert CROMARTIE, Ari GESELOWITZ, aj.: *Adaptive histogram equalization and its variations*. 1987.

[46] ČÍŽEK, V. *Diskrétní Fourierova transformace a její použití*. 1. vydání. Praha: SNTL – Nakladatelství technické literatury, n. p., 1981. 160 s. Matematický seminář SNTL. ISBN 04-019-81

[47] DRUCKMÜLLEROVÁ, H. *Poznámky z aplikace fourierovy analýzy*. Online, výukový materíál. Brno: VUT Brno 2023. Available from: https://moodle.vut.cz/pluginfile.php/569293/mod_resource/content/2/Fourierka-1.pdf [cit. 2024-05-04].

[48] MATHWORKS, Inc. Image *Processing Toolbox™ User's Guide*. Online, Natick. MathWorks, Inc. 2024, Available from: chrome-extension://efaidnbmnnnibpcajpcglclefindmkaj/https://www.mathworks.com/help/pdf_doc/images/images_ug.pdf [cit. 2023-05-04].

[49] VOLUME GRAPHICS. *VGSTUDIOMAX Reference manual*. Heideberg. Volume Graphics GmbH 2023. [cit. 2023-05-06].

LIST OF ABBREVIATIONS AND SYMBOLS

|	
1D	One dimensional
2D	Two dimensional
3D	Three dimensional
4D	Four dimensional
ADC	Analog Digital Convertor
AI	Artificial intelligence
API	Application Programming Interface
BMP	Raster graphics image format
BSD	Family of permissive free software licenses
CAD	Computer aided design
CAE	Computed aided engineering
CCD	Charged Coupled Device
CMOS	Complementary Metal Oxide Conductor
CEITEC	Central European Institute of Technology
CERN	European Council for Nuclear Research
CFD	Computational fluid dynamics
CPU	Central Processing Unit
CT	Computed tomography
CTRL+V	keyboard shortcut used to paste information
DC	Direct Current
DFT	discrete Fourier transform
DN	Digital Number
DICOM	Digital Imaging and Communications in Medicine
DICOM-RT	Digital Imaging and Communications in Medicine extension for radiation therapy
ECT	Eddy current testing
e.g.	For example
FDK	Feldkamp Algorithm
FPD	Flat Panel Detector
FFT	fast Fourier transform
FIB-SEM	Focused Ion Beam in dual beam configuration with Scanning Electron Microscope
FITS	Flexible Image Transport System

FT		Fourier transform
GB		Gigabyte
GIF		file format for the compression and storage of visual digital information
GWP		Global Warming Potential
HPC		High Performance Computing
i.e.		That is
IR		Infra-red
JPEG		Joint Photographic Experts Group
MRI		Magnetic resonance imaging
MS		Microsoft
MSF		Metal Seal Fitting
NDT		Non Destructive Testing
PACS		Picture Archiving and Communication System
PCD		Photon Counting Detector
PET		File format in CT imaging
RAM		Random Access Memory
RGB		Red-Green -Blue
raw		uncompressed and unprocessed image data
SEM		Scanning Electron Microscope
SNR		Signal to Noise Ratio
s.r.o		Private limited company
STEP		File format of 3D model
TIFF		Tag Image File Format (format for storing raster images)
US		United States
UV		Ultraviolet
VG		Volume Graphics
XCT		X-Ray Compputed Tomography
A	[-]	brightness amplitude
A	[-]	Overall accuracy of a model
a	[-]	base of the exponential function
b_1, b_2, b_3, b_4	[-]	Coefficients for bilinear transformation
c	[ms^{-1}]	speed of light
$\boldsymbol{d}$	[px]	vector of distances from the image centre
E	[eV]	energy of the photon

|		
$F1$	[-]	F1 score
FN	[-]	False negatives
FP	[-]	False positives
$F_{m,n}$	[-]	complex spectral coefficient values
f	[Hz]	frequency of the photons
$f(j)$	[-]	interpolated value of the amplitude spectrum at the corresponding discrete point
$f_{i,k}$	[-]	pixel value of the image
$f(x,y)$		image
$g(x,y)$		image
$g_{i,k}$	[-]	intensity values of pixels in the output image
h	[Js]	Planck's constant
h^f		Histogram of image $f(x,y)$
h^g		Histogram of image $g(x,y)$
$h(p)$	[-]	Value of intensity in the pixel p
I_i	[-]	Result of integration along one integration line
i	[-]	Index of particular window
$i,k.$	[-]	Indexes of pixels
$LocThrshld_i$	[-]	threshold value for a particular window
m,n	[-]	Indexes of pixels
$MaxPix_i$	[-]	highest pixel value in particular window
$MinPix_i$	[-]	lowest pixel value in particular window
N	[-]	number of signal samples
P	[-]	Precision
p_{ij}	[px]	Pixel on coordinates i,j
r,q	[-]	Number of grayscale levels
r	[px]	Circle with same center and radius of 80% of R
R	[-]	Recall
R	[px]	inscribed circle
T	[m]	thickness of detector
TN	[-]	True negatives
TP	[-]	True positives
s_x, s_y	[px]	coordinates of the image centre
u_0, v_0	[rad]	angular frequencies, i.e. the number of cycles per unit
x	[px]	Length in x axis

x	[-]	pixel intensity value increase coefficient
y	[px]	Length in y axis
$\boldsymbol{x_i}, \boldsymbol{y_i}$	[px]	vectors of coordinates of points along the integration line
$\Delta x, \Delta y$	[-]	weights for bilinear transformation
x_{down}	[px]	nearest lower coordinates of the pixel
x_{up}	[px]	nearest higher coordinates of the pixel
y_{down}	[px]	nearest lower coordinates of the pixel
y_{up}	[px]	nearest higher coordinates of the pixel
γ	[-]	gamma parameter
θ_i	[°]	angle of the corresponding integration line
λ	[m]	wavelength of radiation
μ	[keV]	total absorption of radiation
μ_{PE}	[keV]	absorption coefficient due to photoelectric effect
μ_{CS}	[keV]	absorption coefficient due to Compton scattering
μ_{RS}	[keV]	absorption coefficient due to Rayleigh scattering
μ_{PP}	[keV]	absorption coefficient due to pair production
μ	[keV]	Linear attenuation coefficient
ρ_2	[px]	Linear distance from center to the pixel
φ	[rad]	phase
φ	[°]	correction angle
$\varphi_{1\,max}$	[°]	maximum found around 90°
$\varphi_{2\,max}$	[°]	maximum found around 180°

LIST OF ATTACHMENTS

Attachment 1. Step-by-step evaluation of a good quality image
Attachment 2. Step-by-step evaluation of a very low contrast image
Attachment 3. Step-by-step evaluation of a lower contrast image
Attachment 4. Step-by-step evaluation of an image with confluent channel mouth and lower contrast
Attachment 5. Step-by-step evaluation of a rotated image with a thin wall
Attachment 6. Step-by-step evaluation of an image with a thin wall
Attachment 7. Step-by-step evaluation of a good image with a slightly lower contrast
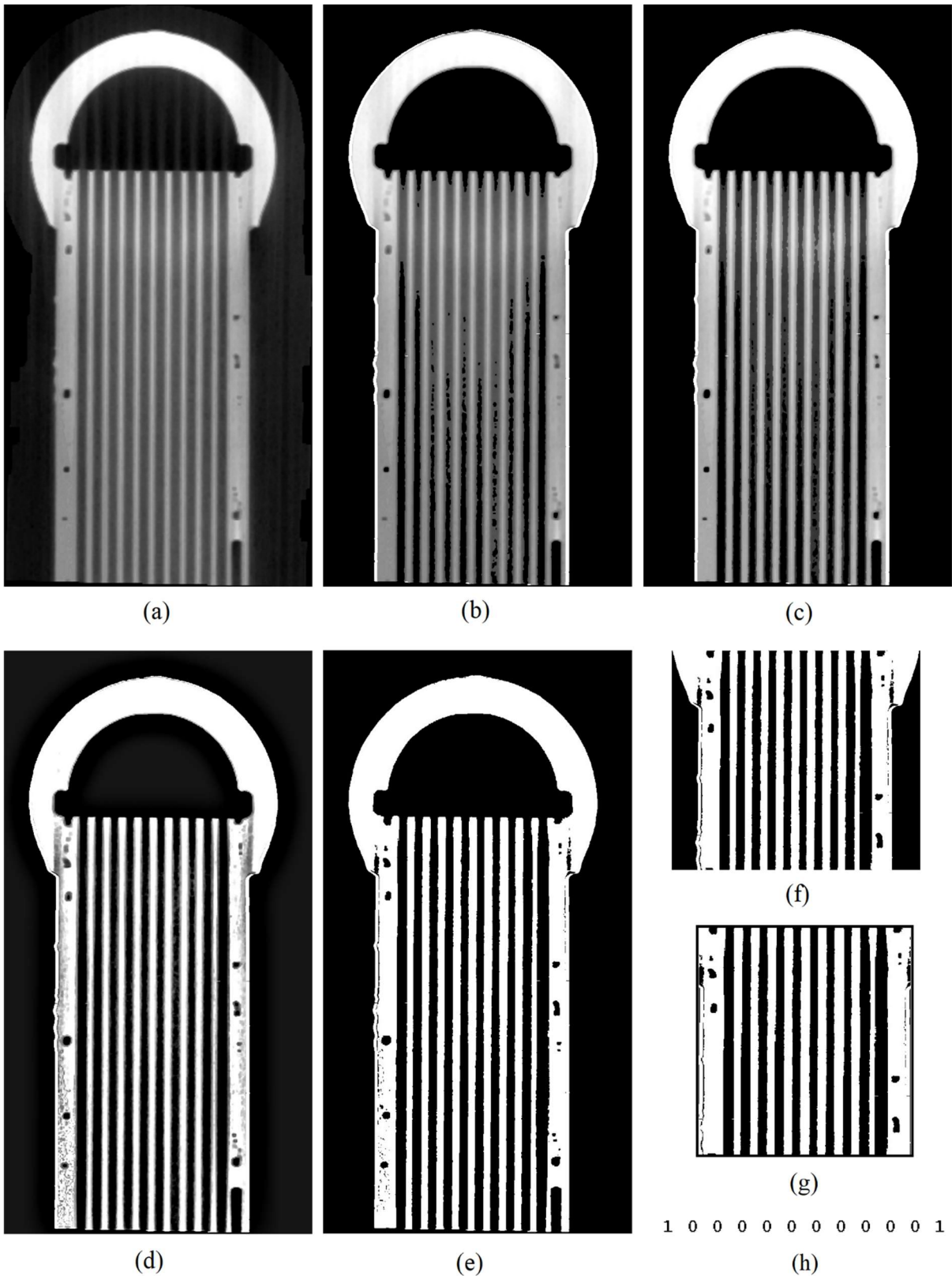
Attachment 1 Step-by-step editing of a good quality image: (a) Raw image (b) Highted edges by `highlightEdges` function (c) Image after contrast adjustment (d) Sharpened image (e) Binarized image (f) Image reducet from the upper and bottom side (g) Image reduced to only tube part (h) Result vector
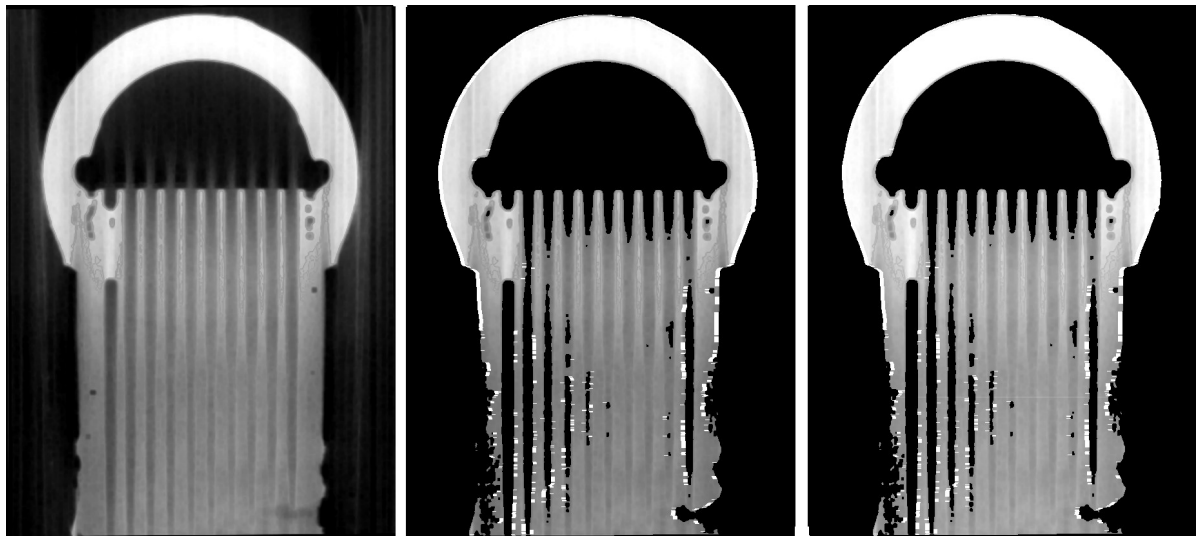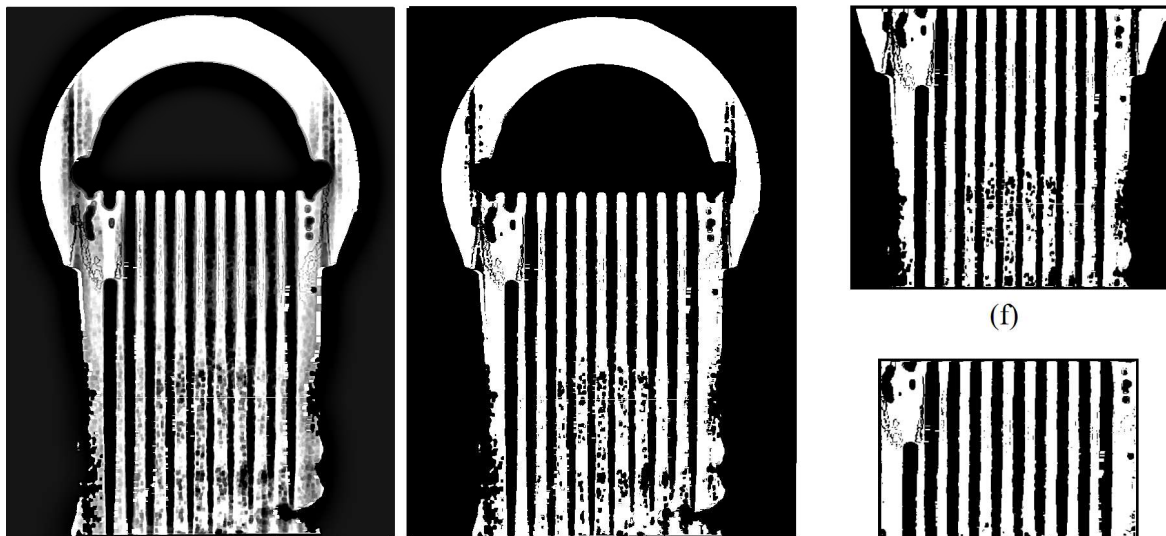
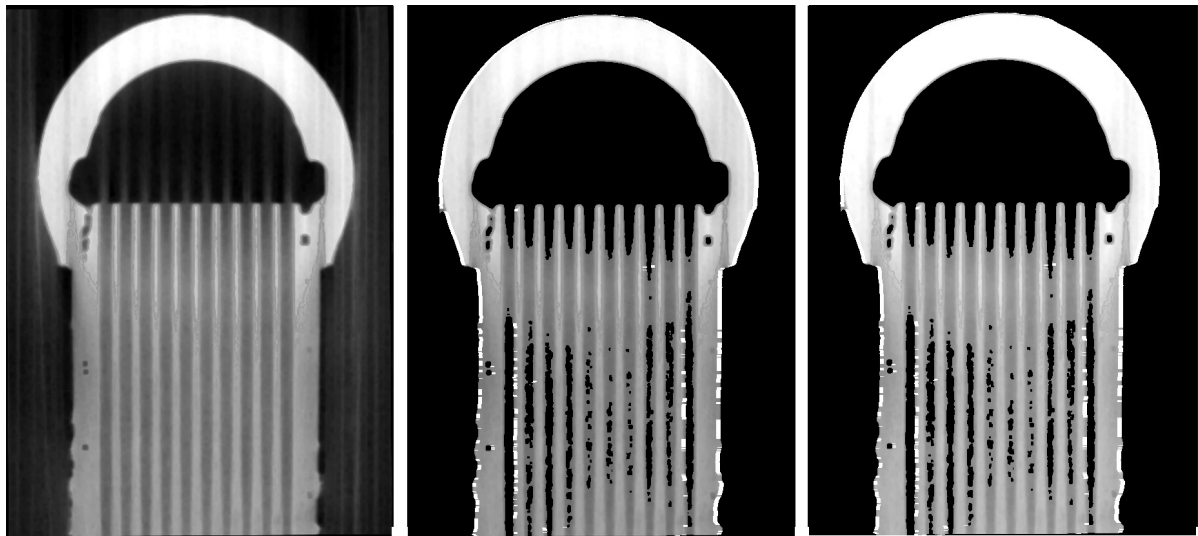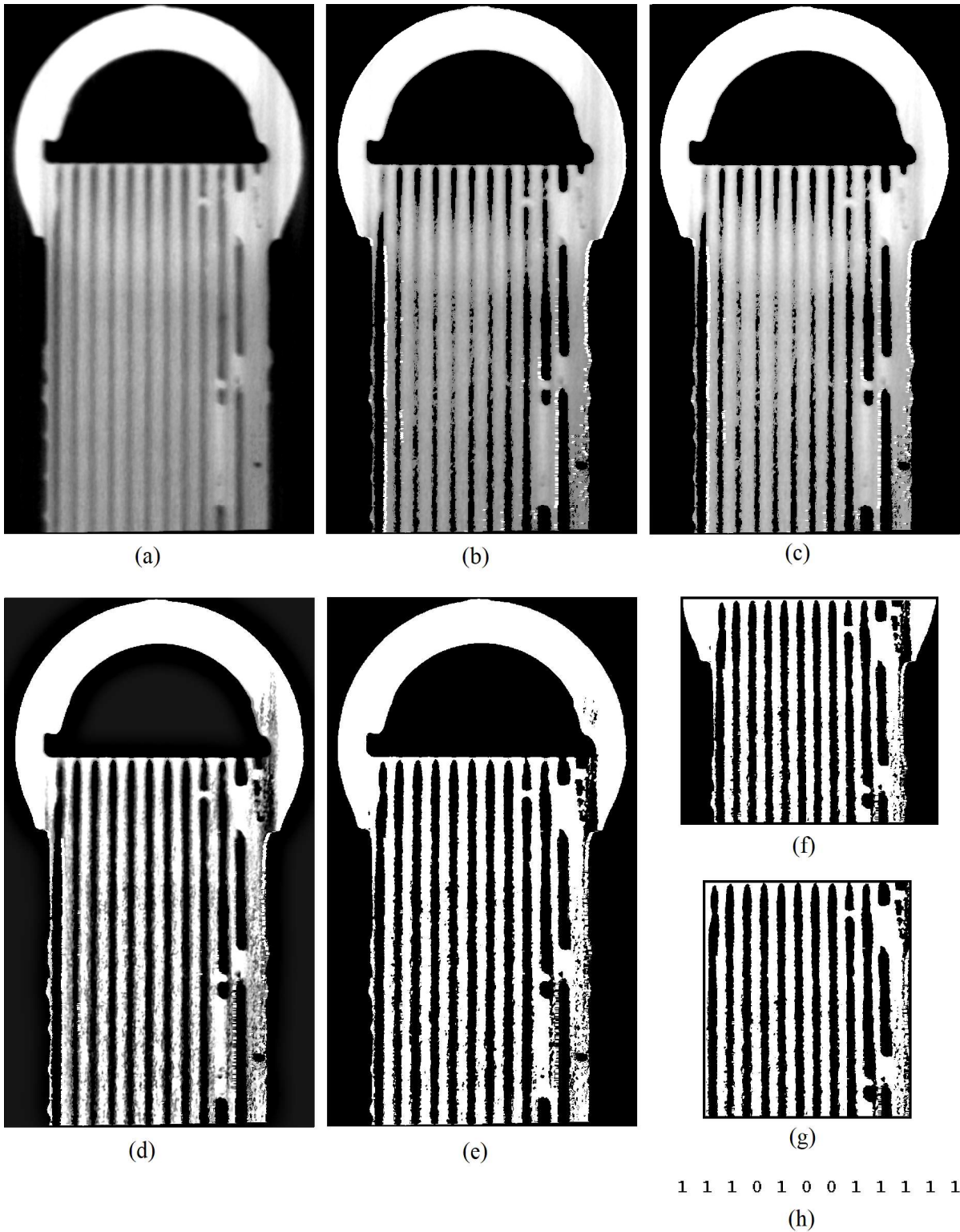Attachment 2 Step-by-step editing of a very low contrast image: (a) Raw image (b) Highted edges by `highlightEdges` function (c) Image after contrast adjustment (d) Sharpened image (e) Binarized image (f) Image reducet from the upper and bottom side (g) Image reduced to only tube part (h) Result vector
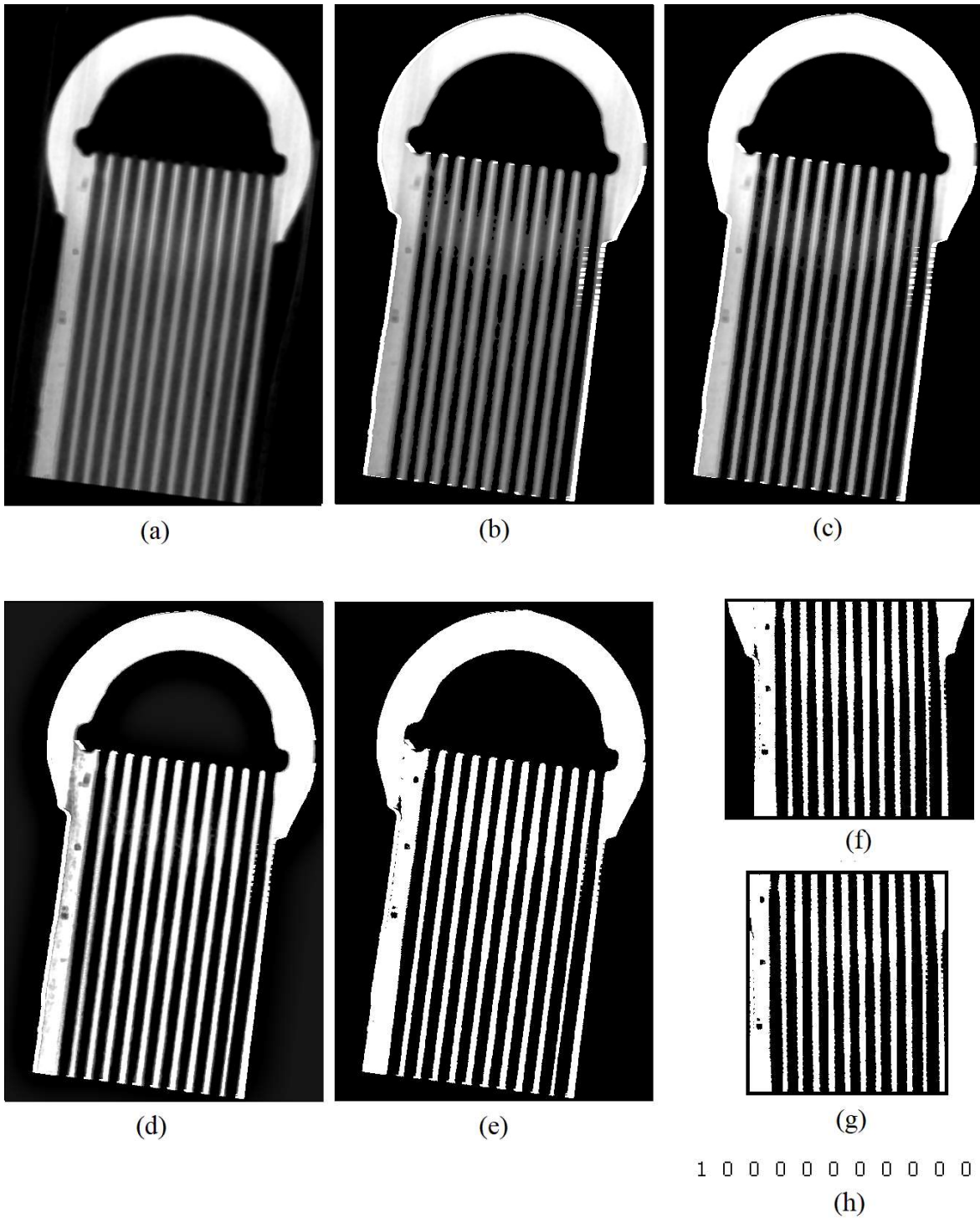
(a)

(b)

(c)

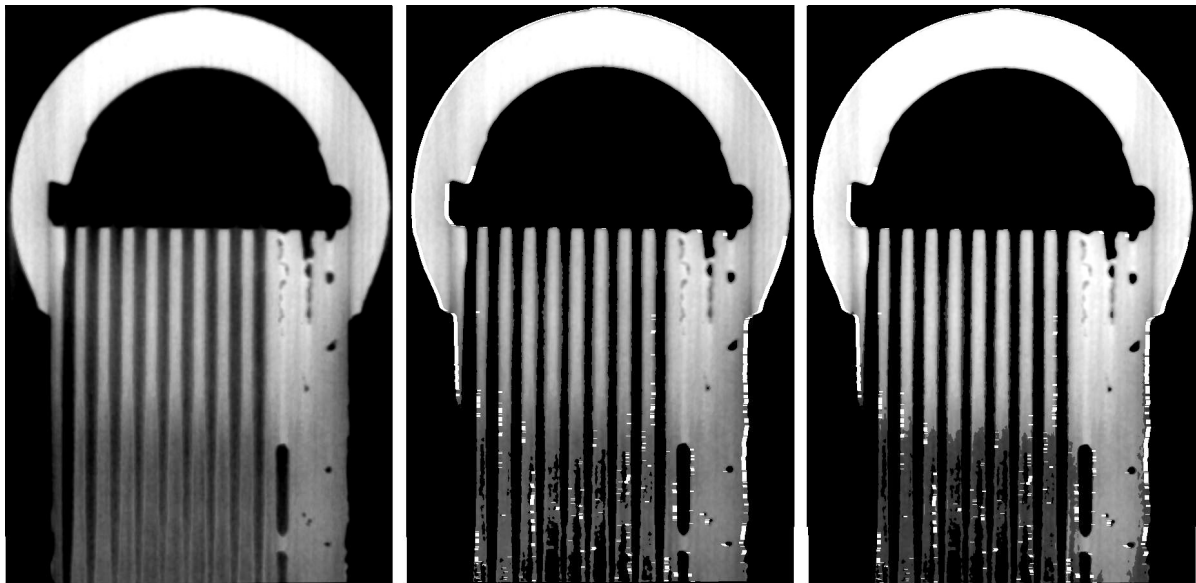(d)

(e)

(f)

(g)

1 0 0 0 0 0 0 0 0 0 0 1

(h)

Attachment 3 Step-by-step editing of a lower contrast image: (a) Raw image (b) Highted edges by `highlightEdges` function (c) Image after contrast adjustment (d) Sharpened image (e) Binarized image (f) Image reducet from the upper and bottom side (g) Image reduced to only tube part (h) Result vector

(a)

(b)

(c)

(d)

(e)

(f)

(g)

1 1 1 0 1 0 0 1 1 1 1 1

(h)

Attachment 4 Step-by-step editing of an image with confluent channel mouth and lower contrast:
(a) Raw image (b) Highted edges by `highlightEdges` function (c) Image after contrast adjustment
(d) Sharpened image (e) Binarized image (f) Image reducet from the upper and bottom side (g) Image
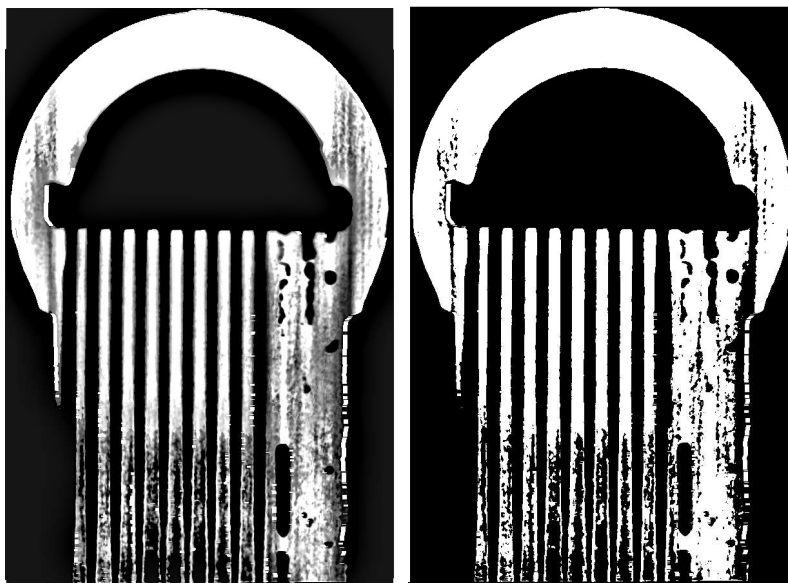reduced to only tube part (h) Result vector

Attachment 5 Step-by-step editing of a rotated image with a thin wall: (a) Raw image (b) Highted edges by `highlightEdges` function (c) Image after contrast adjustment (d) Sharpened image (e) Binarized image (f) Image reducet from the upper and bottom side (g) Image reduced to only tube part (h) Result vector

Attachment 6 Step-by-step editing of an image with a thin wall: (a) Raw image (b) Highted edges by `highlightEdges` function (c) Image after contrast adjustment (d) Sharpened image (e) Binarized image (f) Image reducet from the upper and bottom side (g) Image reduced to only tube part (h) Result vector
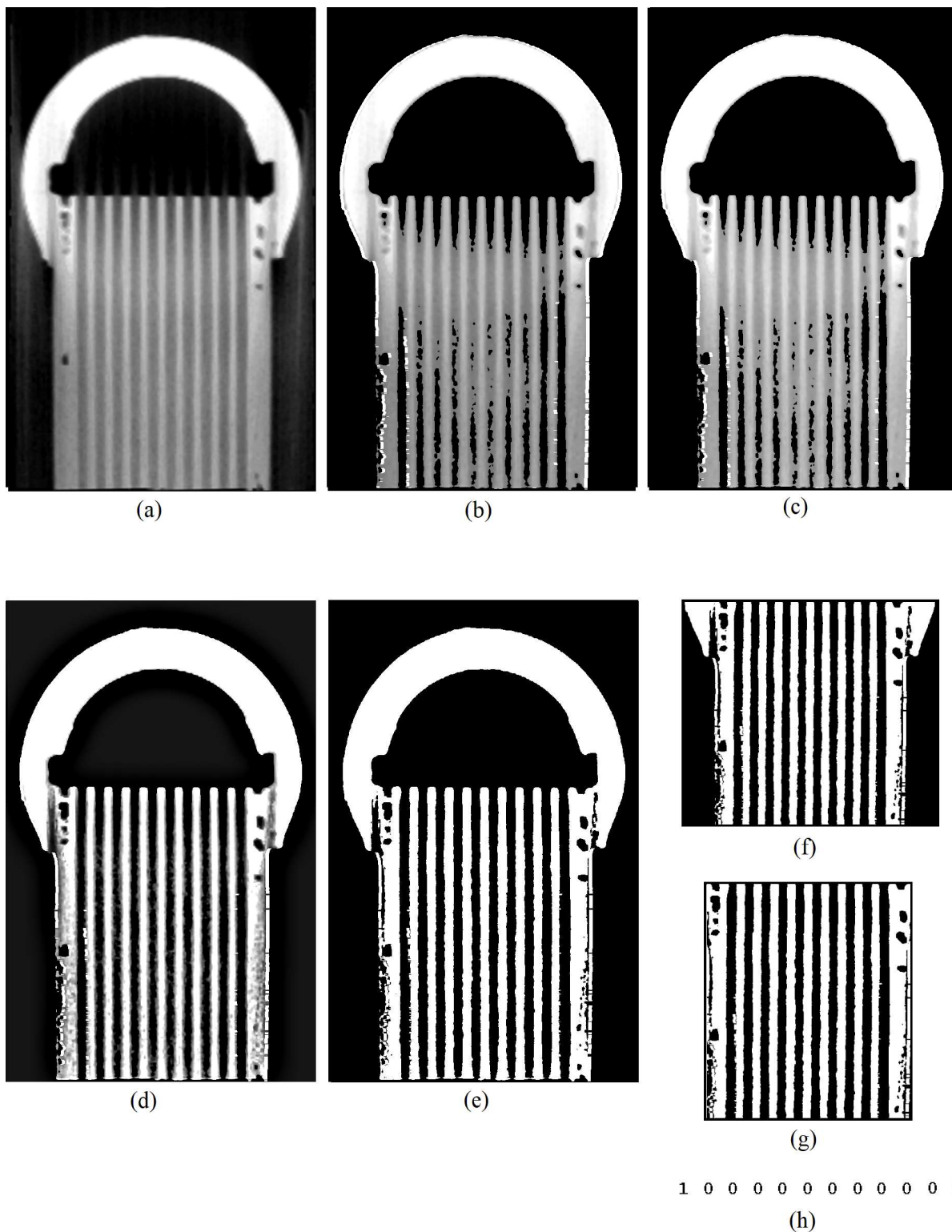
(a)

(b)

(c)

(d)

(e)

(f)

(g)

1 0 0 0 0 0 0 0 0 0 0 1

(h)

Attachment 7 Step-by-step editing of a good image with a slightly lower contrast: (a) Raw image (b) Highted edges by `highlightEdges` function (c) Image after contrast adjustment (d) Sharpened image (e) Binarized image (f) Image reducet from the upper and bottom side (g) Image reduced to only tube part (h) Result vector